Experimental and Theoretical Investigation of Structural, Magnetic and Optical Properties of Nd_2FeCrO_6 and Gd_2FeCrO_6 Perovskites Synthesized by Sol-gel Technique

By

Md. Didarul Islam Bhuyan

DOCTOR OF PHILOSOPHY

Department of Physics
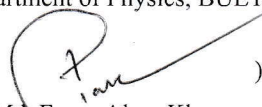
BANGLADESH UNIVERSITY OF ENGINEERING AND TECHNOLOGY

April 2022

The thesis titled "EXPERIMENTAL AND THEORETICAL INVESTIGATION OF STRUCTURAL, MAGNETIC AND OPTICAL PROPERTIES OF Nd_2FeCrO_6 and Gd_2FeCrO_6 PEROVSKITES SYNTHESIZED BY SOL-GEL TECHNIQUE" submitted by Md. Didarul Islam Bhuyan, Roll No.: 0417144001F, Session: April-2017 has been accepted as satisfactory in partial fulfillment of the requirement for the degree of Doctor of Philosophy on 2 April 2022.

BOARD OF EXAMINERS

( )

1   Dr. Mohammed Abdul Basith   Chairman
     Professor   (Supervisor)
     Department of Physics, BUET, Dhaka-1000

( )

2   Dr. Nasreen Akter   Member
     Professor & Head   (Ex-Officio)
     Department of Physics, BUET, Dhaka-1000

( )

3   Dr. Md. Feroz Alam Khan   Member
     Professor
     Department of Physics, BUET, Dhaka-1000

( )

4   Dr. Muhammad Rakibul Islam   Member
     Associate Professor
     Department of Physics, BUET, Dhaka-1000

( )

5   Dr. Md. Zunaid Baten   Member
     Associate Professor
     Department of EEE, BUET, Dhaka-1000

( )

6   Dr. Md. Abu Hashan Bhuiyan   Member
     Former Professor
     Department of Physics, BUET, Dhaka-1000

( )

7   Dr. A. B. M. Obaidul Islam   Member
     Professor
     Department of Physics, University of Dhaka, Dhaka

( )

     Dr. Abdul Hannan   Member
8   Professor   (External)
     Department of Physics
     Shahjalal University of Science and Technology, Sylhet

CANDIDATE'S DECLARATION

It is hereby declared that this thesis or any part of it has not been submitted elsewhere for the award of any degree or diploma.

Md. Didarul Islam Bhuyan

Acknowledgements

Finally, I want to extend my gratefulness to my family members, particularly my wife, parents, and kid, for their love, support, and blessings.

Abstract

In this investigation the physical properties of Nd_2FeCrO_6 and Gd_2FeCrO_6 double perovskites were studied both theoretically and experimentally. The first-principles predictions on the structural stability, magnetic behaviour and electronic structure of B-site ordered double perovskite Nd_2FeCrO_6 have been reported. The thermodynamic, mechanical, and dynamic stability analyses suggest the possibility of the synthesis of Nd_2FeCrO_6 double perovskite at ambient pressure. This compound shows ferrimagnetic (FiM) nature with 2 μ_B net magnetic moment and the magnetic ordering temperature has been estimated to be ~265 K. Electronic structure indicates a higher probability of direct photon transition over the indirect transition with a band gap of ~1.85 eV. Based on the theoretical prediction, Nd_2FeCrO_6 and Gd_2FeCrO_6 nanoparticles were synthesized for the first time using a facile citrate-based sol-gel method, and their structural, magnetic, and optical characteristics were thoroughly studied. Rietveld refinement analysis of the powder X-ray diffraction pattern of the synthesized Nd_2FeCrO_6 and Gd_2FeCrO_6 nanoparticles confirmed their single-phase orthorhombic and monoclinic structure with *Pnma* and *P2₁/n* space group, respectively. X-ray photoelectron spectroscopy confirmed the presence of mixed-valence states of Fe and Cr. The temperature dependent magnetization curves exhibited magnetic reversal behavior in Nd_2FeCrO_6 double perovskite at temperature 6 K in the field cooled (FC) mode. Interestingly, exchange bias effect was observed in this double perovskite material while the sample was cooled down from 300 K to 10 K and magnetic fields were applied during cooling. The zero-field cooled (ZFC) and field cooled curves of Gd_2FeCrO_6 perovskite largely diverged below 20 K. A downturn was observed in the ZFC curve at 15 K which corresponds to an antiferromagnetic, Néel transition. The narrow magnetic hysteresis loop of Gd_2FeCrO_6 recorded at 5 K was nearly saturated and demonstrated an asymmetric shift along the magnetic field axis indicating the concurrence of ferromagnetic and antiferromagnetic domains in Gd_2FeCrO_6 nanoparticles. The optical band gap of Nd_2FeCrO_6 and Gd_2FeCrO_6 nanoparticles are found to be 1.95 eV and 2.00 eV, respectively, evaluated experimentally from the UV–visible and photoluminescence spectroscopic analyses. Here, by employing experimentally obtained structural parameters of Gd_2FeCrO_6 perovskite in first-principles calculation, the spin-polarized electronic band structure, density of states and optical absorption property of Gd_2FeCrO_6 double perovskite were also investigated and compared the results with experimental outcomes. Therefore, due to the lower band gap and magnetically tunable exchange bias, it is anticipated that the

newly synthesized Nd_2FeCrO_6 and Gd_2FeCrO_6 double perovskites could be the promising materials for visible-light-driven energy device and spintronic applications.

Contents

List of figures

List of tables

List of abbreviations

AFM	Antiferromagnetic
BFGS	Brodyden-Fletcher-Goldfarb-Shanno
BVS	Bond Valence Sum
BZ	Brillouin Zone
CA	Citric Acid
CASTEP	Cambridge Serial Total Energy Package
CBM	Conduction Band Minimum
DFT	Density Functional Theory
DI	Deionized
DM	Dzyaloshinskii-Moriya
DOS	Density of States
DP	Double Perovskite
DPOs	Double Perovskite Oxides
EDX	Energy Dispersive X-ray Spectroscopy
EG	Ethylene Glycol
FC	Field Cooled
FESEM	Field Emission Scanning Electron Microscopy
FM	Ferromagnetic
FiM	Ferrimagnetic
FTIR	Fourier Transform Infrared Spectroscopy
GFCO	Gd_2FeCrO_6
GGA	Generalized Gradient Approximation
GII	Global Instability Index
HRTEM	High Resolution Transmission Electron Microscopy
LDA	Local Density Approximation
NFCO	Nd_2FeCrO_6
NHE	Normal Hydrogen Electrode
PBE	Perdew–Burke–Ernzerhof

PDOS	Partial Density of States
PL	Photoluminescence
PWPP	Planewave Pseudopotential
PVA	Polyvinyl Alcohol
Re	Rare earth
RT	Room Temperature
TEM	Transmission Electron Microscopy
TDOS	Total Density of States
TGA	Thermogravimetric Analysis
USP	Ultrasoft Pseudopotentials
UV	Ultraviolet
VASP	Vienna Ab-initio Simulation Software
VBM	Valence Band Minimum
VESTA	Visualization for Electronic and Structural Analysis
SCF	Self-consistent Field
SPuDS	Structure Prediction Diagnostic Software
SQUID	Superconducting Quantum Interference Device
XRD	X-ray diffraction
XPS	X-ray Photoelectron Spectroscopy
ZFC	Zero Field Cooled

CHAPTER 1

INTRODUCTION

1.1 Background

The promises of B-site ordered double perovskite oxides (DPOs) $A_2B'B''O_6$ (A: alkaline or rare-earth ions, e.g., Sr, Pr, La, Gd, etc.; B′, B″: transition metals like Fe, Cr, Ni, Mn, etc.) over $AB'O_3$ and $AB''O_3$ single perovskites for magnetic and semiconductor-based applications have long been recognized [1-4]. Recently, many studies have investigated the structural and transport properties of rare-earth-based DPOs, which exhibit a broad variety of functional qualities depending on their different cationic orderings and oxidation states [5-8]. Double perovskites provide a wide range of structural flexibility as well as freedom of choosing a suitable combination of B′ and B″ cations from the periodic table and provides opportunity to control their electronic structure, magnetic behavior, etc. for practical application [9]. In particular, $A_2B'B''O_6$ double perovskite enables us to tune a vast variety of electronic and magnetic properties of its parent $AB'O_3$ and $AB''O_3$ single perovskites by introducing additional B′-O-B″ magnetic exchange interaction [5]. Compared to the B′-O-B′ or B″-O-B″ interaction, the physical significance of B′-O-B″ interaction is more interesting [10]. Since it can accommodate two different B′ and B″ cations, their difference in ionic radius often leads to structural phase transition as well as modification in the octahedral (BO_6) environment. The flexibility of the formation of $A_2B'B''O_6$ double perovskite by adapting a suitable combination of B′ and B″ cations provide an opportunity to control their electronic structure, magnetic behavior, etc. and opens the path to search for new multi-functional materials. To realize the opportunities of $A_2B'B''O_6$, the major challenge is to achieve the long-range B′ and B″ sites (B site) ordering, which is governed by kinetic and thermodynamic factors of order-disorder reactions during synthesis of these materials [11, 12].

Fig. 1.1 shows a schematic illustration of possible B′ and B″ sites distribution when B″ is inserted into $AB'O_3$ in order to form $A_2B'B''O_6$ double perovskite. If the synthesis conditions are not optimized for a certain material, it may form a randomly distributed B′ and B″ phase or a partially ordered phase. The physical properties especially magnetism is strongly dependent on the degree of cations ordering in double perovskite [13]. For example, $ReB'_{0.5}B''_{0.5}O_3$ perovskites, containing rare-earth (Re) elements, have orthorhombic (*Pnma*) crystal structure as like as $ReB'O_3$, but demonstrate enhanced

magnetization because of the additional B′-O-B″ net ferromagnetic (FM) exchange interaction along with B′-O-B′, B″-O-B″, Re-O-B′/B″, and Re-O-Re antiferromagnetic (AFM) interactions [5]. These materials are generally weak FM due to the competing AFM and FM superexchange interactions arising from the B-site disordering as shown in Fig. 1.1(b) [2, 13-17]. Yuan *et al.*[18] studied several orthorhombic ReFe$_{0.5}$Cr$_{0.5}$O$_3$ systems and reported that magnetization improves greatly upon degree of B-site ordering of Fe and Cr atoms via the Fe^{3+}(d^5)–O–Cr^{3+}(d^3) interaction. Interestingly, due to the presence of multiple magnetic interactions, multiple magnetic phase transitions with variation in temperature have been observed corresponding to the activation of each interaction. Yin *et al.* [19] reported that DyFe$_{0.5}$Cr$_{0.5}$O$_3$ perovskite shows an anomaly in temperature dependent magnetization curve near 261 K due to the Fe^{3+}(d^5)–O–Cr^{3+}(d^3) interaction and another at 120 K, related to the Cr^{3+}(d^3)–O–Cr^{3+}(d^3) interaction which is expected for DyCrO$_3$. Indeed, DyFe$_{0.5}$Cr$_{0.5}$O$_3$ also show another anomaly at 640 K corresponding to the onset of Fe^{3+}(d^5)–O–Fe^{3+}(d^5) interaction, which also observed for DyFeO$_3$ [15]. Similar multiple magnetic phase transitions have been reported for NdFe$_{0.5}$Cr$_{0.5}$O$_3$ disordered perovskite [20, 21]. From these reports, it is evident that ReB′$_{0.5}$B″$_{0.5}$O$_3$ retains the properties of their parent compounds and the strength of B′-O-B″ interaction is much weaker than that of B′-O-B′ and B″-O-B″ AFM interaction [22-24]. For the technological applications, long range B′-O-B″ interaction is more demanded [10]. Therefore, to achieve a very high degree of ordering in B-sites, a number of synthesis techniques like solid-state reaction, soft chemical-based synthesis routes, and thin-film deposition techniques have been proposed [11-13, 25-27]. In B-site ordered double perovskites, one may find three patterns (rock salt, columnar and layered) for B′ and B″ depending on the choice of cations and synthesis condition [28, 29]. The rock salt ordering is most symmetric and common as the array of B′ and B″ cations is equivalent to the anion and cation positions as shown in Fig. 1.1(d) [29, 30].

Among the double perovskites, rear-earth (Re) containing magnetic semiconductors, Re$_2$B′B″O$_6$ (4f-3d-3d system) have gained significant research interest because of their wide range of technological applications and rich physical properties [31, 32]. For instance, Re$_2$NiMnO$_6$ systems have been studied extensively due to their ferromagnetism, low band gap, large magneto-capacitance, magneto-resistance, and relaxor ferroelectricity [33, 34]. Notably, Re$_2$FeCrO$_6$ is another class of double perovskites which is expected to be a hub of ferrimagnetic semiconductors [35], however, they are less
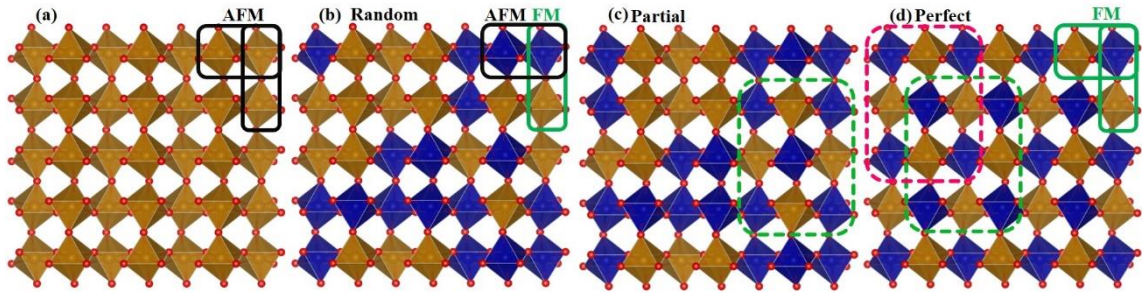
Fig. 1.1 (a) Cation order in $AB'O_3$ perovskite. (b) Random distribution of B' and B'' cations in disordered $AB'_{0.5}B''_{0.5}O_3$ perovskite. (c) Partial ordering of B' and B'' cations in disordered $AB'_{0.5}B''_{0.5}O_3$ perovskite. (d) Perfectly B' and B'' sites ordered double perovskite $A_2B'B''O_6$.

studied either by experimental or computational investigation. Double perovskite La_2FeCrO_6 is an example of this class that has been synthesized using the pulsed laser deposition technique with a high degree of Fe and Cr ordering [36, 37] and the electronic properties of this compound have been studied by the first-principles calculations [38]. Unlike the randomly distributed Cr and Fe disordered AFM perovskite $LaCr_{0.5}Fe_{0.5}O_3$, ordered La_2CrFeO_6 double perovskite shows FiM nature with a saturation magnetization of $\sim 2\mu_B$ per formula unit (f.u.) [36, 37]. Recently Majumder *et al.*[2] reported a saturation magnetization of $\sim 0.8 \mu_B$/f.u. in partially ordered Pr_2FeCrO_6 bulk sample. Undoubtedly, a complete B-site ordered phase is difficult to achieve for double perovskite samples by conventional solid-state or sol-gel technique. Booth *et al.* [39] achieved perfect ordering in several Re_2NiMnO_6 double perovskites by repeated sintering where the number of required sintering steps and sintering temperature varied with different Re cations.

Most recently, Das *et al.* identified almost canted or compensated ferrimagnetic ordering of the Fe moments in Pr_2FeCrO_6 double perovskite [40]. In ordered perovskites, the $Fe^{3+}_\uparrow$-O-$Cr^{3+}_\downarrow$ super-exchange interaction is dominant, whereas the disordered perovskites show the dominant AFM $Fe^{3+}_\uparrow$-O-$Fe^{3+}_\downarrow$ and $Cr^{3+}_\uparrow$-O-$Cr^{3+}_\downarrow$ interactions (illustrated in Fig. 1.1). The partially ordered perovskites demonstrate a small magnetization due to the presence of additional FiM $Fe^{3+}_\uparrow$-O-$Cr^{3+}_\downarrow$ superexchange interaction in conjugation to the strong AFM interactions [22-24].

There is significant interest in finding new eco-friendly, conveniently synthesizable, low-cost, and lead-free light absorber materials for solar cell applications [41, 42]. Furthermore, Bi_2FeCrO_6 and Pr_2FeCrO_6 double perovskites have recently demonstrated fascinating optoelectronic characteristics such as a suitable band gap, strong absorbance in the visible range, and high photocatalytic performances. Due to their diverse magnetic

and optical properties, researchers are curious about other members of the Re_2FeCrO_6 double perovskite family. Experimentally, the difficulties could have come from the almost equivalent ionic radii of Fe and Cr, which poses a hurdle to produce B-site ordered samples [36]. The experimental investigation of the material properties of these double perovskites at the molecular level are sometimes unattainable due to the unavailability of the required experimental facilities. These complexities can be circumvented to a greater extent by implementing the Density Functional Theory (DFT) based on first-principles calculation [43, 44]. In this investigation, the parent single perovskites $NdFeO_3$ and $NdCrO_3$ were studied initially to understand the effect of Hubbard parameter U (U_{eff} = U-J, where the effects of the on-site Coulomb and exchange interactions are denoted by U and J, respectively, hereafter referred to simply as U) on magnetic and electronic properties.

First-principles calculation showed Nd_2FeCrO_6 satisfied the thermodynamic, mechanical, and dynamic criteria as a stable compound. Based on theoretical outcomes of Nd_2FeCrO_6, a stable structure of double perovskite Nd_2FeCrO_6 and Gd_2FeCrO_6 nanoparticles were synthesized by adapting a low-cost facile sol-gel method and investigated extensively their crystallographic structure along with field and temperature-dependent magnetic properties.

In rare-earth-based single perovskites $ReFeO_3$ (Re = rare-earth element), the 4f electron -based Re sublattice and 3d electron-based Fe sublattice are coupled in an antiparallel fashion. In these orthoferrites, the noncollinear antiferromagnetism in the Fe sublattice demonstrates weak ferromagnetism [45, 46] comparatively at high temperatures, while the Re sublattice usually orders antiferromagnetically at much lower temperatures. The exchange interaction between 3d electrons is substantially stronger than that of 4f electrons, therefore, the two sublattices reveal temperature dependent complex magnetic behavior [47]. Like orthoferrites, rare-earth orthochromites $ReCrO_3$ also exhibit complex magnetic transitions at different temperatures due to a rich variety of magnetic spin interactions between Re^{3+} and Cr^{3+} [48, 49]. When cooled from room temperature, the Cr sublattice in $ReCrO_3$ is found to order at a critical temperature T_{N1}, whereas the rare earth sublattice orders at a much lower temperature (T_{N2}) [49]. Interestingly, magnetization reversal was also observed in both $ReFeO_3$ [50] and $ReCrO_3$ [51, 52] single perovskites. In addition to magnetization reversal, recent investigations have also demonstrated the presence of exchange bias effect in a number of single perovskites ferrite-chromite e.g.,

$YFe_{0.5}Cr_{0.5}O_3$ [53], $LuFe_{0.5}Cr_{0.5}O_3$ [54], $NdFe_{0.5}Cr_{0.5}O_3$ [20, 21]. The presence of intriguing magnetic properties in the aforementioned ferrite-chromite was another motivation to synthesize Nd_2FeCrO_6 and Gd_2FeCrO_6 double perovskites. To the best of our knowledge, the crystallographic structure and physical properties of Nd_2FeCrO_6 and Gd_2FeCrO_6 double perovskites have not been reported yet.

1.2 Objectives of the present study

The objectives of the present research are as follows:

(i) Theoretical investigation of structural, magnetic, electronic and optical properties of Nd_2FeCrO_6 and Gd_2FeCrO_6 double perovskite by first-principles DFT calculations.

(ii) Synthesis of Nd_2FeCrO_6 and Gd_2FeCrO_6 perovskites via a facile sol-gel technique.

(iii) Characterization of the as-prepared samples by analyzing their Rietveld refined powder X-ray diffraction patterns. Analysis of their chemical structure by Fourier transform infrared spectrum.

(iv) Investigation of the bond length of as-synthesized Nd_2FeCrO_6 and Gd_2FeCrO_6 double perovskites using Raman spectra.

(v) Analysis of their surface morphology by performing field emission scanning electron microscopy imaging. Investigation of the size and crystalline structure of the nanoparticles using transmission electron microscopy imaging.

(vi) Investigation of the chemical binding energies and valence states of different elements by X-ray photoelectron spectroscopy.

(vii) Investigation of the temperature and field-dependent magnetic properties of the as-prepared samples using a superconducting quantum interference device magnetometer.

(viii) Investigation of optical properties of the synthesized materials using UV–visible and photoluminescence spectrometers.

1.3 Outline of the thesis

This thesis contains the following chapters:

➤ **Chapter 1** of this thesis deal with the introduction and importance of double perovskites and the objectives of the investigation.

➢ **Chapter 2** provided a literature review in the relevant areas of the double perovskites.

➢ **Chapter 3** included a detailed description of the sample preparation and the different measurement techniques that have been used in this research work.

➢ **Chapters 4**, **5** and **6** presented the results of various investigations of the study and explanation of results in the light of existing theories.

➢ **Chapter 7** included the summary and conclusions of this research**.**

CHAPTER 2

LITERATURE REVIEW

2.1 Previous investigations on double perovskite materials

In the last few decades, perovskite oxides, ABO_3 (A = rare earth or alkaline metal ions, B = transition metal ions), have intrigued significant research interest due to their exceptional structural and compositional flexibility. Recently, substituting exactly half of the transition metal ions of perovskites by another cation has resulted in a number of interesting double perovskites (Fig. 2.1), $A_2B'B''O_6$ (e.g., A = La, Sr, Bi, Y, Pr, Nd, Gd, etc., B' and B'' = Co, Fe, Cr, Ni, Mn, etc.) which possess a great diversity of functional properties based on their various cationic orderings and oxidation states.
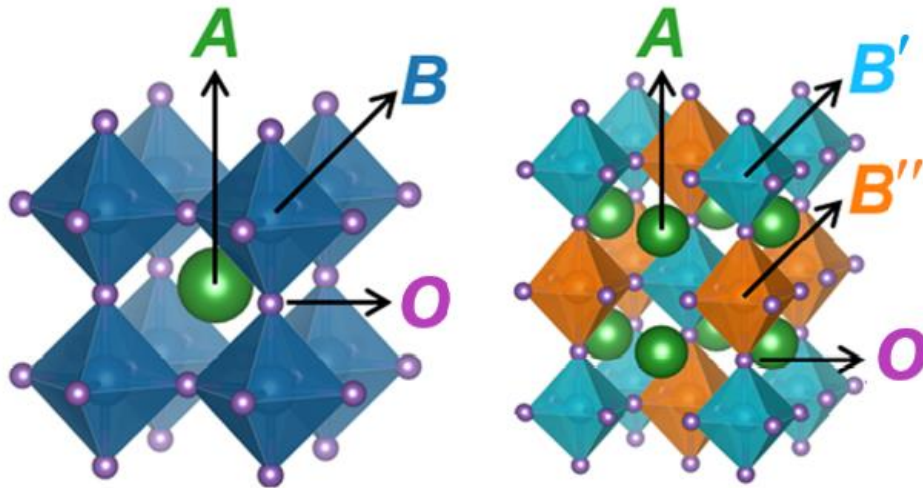
Fig. 2.1 Crystal structure of (a) single perovskite, where the A cation is surrounded by a network of corner sharing BO_6 octahedra and (b) double perovskite, where the A cations are surrounded by an alternating network of $B'O_6$ and $B''O_6$ octahedra [55].

Recently, S. Vasala and M. Karppinen have published a review work [1] that explored a thousand $A_2B'B''O_6$ type double perovskites, most of which were synthesized at ambient pressure. Additionally, a range of novel $A_2B'B''O_6$ compounds were also fabricated under high-pressure. However, a number of their synthesized compounds having $A_2B'B''O_6$ stoichiometry failed to achieve the desired perovskite crystal structure. In Fig. 2.2, the scenario for compounds with the most common A-site cations (A = Ca, Sr, Ba, and La) has been graphically depicted. Notably, these compositions account for the vast majority of known compounds, totalling over 800 [1]. However, as can be observed, many potential cation combinations are yet unexplored.
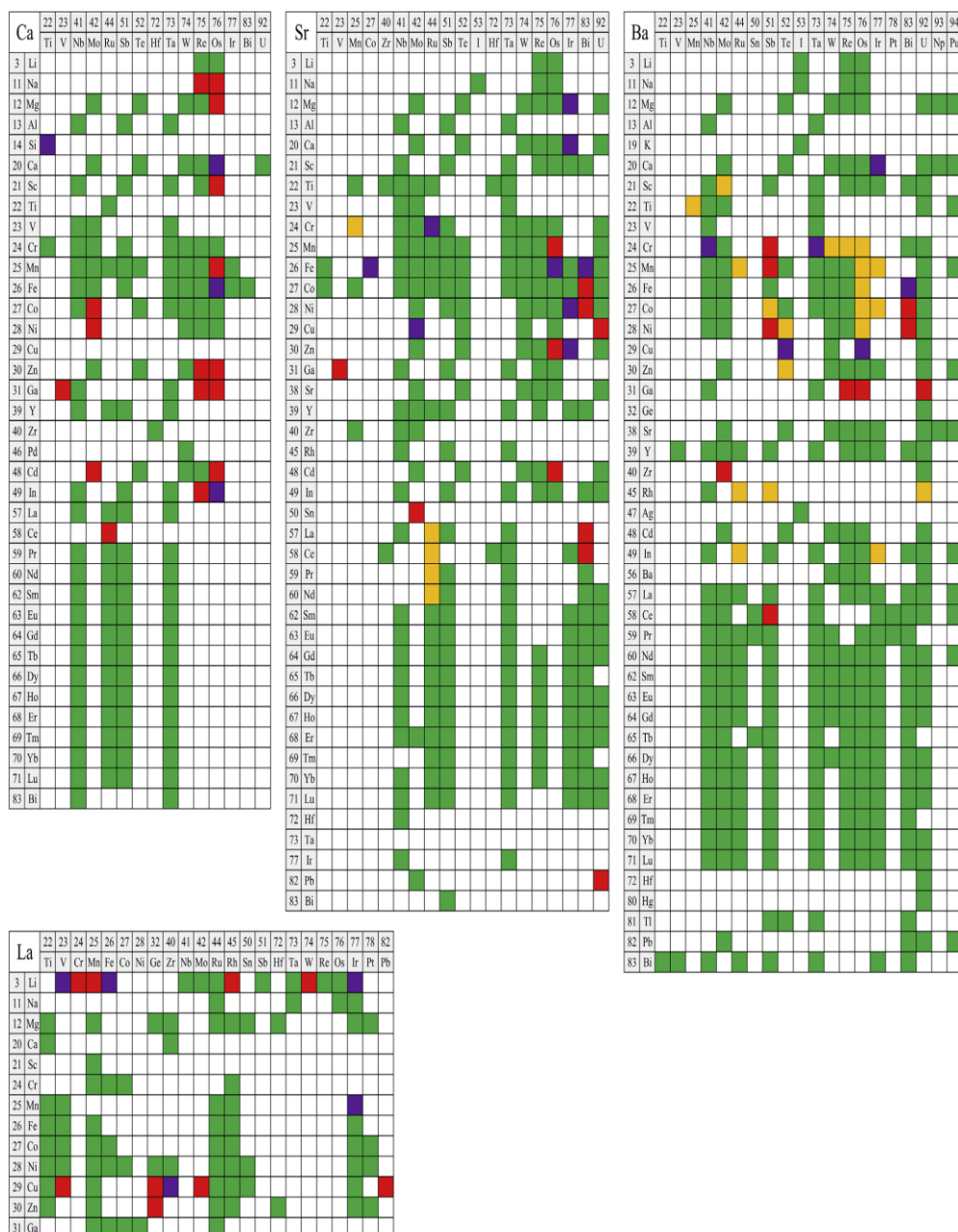
Fig. 2.2 $A_2B'B''O_6$ compositions with A = Ca, Sr, Ba, or La reported in the literature. Left column represents the B′ cation and top row the B″ cation. The colors indicate perovskite compounds synthesized at ambient pressure (green) or stabilized using either high-pressure or high oxygen-partial-pressure synthesis (purple), and compounds with a hexagonal non-perovskite structure with the $A_2B'B''O_6$ stoichiometry (yellow), and cases where a phase of the $A_2B'B''O_6$ composition does not form (red) [1].

Until now Re_2NiMnO_6 double perovskites (where Re = rare earth metal ions) have been widely explored owing to their ferromagnetism, narrow band gap, strong magneto-capacitance, magneto-resistance, and relaxor ferroelectricity. However, Re_2FeCrO_6 is a kind of double perovskite that is expected to be a hub for ferrimagnetic semiconductors but has received less experimental and computational attention. The family of

Re_2NiMnO_6 double perovskites has been explored by number reaserch of groups. Among them, recently, M. Nasir *et al.* [33] investigated the R_2NiMnO_6 (R= rare earth metal ions) double perovskite series. This group synthesized all double perovskites using sol-gel method. It was observed that the ionic radius of R-site cations affects the structural characteristics of R_2NiMnO_6. X-ray patterns established that all samples were single-phase except Tb_2NiMnO_6, Ho_2NiMnO_6 and Y_2NiMnO_6 (Fig. 2.3). A minor impurity peak appeared for Tb_2NiMnO_6, Ho_2NiMnO_6 corresponding to Tb_2O_3 and Ho_2O_3, respectively. Investigations showed, the fluctuation of lattice characteristics and cell volume with an ionic radius of R cations and the tolerance factor of these materials varied from 0.925 to
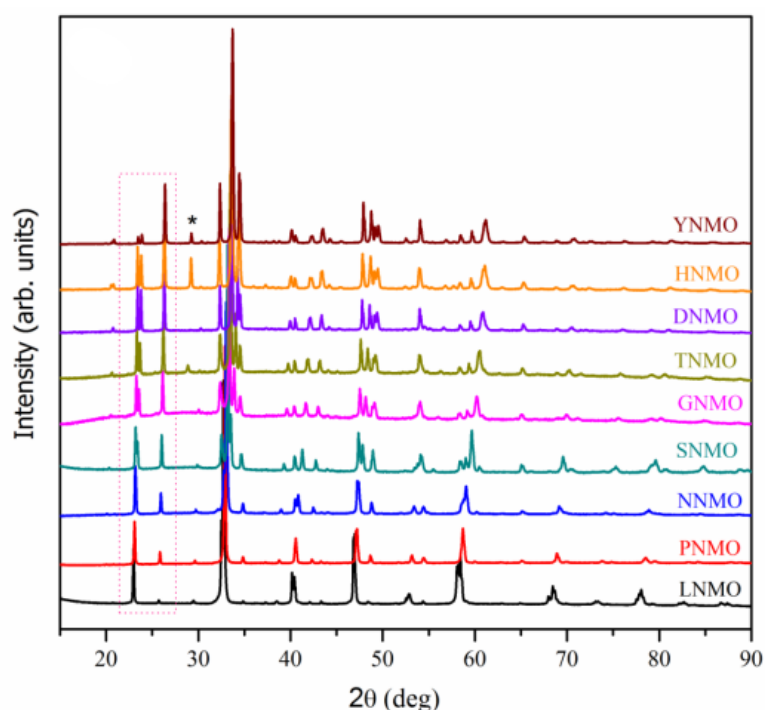
Fig. 2.3 (a) Normalized X-ray diffraction patterns of R_2NiMnO_6 (R= La, Pr, Nd, Sm, Gd, Tb, Dy, Y, and Ho). All the peaks were indexed to the monoclinic cell belonging to *$P2_1/n$* space group [33].

0.849 with decreases of ionic radii, $\langle r_R \rangle$ from La to Ho. Notably, the ionic radii reduced in the order of $r_{La} > r_{Pr} > r_{Nd} > r_{Sm} > r_{Gd} > r_{Tb} > r_{Dy} > r_Y > r_{Ho}>$. Except for La_2NiMnO_6, the lattice parameter "*b*" rose as the tolerance factor decreased. This was associated to the displacement of oxygen ions, which resulted in the octahedra tilting as $\langle r_{Re} \rangle$ decreases. This investigation also showed that the tilting angle progressively increased with the reduction in the size of the rare earth ion, from 7.1° for La_2NiMnO_6 to 17.9° for Ho_2NiMnO_6. The magnetic properties of Re_2NiMnO_6 samples were also

investigated in the temperature range of 4-300 K under 100 Oe. The zero-field cooled (ZFC) and Field Cooled Cooling (FCC) M-T data for all the Re_2NiMnO_6 samples were
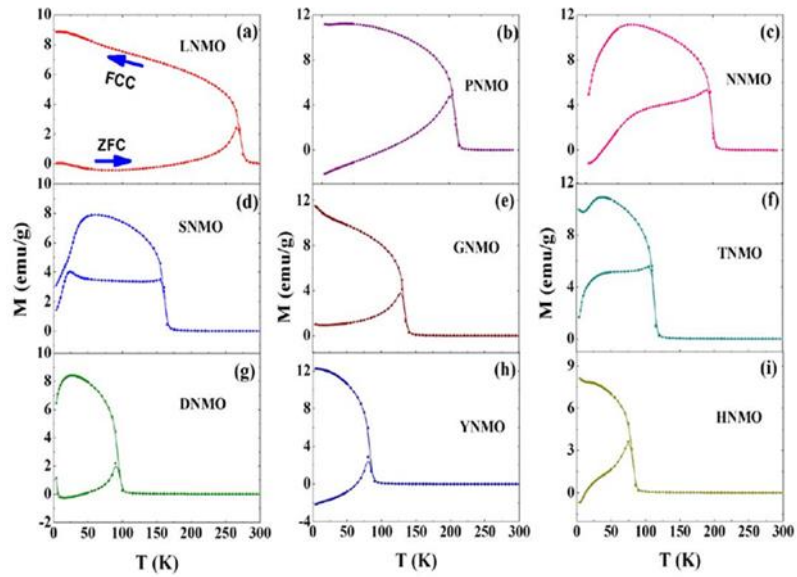
Fig. 2.4 Temperature dependence of the field-cooled cooling (FCC) and zero-field cooling (ZFC) dc magnetization for R_2NiMnO_6 double perovskites under 100 Oe applied magnetic field: (a) LNMO, (b) PNMO, (c) NNMO, (d) SNMO, (e) GNMO, (f) TNMO, (g) DNMO, (h) YNMO, and (i) HNMO [33].

shown in Fig. 2.4. Thermomagnetic irreversibility was reported for all samples in the ZFC and field FCC M-T values below the ferromagnetic transition temperature, T_C. This behaviour was typical for R_2NiMnO_6 compounds. At lower temperatures, the bifurcation of the FCC and ZFC curves suggested competing magnetic interactions or spin geometric frustrations such as spin glass or cluster glass. Authors also reported that T_c decreased with decreases r_R^{3+}, which was a good agreement with the M-T analysis done by R. J. Booth *et al.* [39]. This monotonic decrease of T_c with decreasing r_R^{3+} indicated the correlation of magnetism with Ni/Mn-O bond length and the Ni-O-Mn bond angle. Isothermal field-dependent magnetization hysteresis loops (Fig. 2.5) for R_2NiMnO_6 at 5 K temperature demonstrated that all samples were ferromagnetic. This investigation discovered that the magnetic nature of R^{3+} ions affect the behaviour of M-H curves. The magnetization rose continuously for Gd_2NiMnO_6, Tb_2NiMnO_6, Dy_2NiMnO_6, and Ho_2NiMnO_6 samples up to the field of 5 T. This might be arising from the polarization of the $Gd^{3+}/Tb^{3+}/Dy^{3+}/Ho^{3+}$ moments. The optical band gaps of these double perovskites were also measured by plotting Tauc plot and reported that the band gap of R_2NiMnO_6 increased with the decreasing ionic radius of Re cations from 1.42 to 1.68 eV.
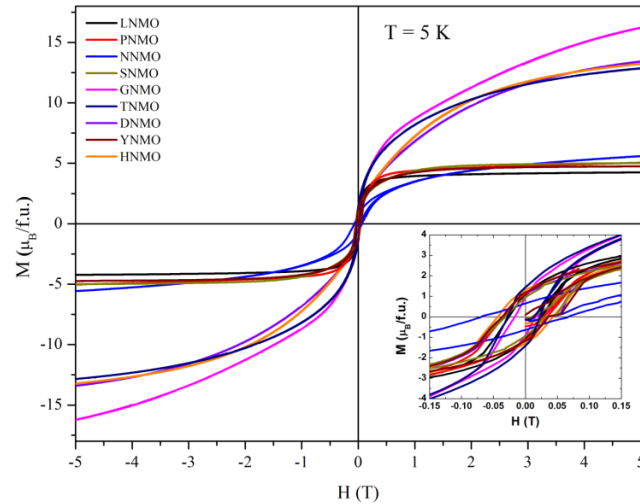
Fig. 2.5 Magnetization vs magnetic field isotherms for R_2NiMnO_6 at 5 K temperature [33].

Earlier, in another investigation, Booth *et al.* [39] explored the structural, magnetic and dielectric properties of a series of double perovskite oxides, Re_2NiMnO_6 (Re = Pr, Nd, Sm, Gd, Tb, Dy, Ho and Y). Using repeated sintering temperatures, the authors claimed to have achieved perfect ordering in several Re_2NiMnO_6 double perovskites. All of the phases had monoclinic ($P2_1/n$) double perovskite structures, with Ni and Mn atoms arranged at 2c and 2d sites, respectively and they showed ferromagnetic behaviour. It was observed that the radius of Re^{3+} atoms is more closely related to the Re_2NiMnO_6 series' ferromagnetic ordering temperature than to the average Ni–O–Mn angle in the double perovskite structure. All samples had Mn^{4+} and Ni^{2+} with the presence of antisite disorder.

Temperature-dependent magnetic properties of Nd_2NiMnO_6 double perovskite were investigated by R. Yadav *et al.* [56]. The outcome of the investigation showed that Nd_2NiMnO_6 is a ferromagnetic material with a transition temperature of 190 K and an additional anomaly at a lower temperature. Due to superexchange interaction between Ni^{2+}-O-Mn^{4+}, FM order was developed. The antiferromagnetic interaction in the sample was ascribed to the sample's mixed-valence states of Ni^{3+} and Mn^{3+}, which resulted in a lower temperature magnetic transition. An additional transition was observed near 100 K in the field cool curve of Nd_2NiMnO_6. However, Choudhury *et al.* [57] reported that the two magnetic features were an intrinsic part of a homogeneous system due to antisite disorder. C. Shi *et al.* [58] also observed double magnetization transition temperatures at 193.04 K and 105.12 K from the temperature-dependent magnetization curve of Nd_2NiMnO_6 due to Ni^{2+}–O–Mn^{3+} and Ni^{3+}–O–Mn^{4+} superexchange interactions,

respectively. However, in Dy_2NiMnO_6, two magnetic transitions occurred around 100 K and 20 K [59]. As reported by Kumar P. *et al.* [60], DC and AC magnetic susceptibility measurements of La_2NiMnO_6 showed two magnetic anomalies at T_{C1} ~270 K and T_{C2} ~240 K, indicating the ferromagnetic ordering of the monoclinic and rhombohedral phases, respectively. The authors observed a broad peak at a lower temperature (70 K), indicating a spin-glass transition due to Ni^{2+} and Mn^{4+} ions' partial anti-site disorder.

On the other hand, the synthesis of Re_2FeCrO_6 (Re= rare earth meatal ions) double perovskites was challenging due to the similar ionic radii of Fe and Cr ions. It should be noted that except La_2FeCrO_6, Pr_2FeCrO_6 and Y_2FeCrO_6 double perovskites, other members of Re_2FeCrO_6 family are less explored either by experimental or computational investigation. Several groups investigated Re_2FeCrO_6 (R_e= La, Pr and Y) double perovskite materials. Among them, most recently, Majumder *et al.* [2] reported the crystal structure and the nature of the magnetic ground state of the polycrystalline compound Pr_2FeCrO_6. Analysis associated with XRD pattern unveiled that the Pr_2FeCrO_6 double perovskite exhibited a B-site disordered orthorhombic crystal structure. The crystallographic unit cell's B-sites have a random distribution of Fe^{3+} and Cr^{3+} magnetic sublattices, which helps to produce a variety of intriguing magnetic characteristics. Three unique anomalies were discovered in the temperature dependence of the magnetization and magnetic entropy change curves of the compound: (i) a G-type canted AFM ordering of the Fe^{3+} and Cr^{3+} at ~256 K, (ii) a progressive spin reorientation transition, and (iii) an AFM ordering of Pr^{3+} sublattices at ~14 K. Compensated temperature of ~135 K was observed for this material. Surprisingly, a distinct "diamagnetism-like" behaviour evolved in the low-temperature region under small applied field values. Furthermore, irreducible representations of crystal symmetry were used to create the thermal evolution of magnetic crystal structures in distinct transition areas. A maximum change of 2.06 $Jkg^{-1}K^{-1}$ was observed in magnetic entropy when the magnetic field was changed between 0 and 90 kOe.

Earlier in 2010, B. Gray *et al.* [5] investigated the electrical and magnetic states of an artificial double perovskite, La_2FeCrO_6 using element-resolved polarized X-ray probes. Using unit-cell level control of thin film growth on $SrTiO_3$ (111), the rock salt double perovskite structure could be created for this material, which did not have an ordered perovskite phase in bulk. Even though the Fe and Cr were in the proper +3 valence state, the element-resolved magnetic studies show that the moments in the field were small and

there is no evidence of substantial magnetic moments in the remanent state, contrary to related previous findings. Based on these data, this group argued that the ground state was consistent with the canted antiferromagnetic order.

In another recent investigation by N. Das *et al.* [40], Pr_2FeCrO_6 (PFCO) nanoparticles were synthesized with exceptional structural stability at a sintering temperature of 1500 K. A clear magnetic hysteresis loop was observed below 150 K (Fig. 2.6 (a)). The magnetic hysteresis loop revealed a low remnant magnetization of around 0.05 μ_B/f.u. Because of surface spin canting of nanoparticles, the M-H loops of Pr_2FeCrO_6 recorded at 50 and 150 K demonstrated the existence of strong remanent magnetization and a
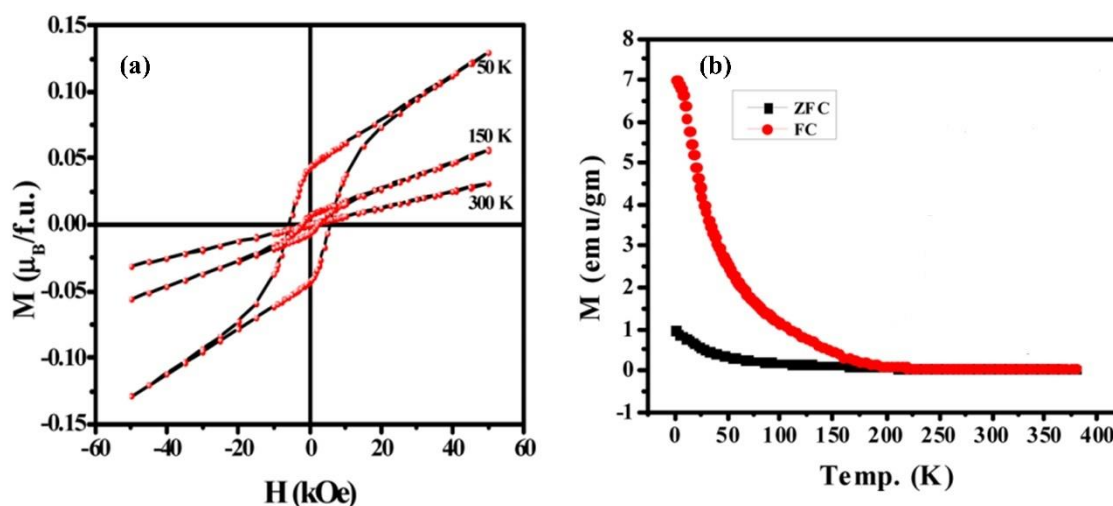
Fig. 2.6 (a) Isothermal magnetization of Pr_2FeCrO_6 measured at three different temperatures 300, 150, and 50 K in an applied magnetic field of 5 T. (b) ZFC and FC magnetization of Pr_2FeCrO_6 as a function of temperature measured in a magnetic field of 0.1 T [40].

significant coercive field. Pr_2FeCrO_6 bulk particles were paramagnetic at room temperature and undergo a magnetic transition below 240 K (Fig. 2.6(b)). Mössbauer study at 25 K showed a high hyperfine magnetic field of ~53 T at the iron nucleus, corresponding to a magnetic moment of near 6−7 μ_B/Fe. These two findings revealed that the Fe moments were ordered in a ferrimagnetic (nearly compensated or canted).

In 1998, using the laser-ablation approach, Ueda *et al.* [61] synthesized the ordered La_2FeCrO_6 as an artificial superlattice of $LaFeO_3$/$LaCrO_3$ (111) layers. Ferromagnetic spin order was observed in the $LaCrO_3$-$LaFeO_3$ superlattices, whereas their single-phase materials $LaCrO_3$ and $LaFeO_3$ possess an antiferromagnetic (AFM) state. Ferromagnetic coupling between Fe^{3+} and Cr^{3+} through oxygen has long been expected based on

Anderson, Goodenough, and Kanamori rules. Despite many studies of Fe-O-Cr–based compounds, random positioning of Fe^{3+} and Cr^{3+} ions had frustrated the observation of ferromagnetic properties. Ferromagnetic ordering was accomplished by forming artificial superlattices of Fe^{3+} and Cr^{3+} layers along the [111] direction.

Recently, V.M. Gaikwad *et al.* [62] have synthesized single-phase perovskite oxide Pr_2FeCrO_6 nanoparticles by low-temperature co-precipitation technique. The analysis of X-ray diffraction patterns using *Pbnm* space group showed that these nanoparticles exhibit larger structural distortion than their bulk counterparts. Because of the increased
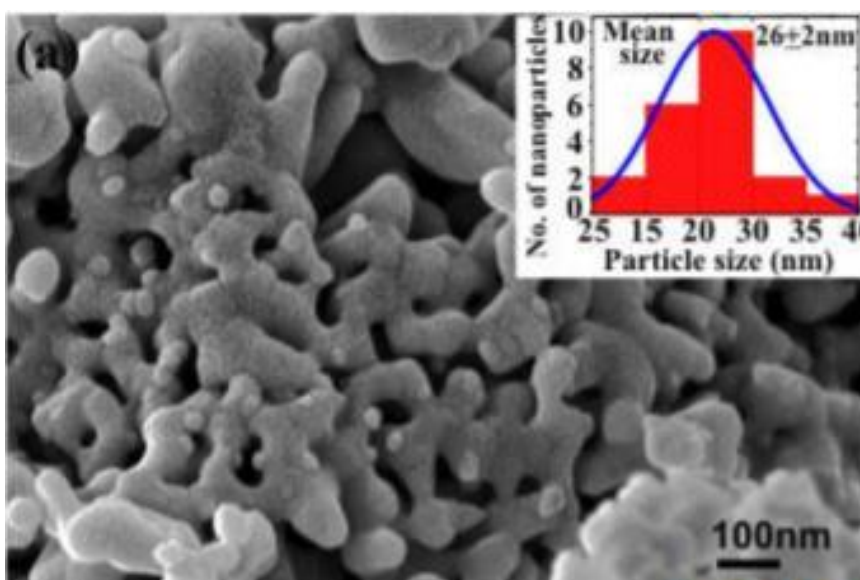
Fig. 2.7 (a) FESEM image of Pr_2FeCrO_6 spherical nanoparticles with inset showing size distribution plot [62].

precipitation rate during synthesis, the nanoparticles were agglomerated (Fig. 2.7(a)). According to the size distribution plot (inset of Fig. 2.7(a)), the mean particle size was found to be 26±2 nm. This group also investigated magnetic properties of Pr_2FeCrO_6 nanoparticles and observed the temperature fluctuation of magnetization (Fig. 2.8), which revealed that these nanoparticles undergo a ferrimagnetic transition at ~245 K, followed by substantial irreversibility (87%) under field (1 kOe) cooled conditions. Because of the surface spin canting of nanoparticles, the M- H loops recorded at 10 K and 50 K revealed strong remanent magnetization and a large coercive field. The optical absorption analysis revealed an energy band gap (E_g) of 2.13 eV, which is somewhat higher than the equivalent bulk system (1.4–2.0 eV).
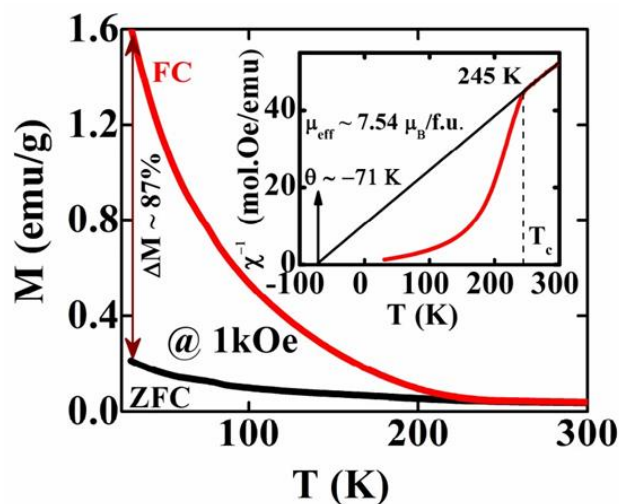
Fig. 2.8 Temperature dependent magnetization (25 to 300 K) of Pr_2FeCrO_6 nanoparticles at 1 kOe with inset showing Curie-Weiss fitting [62].
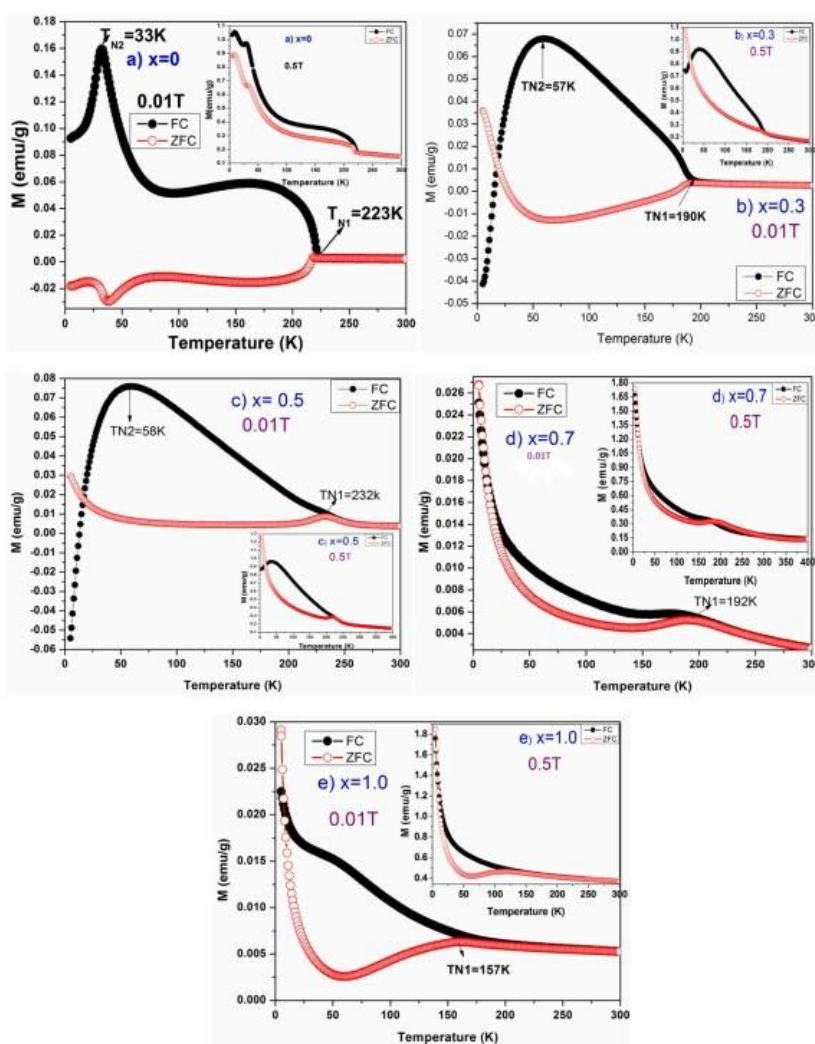
Fig. 2.9 (a-e) Temperature variation FC and ZFC magnetization curves of $NdCr_{1-x}Fe_xO_3$ at 0.01 T applied field. Inset figures show FC and ZFC magnetization curves at 0.5 T applied field [63].

In another recent study, J. Shanker *et al.* [63] investigated the magnetic properties of $NdCr_{1-x}Fe_xO_3$ perovskite. ZFC and FC magnetization curves of $NdCr_{1-x}Fe_xO_3$ as functions of temperature at 0.01 T and 0.5 T applied fields have shown in Fig. 2.9(a-e). According to the investigators, the first-order transition temperature (T_{N1}) varied depending on the composition. For samples with x = 0, 0.3, 0.5, 0.7, and 1, the transition temperatures were estimated as T_{N1} = 223 K, 190 K, 232 K, 192 K, and 157 K, respectively. This group also observed that at temperatures below T_{N1}, ZFC and FC magnetization curves were bifurcated. Notably, the temperature-dependent magnetization plot of x = 0 sample exhibited strange complex nature for T $\leq$ T_{N1} and was symmetric with a reverse sign in low temperature.

In 2013, R. P. Maiti *et al.* [64] synthesized Y_2FeCrO_6 nanoparticles by a molten salt synthesis procedure. By TEM analysis, the authors determined the structure of the produced Y_2FeCrO_6 double perovskite. The particle diameter was determined to be in the range of 40 to 60 nm. Additionally, using a high-resolution TEM image, interplanar spacing was calculated and found to be 0.269 nm, which corresponds to the (1 2 1) plane. XPS analysis revealed the presence of Fe^{2+} and Cr^{2+} species in addition to Fe^{3+} and Cr^{3+} ions in these materials. Moreover, these particles exhibited ferromagnetic and relaxor-type ferroelectric transition. The magnetic characteristics of these nanoparticles were described using superexchange interactions between Fe^{2+}/Fe^{3+} and Cr^{2+}/Cr^{3+} and Kanamori–Goodenough coupling between Fe^{3+}/Cr^{3+}.

Computational methods using DFT based first-principles calculation have emerged as a new era in condensed matter physics. Using this method, it is possible to calculate the structural, thermal, elastic, electronic, magnetic and optical properties of solids with reasonable accuracy, enabling us to understand and predict the properties that are sometimes difficult to measure even experimentally. Nowadays, first-principles calculations based on DFT have become an essential and significant part of condensed matter physics and material science research. Apart from the experimental investigations, double perovskites have also intrigued many researchers in recent years to conduct comprehensive theoretical investigations to have a deep insight regarding the band structures and density of states of these materials.

The electronic and magnetic properties of La_2NiMnO_6 double perovskite compound were studied by H. Das *et al.* [6]. The authors considered the compound as a ferromagnetic insulator and carried out first-principles density functional calculations to understand the

ferromagnetic insulating behaviour in this compound and understand the origin of the dielectric anomaly that has been observed experimentally. The quick change was observed in the dielectric constant at H = 0 T, which occurs at a temperature below transitions temperature (T_c) because the magnetic moment was not fully developed near T_c due to thermal fluctuation. While at a lower temperature, the moment was fully developed and made the effect of coupling to phonon degrees of freedom appreciable enough to observe the jump in the dielectric constant. This was corroborated by the fact that the jump became closer to T_c upon applying a magnetic field, which helps to overcome the thermal fluctuation and improve the magnetization.

Recently, Sadhan Chanda et al. [65] investigated the electronic structure and magnetic properties of Dy_2NiMnO_6 (DNMO) using DFT simulations and compared the results with experimentally obtained values. The study demonstrated that when Coulomb repulsion was neglected, i.e., when U = 0, the ground state of Dy_2NiMnO_6 exhibited a half-metallic character with a limited density of states at the Fermi level (set to 0 eV) in the down-spin channel. The electronic band gap of Dy_2NiMnO_6 in the up-spin channel was found to 1.4 eV. This half-metallic behaviour contradicted their experimental findings, which indicated that DNMO was an insulator with a 1.62 eV direct energy band gap. It is widely established that the Local Density Approximation (LDA) and the Generalized Gradient Approximation (GGA) cannot accurately represent the ground state of perovskite oxides and other strongly correlated compounds. Authors claimed that the GGA+U computations' forecast was accurate. The optical band gap was determined to be 1.5 eV, almost identical to the value found experimentally in the UV-visible absorption spectra of Dy_2NiMnO_6. The sum of Ni and Mn magnetic moments in Dy_2NiMnO_6 was estimated to be 4.43 μ_B/f.u., and the total magnetic moment was determined to be 15 μ_B/f.u. Therefore, in this investigation, the magnetic, optical, and electrical properties of Nd_2FeCrO_6 and Gd_2FeCrO_6 double perovskites were calculated using the GGA+U technique in conjunction with GGA.

Earlier, in another investigation, M. Ullah et al. [66] used the full-potential linearized augmented plane wave technique to study the impact of spin polarization on the electrical and thermoelectric characteristics of the double perovskites La_2NiMnO_6 and La_2CoMnO_6. The investigations showed that La_2NiMnO_6 had a larger band gap energy than La_2CoMnO_6 in both the majority and minority spin states. It was seen that in the spin-up state, the electrical conductivity, thermal conductivity, and thermoelectric power

of both compounds rose with temperature, whereas in the spin-down state, they stayed unchanged. Total magnetic moments computed for both compounds indicated a strong ferromagnetic character.

In 2001, K. Miura *et al.* [67] calculated the band structure of La_2FeCrO_6 which is a d^5-d^3 system and discovered that although the ground-state magnetic ordering of La_2FeCrO_6 was ferrimagnetic in GGA, it became ferromagnetic when U_{eff} was applied in LDA+U. This group developed an explicit formula for superexchange coupling, validated the outcome of band-structure calculation, and observed the coexistence of FM and AFM contributions in La_2FeCrO_6.

According to this review, structural, optical, magnetic, and electrical properties of Re_2NiMnO_6 and Re_2FeCrO_6 based compounds have been widely investigated among the primary combinations of double perovskites ($Re_2B'B''O_6$). In this investigation, for the first time, Nd_2FeCrO_6 and Gd_2FeCrO_6 double perovskites nanoparticles were synthesized by adopting a facile sol-gel technique and extensive investigation on their crystallographic structure, optical and magnetic properties were conducted both experimentally and theoretically. The synthesis procedures and characterization methodologies are described in **Chapter 3**, and the results are presented in **Chapters 4, 5, and 6**.

CHAPTER 3
SAMPLE PREPARATION AND CHARACTERIZATION
TECHNIQUES

In this chapter, firstly the essential steps of synthesizing Nd_2FeCrO_6 and Gd_2FeCrO_6 double perovskites using sol-gel technique are presented. After that, number of experimental techniques applied for investigating the structural, morphological, magnetic and optical properties of the synthesized double perovskites have been discussed. Notably, to explore the properties of the synthesized materials, a number of relevant characterization techniques were employed, and these techniques were briefly described in this chapter.

3.1 Sample preparation

To synthesize perovskite oxide materials, various techniques are widely employed, including combustion, sol-gel, hydrothermal, and co-precipitation method. The double perovskites Nd_2FeCrO_6 and Gd_2FeCrO_6 were synthesized in this research using the sol-gel technique, which is highly cost-efficient, easy, and appropriate for the synthesis of homogeneous and crystalline powder [68]. This method involves combining readily oxidizing reactants, such as metal nitrates, with an organic chelating agent that serves as the reducing agent.

3.1.1 Synthesis of Nd_2FeCrO_6 double perovskite

As was already mentioned, in this investigation, facile sol-gel method was used to synthesize Nd_2FeCrO_6 double perovskite. A schematic of the synthesis technique is presented in Fig. 3.1. Stoichiometric amounts of analytical grade $Nd(NO_3)_3.6H_2O$ (Sigma-Aldrich, 99.9%), $Fe(NO_3)_3.9H_2O$ (Sigma-Aldrich, 99.95%) and $Cr(NO_3)_3.9H_2O$ (Sigma-Aldrich, 99%) and citric acid (CA) were used as precursor materials and dissolved separately in 40 mL of deionized (DI) water while stirring with a magnetic stirrer. The solutions were poured into a beaker and vigorously stirred for 20 minutes on a hot plate at 50 ℃ followed by the addition of aqueous ammonia to maintain the pH of the solution at approximately 6.5. Ethylene glycol (EG) was added to this mixture such that the molar ratios were adjusted to $(Nd^{3+}, Fe^{3+}+ Cr^{3+})$: (CA): (EG) = 1:1:4 and the temperature was maintained at around 80 ℃ for about 4 hours. The gel precursor was produced by heating the solution at a temperature of 200 ℃ in order to burn the organic parts. The resulting

gel was burned at a high temperature and the resultant brown powder was cooled down to room temperature, ground in an agate mortar and thereafter calcined at 800 ℃ for 6 hours.

Fig 3.1 Schematic representation of the synthesis of Nd_2FeCrO_6 double perovskite by sol-gel method.

3.1.2 Synthesis of Gd₂FeCrO₆ double perovskite

Double perovskite Gd_2FeCrO_6 was also prepared by adopting a citrate-based sol-gel technique. A schematic of the synthesis route is presented in Fig. 3.2. Stoichiometric amounts of analytical grade $Gd(NO_3)_3.6H_2O$ (Sigma-Aldrich, 99.9%), $Fe(NO_3)_3.9H_2O$ (Sigma-Aldrich, 99.95%) and $Cr(NO_3)_3.9H_2O$ (Sigma-Aldrich, 99%) and CA were used as precursor materials and dissolved separately in 40 mL of DI water while stirring with a magnetic stirrer. The solutions were put into a beaker and vigorously stirred for 20 minutes at 50 ℃ on a hot plate, followed by the addition of aqueous ammonia to keep the pH at around 6.5. After 4 hours, EG was added to this mixture ensuring the molar ratio of $(Gd^{3+}, Fe^{3+}+ Cr^{3+})$: (CA): (EG) = 1: 1: 4 to develop a polymeric-metal cation network. Then, the obtained gel precursor was burnt at elevated temperature to yield brown fluffy powder. Thereafter, the powder was ground by a mortar and calcined at 800 °C for 6 hours in air followed by cooling down to room temperature (RT).
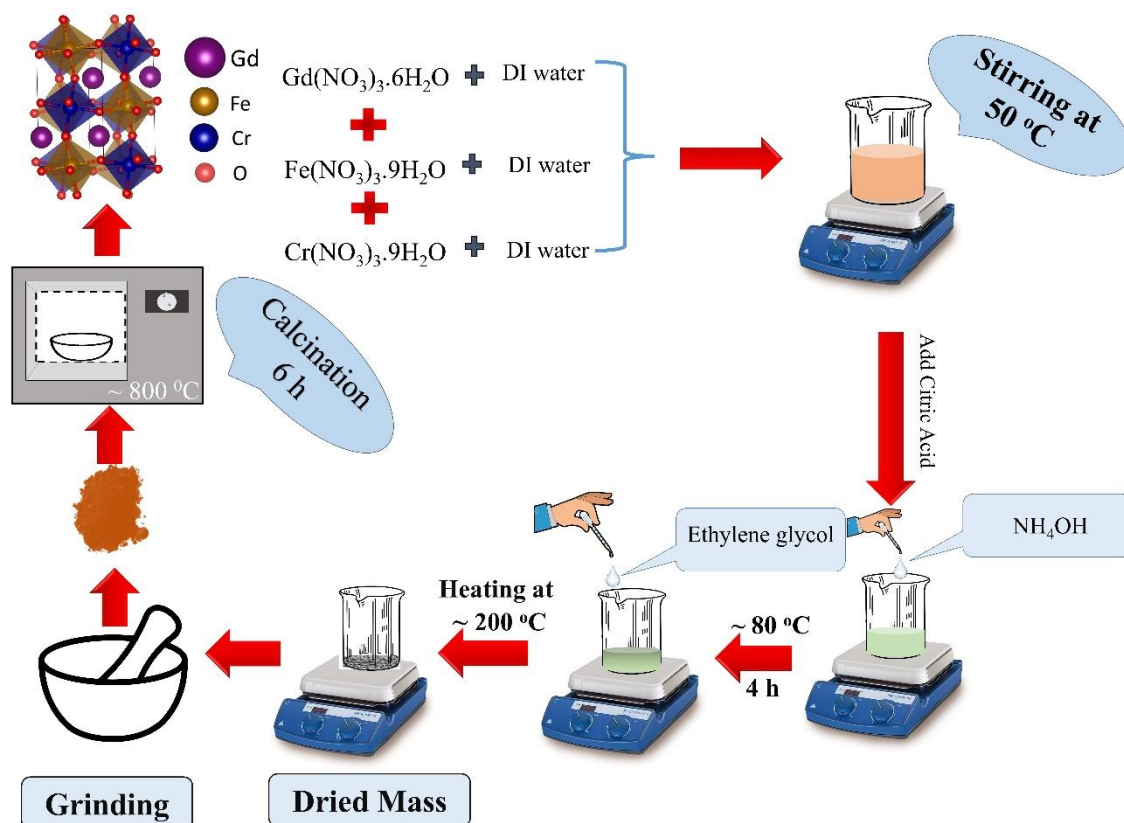
Fig. 3.2 Schematic representation of the synthesis of Gd$_2$FeCrO$_6$ double perovskite by sol-gel method.
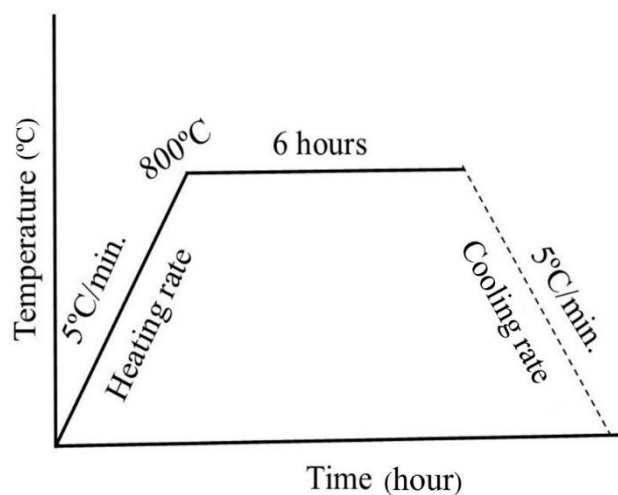
Fig. 3.3 Heating profile of step-by-step calcination process for this investigation.

The step-by-step calcination process of Nd$_2$FeCrO$_6$ and Gd$_2$FeCrO$_6$ double perovskites is shown in Fig. 3.3. For ferroelectric characterization, the calcined powder of Nd$_2$FeCrO$_6$ and Gd$_2$FeCrO$_6$ were pelletized into discs of thickness around 1.2 mm and diameter 10

mm using 5% polyvinyl alcohol (PVA) as a binder. Finally, the pellets were sintered at 850 °C temperature for around 20 min in air and cooled down to room temperature. The structural, magnetic, and optical properties of these as-synthesized double perovskites are investigated in **Chapters 5 and 6**.

3.2 Structural characterization techniques

3.2.1 Powder x-ray diffraction

Powder X-ray Diffraction (XRD) analysis is a laboratory-based method for determining a compound's structural phase and order of crystallinity. This method may be used to determine the dimensions of unit cells. The studied material is finely powdered, homogenized, and the bulk composition is calculated on an average basis. A cathode ray tube generates X-rays by burning a filament to generate electrons, then applying a voltage to accelerate the electrons toward a target and bombarding the target material with electrons. When electrons with adequate energy displace inner shell electrons of the target material, characteristic X-ray spectra are produced. These spectra are made up of various elements, the most prevalent of which being K_α and K_β. With $CuK\alpha$ (λ= 1.5406 Å) radiation, copper is the most popular target material for single-crystal diffraction. The diffracted X-rays are then filtered to generate monochromatic radiation, collimated to focus, and directed towards the sample. The interaction of the incident rays with the sample produces constructive interference (and a diffracted ray) when circumstances meet Bragg's Law [69] which is given by:

$$2d\sin\theta = n\lambda \qquad \cdots\cdots\cdots \text{(3.1)}$$

This law relates the wavelength (λ) of electromagnetic radiation to the diffraction angle (θ) and the lattice spacing (d) between two crystal planes in a crystalline sample. The diffracted X-rays that have been detected, processed, and counted are next examined. Scanning the sample over a range of 2θ angles should reveal all possible lattice diffraction directions due to the random orientation of the powdered material. Two identical wavelength and phase beams approach a crystalline material and scatter off two separate atoms inside it. The lower beam travels an additional $2d\sin\theta$ length. When its length is an integer multiple of the wavelength of the light, constructive interference occurs.

Powder X-ray diffraction patterns of as-synthesized Nd_2FeCrO_6 and Gd_2FeCrO_6 were recorded on a PANalytical Empyrean diffractometer. The X-ray source of this diffractometer emits radiation with wavelength of 1.540598 Å (Cu $K\alpha_1$) and 1.544426 Å

(Cu Kα_2). The diffractometer is calibrated with reference to a standard oriented Si wafer. For the usual structural phase analysis, a slow scan rate of 0.25 °/minute is used.

3.2.2 Rietveld refinement

The "Rietveld profile refinement" technique of evaluating powder diffraction data (XRD and Neutron Powder Diffraction) is named after Hugo Rietveld [70-73]. This technique entails fitting the parameters of a model to the measured "whole–profile", which is the intensity measured as a function of scattering angle. We fit a model to the data in Rietveld analysis. If the model is right, it should be able to forecast what the "true" intensity levels are. The Rietveld refinement is guided numerically using agreement indices, or R values [70]. The goodness of fit (χ^2) is,

$$\chi^2 = \left(\frac{R_{wp}}{R_{exp}}\right)^2 \qquad \cdots\cdots\cdots \quad (3.2)$$

where R_{wp} is weighted–profile R-value and R_{exp} is expected R-value. Rietveld refinement of the obtained XRD data of Nd_2FeCrO_6 and Gd_2FeCrO_6 double perovskites were performed by the FullProf computer program package [71] in order to determine the structural parameters.

3.3 Raman spectroscopy

Raman spectroscopy is a flexible technique for analyzing a broad variety of substances. This spectroscopy is called for its creator, C. V. Raman, who co-authored the original article on the method with K. S. Krishnan [72]. It overcomes the majority of the drawbacks of existing spectroscopic methods. It may be used to both qualitative and quantitative data. The frequency of scattered radiations may be measured for qualitative study, while the intensity of scattered radiations can be measured for quantitative analysis.
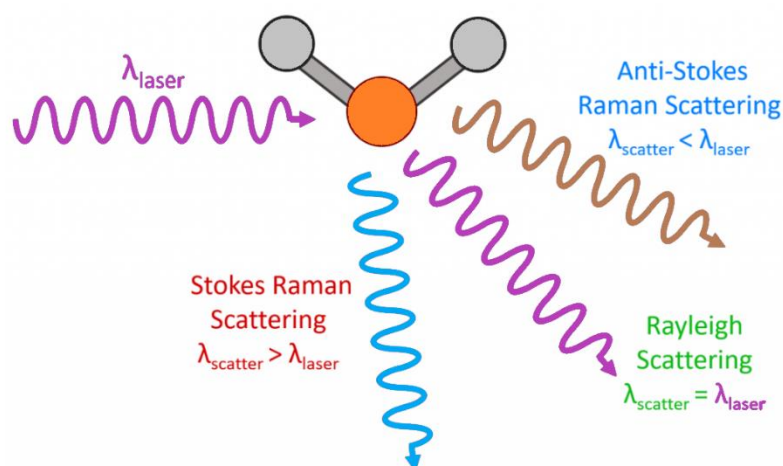
Fig. 3.4 Schematic diagram of basic principle of Raman Spectroscopy.

In Raman spectroscopy, a monochromatic laser beam is used to illuminate the sample, which reacts with the molecules and causes light to be dispersed. A Raman spectrum is made up of scattered light with a frequency that differs from that of the incoming light (inelastic scattering). Raman spectra are produced by the inelastic interaction of incoming monochromatic light with sample molecules. When monochromatic radiation hits a sample, it scatters in all directions after interacting with the molecules in the sample.

The Raman spectra of Nd_2FeCrO_6 and Gd_2FeCrO_6 double perovskites were measured in backward scattering configuration with 532 nm laser excitation using a MonoVista CRS+ Raman microscope systems (S&I) in the range from 5 cm^{-1} to 3000 cm^{-1}. In **Chapters 5 and 6**, the findings of the analysis are described.

3.4 Fourier transform infrared spectroscopy

Fourier Transform Infrared Spectroscopy (FTIR) is a technique for obtaining the infrared spectrum of absorption or emission of a solid, liquid or gas, which has a longer wavelength and a lower frequency than visible light and is measurable in a sample when submitted to infrared radiation (IR). High spectral resolution data is collected by FTIR over a wide spectral range. The goal of FTIR is to measure how much light a sample absorbs at each wavelength. "Dispersive spectroscopy" is a direct way to accomplish this. It allows monochromatic light to hit a sample, then measures how much of the light was absorbed for each different wavelength. At operation, the core notion is that various elements' bonds absorb light at different frequencies.

A typical FTIR spectrometer consists of a source, interferometer, sample container, detector, amplifier, A/D converter, and computer. Radiation from the source passes through the sample, via the interferometer, and into the detector. The signal is

subsequently amplified and converted to a digital signal by the amplifier and analog-to-digital converter, respectively. The signal is finally sent to a computer for Fourier processing. A block schematic of an FTIR spectrometer is shown in Fig. 3.5.
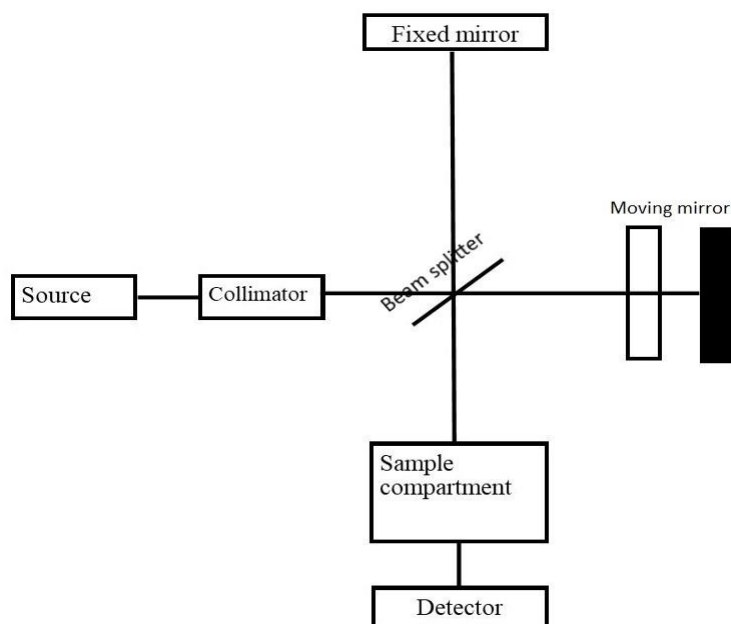
Fig. 3.5 Operations schematic of Fourier Transform Infrared Spectroscopy.

In this investigation, FTIR spectra of Nd_2FeCrO_6 and Gd_2FeCrO_6 samples were collected using Spectrum Two FTIR Spectrometer (PerkinElmer). The transmittance value of the samples was measured for IR radiation with wavenumbers ranging from 350-4000 cm^{-1} and the analysis of which are discussed in **Chapters 5 and 6**.

3.5 Thermogravimetric analysis

Thermogravimetric analysis (TGA) is an analytical method to evaluate a material's thermal stability and percentage of volatile components in it. This method monitors the weight change that happens when a sample is heated at a constant rate. Physical events such as phase transitions, adsorption, absorption, and desorption, as well as chemical phenomena such as thermal breakdown, chemisorption, and solid-gas interactions, are all revealed by this measurement.

In this work, the thermal stability of as-synthesized Nd_2FeCrO_6 and Gd_2FeCrO_6 double perovskites were investigated via TGA analysis using NETZSCH, STA 449 F3 Jupiter in

nitrogen atmosphere at a heating rate of 10 °C/min from 30 °C to 1000 °C. The TGA curves of Nd_2FeCrO_6 and Gd_2FeCrO_6 materials are analyzed in Chapters 5 and 6 respectively.

3.6 Morphological analysis techniques

3.6.1 Field emission scanning electron microscopy

Field Emission Scanning Electron Microscopy (FESEM) works on the same principles as a scanning electron microscope (SEM), but with the addition of a field emission electron source. Unlike SEM, which employs thermionic electron sources to create electron beams, FESEM uses a potential gradient to emit electron beams. It's a common method for determining topographical characteristics, surface morphology, crystal structure, crystal orientation, defect existence and position, as well as particle size, shape, and density.

The powder sample is placed on copper tape, which has three layers: the lowest one is a copper layer, the middle one is a carbon tape, and the top one is the copper tape where the sample is affixed, before being photographed using FESEM. The sample was then coated with gold for roughly 40 seconds using an ion sputtering process in an auto fine coater. The sample is coated with a 10 nm coating of platinum. The copper tape is then introduced into the FESEM after being positioned on a holder in the specimen chamber. The morphological examinations of the samples were aided by the micrographs generated from FESEM analysis. Field emission scanning electron microscope (XL30SFEG; Philips, Netherlands 50 and S4300; HITACHI, Japan) was used to analyze the surface morphology of Nd_2FeCrO_6 and Gd_2FeCrO_6 nanoparticles.

3.6.2 Scanning process and image formation

Primary electrons are focused and deflected by electronic lenses inside the high vacuum column to form a narrow scan beam that bombards the item. As a consequence, each area on the item emits secondary electrons. The angle and velocity of these secondary electrons have an impact on the object's surface structure. The secondary electrons are caught by a detector, which generates an electrical signal. This signal is amplified before being converted into a video scan picture that may be seen on a monitor. The samples' morphological evaluations were based on the pictures produced by FESEM analysis. Fig. 3.6 depicts a symmetric diagram of FESEM.
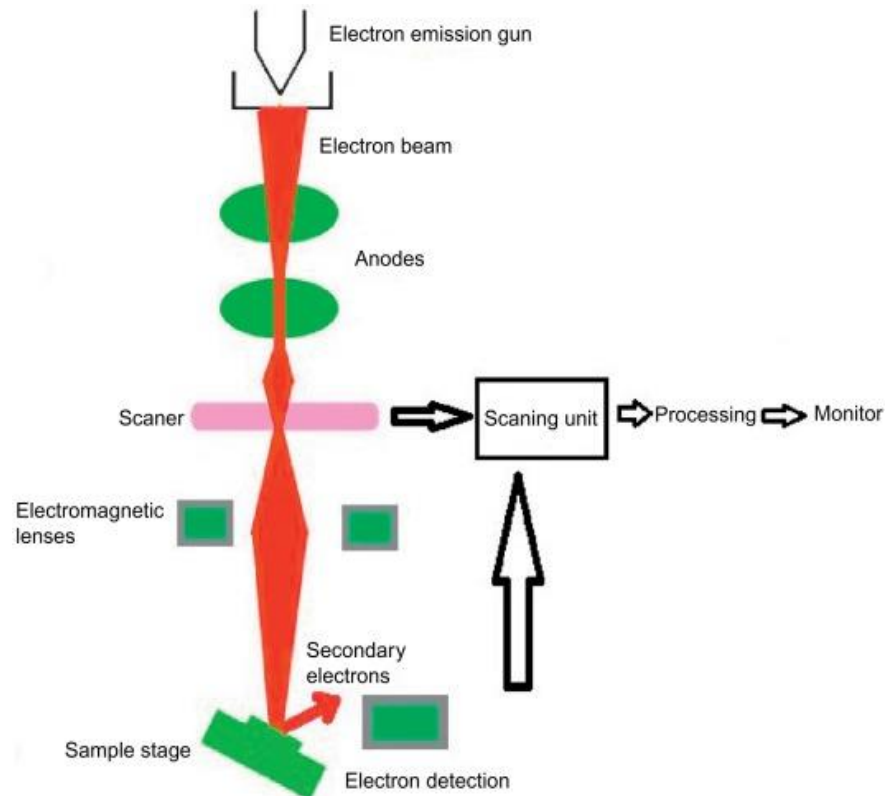
Fig. 3.6 A symmetric diagram of FESEM [73].

3.6.3 Transmission electron microscopy

Microscopes that use a beam of electrons to observe objects and create a greatly magnified image are known as transmission electron microscopes (TEMs). TEMs have the ability to magnify objects by more than 2 million times. The spatial resolution of an optical microscope is limited by the wavelength of its illumination, so the best optical microscopes can only discern features down to a hundred nanometers. To understand the fundamental properties of the patterned structures, a high spatial resolution is required. The idea of an electron microscope was first suggested by German physicists Ernst Ruska and Max Knoll to solve this resolution barrier. The first electron microscope was developed in 1931 [74] after De Broglie's popular electron wave-particle duality principle had been published in 1925 [75]. Louis de Broglie, inspired by Einstein's photon explanation of electromagnetic radiation, hypothesized that electrons have wave-like properties, with wavelengths much shorter than visible light:

$$\lambda = \frac{h}{p} \qquad \cdots\cdots\cdots \quad (3.3)$$

where h = 6.625×10^{-34} *J.s* is Planck's constant and *p* is the momentum of the particle. This eventually led to the notion of creating an electron microscope that could overcome the resolution limitations of standard optical microscopes by employing the electron wave. Electrons driven by a potential difference, V, have a wavelength, λ, that is proportional to their energy,

$$\lambda = \frac{h}{\sqrt{2m_o eV}} \qquad \cdots \cdots \cdots \quad (3.4)$$

where m_o and *e* are the rest mass and the charge of the electron, respectively. Nowadays, TEMs commonly use accelerated voltages of 60-300 kV, so the relativistic kinetic energy of electrons must be considered. When the relativistic influence is considered, the above equation becomes:

$$\lambda = \frac{h}{\sqrt{2m_o eV(1 + \frac{eV}{2m_o c^2})}} \qquad \cdots \cdots \cdots \quad (3.5)$$

where *c* is the speed of light in a vacuum.

The Thermo Scientific™ Talos™ F200X scanning/transmission electron microscope was used to investigate the size and crystallinity of the synthesized Nd_2FeCrO_6 and Gd_2FeCrO_6 nanoparticles. Selected area electron diffraction (SAED) was captured to check the crystallinity. High-resolution transmission electron microscope (HRTEM) images were also obtained under higher magnification.

3.7 X-ray photoelectron Spectroscopy

X-ray Photoelectron Spectroscopy (XPS) spectra are created by irradiating a material with an X-ray beam, such as a conventional Al K_α or Mg K_α source, while simultaneously measuring the kinetic energy and amount of electrons that escape from atoms on the material's surface.

When known-energy photons (typically X-rays) strike the surface (Fig. 3.7), one electron from the K-shell is ejected out, and the kinetic energy (K.E.) of this electron is measured using spectroscopy. The spectrum is displayed as a plot of the binding energy as a function of electron counting rate. Binding energy is one unique character of each element. The depth of penetration in materials needs to be kept within a few microns while hitting with X-ray. As a result of interactions between incident photons and surface atoms,

photoelectric emission of electrons occurs. The kinetic energy of the expelled electrons may be calculated as follows:

$$\text{Kinetic energy (K. E)} = hv - B.E. - \emptyset_s \quad \cdots\cdots\cdots \quad (3.6)$$

where hv is the energy of the photon, $B.E.$ is the binding energy of the atomic orbital from which the electron is ejected, and $\emptyset_s$ = work function of spectrometer. The innermost orbital appears to have a larger binding energy in the XPS spectrum than the outermost orbital. Binding energies of 1s orbitals increase with its atomic number following an empirical formula.
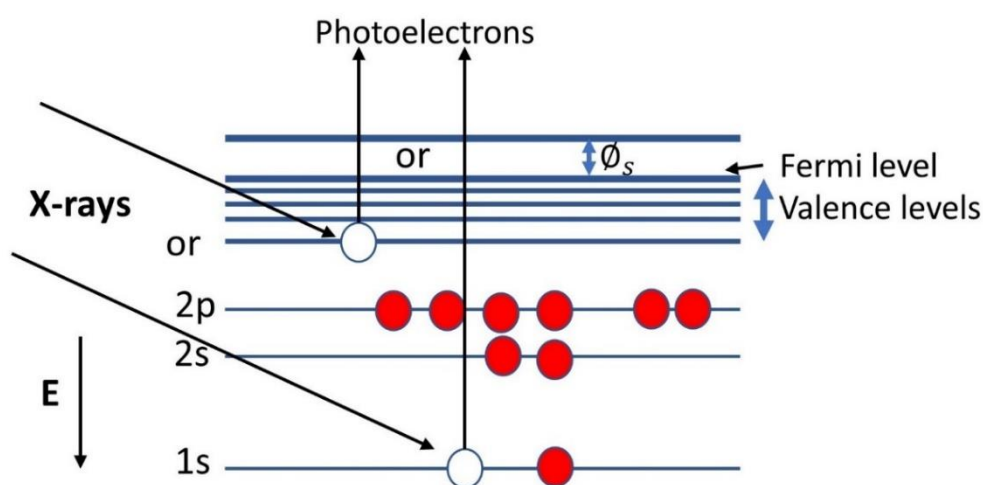
Fig. 3.7 Basic principles of X-ray photoelectron spectroscopy.

3.8 Magnetization measurement

3.8.1 Superconducting quantum interference device

Magnetic fields and characteristics may be measured in a variety of methods. Induction coils, flux gate magnetometers, magnetoresistive and Hall effect magnetometers, magneto-optical magnetometers, and optically pumped magnetometers have all been used as sensing techniques. The degrees of sensitivity vary from micro-Tesla to pico Tesla. Superconducting Quantum Interference Device (SQUID) is the most sensitive magnetic flux detector. In particular, it is the only method that allows precise measurement of the total magnetic moment of a sample in absolute units. Fig. 3.8 shows the block diagram of a typical direct current (DC) SQUID. The DC SQUID is distinguished from the radio frequency (RF) SQUID in the manner of biasing the Josephson junction and the number of junctions [76]. Because there are two junctions and shunt resistors, they must be

matched to within a few percentages. It's feasible to run SQUIDs with mismatched junctions, but performance would suffer dramatically [76].
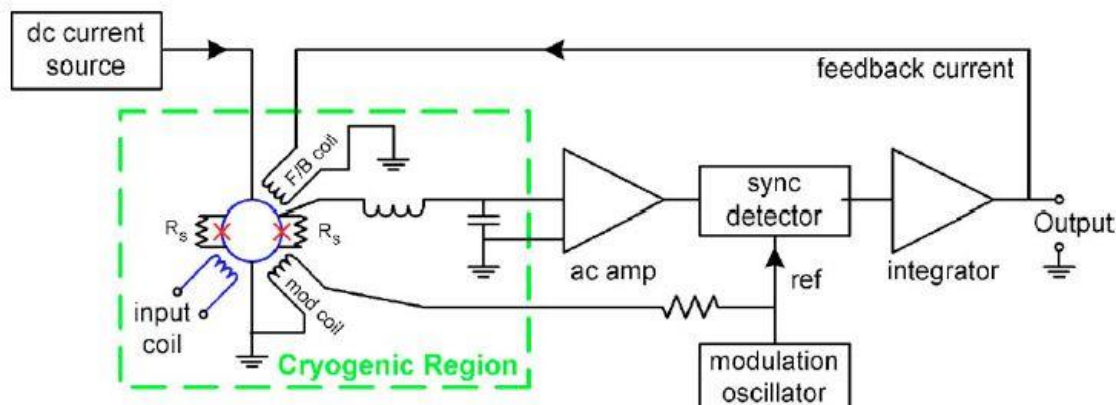
Fig. 3.8 Block diagram of a typical DC SQUID. The detection coil (connected to the input coil) is omitted for clarity [76].

Temperature dependent magnetization measurement of the as-prepared sample was performed using a SQUID magnetometer under 100 Oe applied magnetic field via ZFC and FC methods. Further, field dependent magnetization measurements of Nd_2FeCrO_6 nanoparticles were conducted at 300, 200, 100 and 5 K using the same SQUID. All magnetic measurements using SQUID magnetometer were performed at the Institute of Multidisciplinary Research of Advanced Materials, Tohoku University, Japan.

3.9 Optical measurement
3.9.1 UV-visible diffuse reflectance spectroscopy

Diffuse reflectance is a typical optical phenomenon utilized to gather molecular spectroscopic information in the UV-visible, near-infrared (NIR), and mid-infrared ranges. The collection and analysis of surface-reflected electromagnetic radiation as a function of frequency is often employed to produce powder spectra.

The reflectance and transmittance of a sample were characterized using Kubelka- Munk equations as a function of absorption and scattering [77]. Ideally one would prefer a function, like Beer and Lambert's law in transmission spectroscopy, to linearly relate analytic concentration with the reflectance properties of a diffusely reflecting sample. The function must be used is that derived by Kubelka-Munk:

$$F(R) = \frac{(1-R)^2}{2R} = \frac{K}{S} \frac{2.303 \in C}{S} \qquad \cdots\cdots\cdots \quad (3.7)$$

where, K denotes the absorption coefficient (twice the Beer and Lamberts law absorption coefficient), S is twice the scattering coefficient of the sample, $\in$ is the absorptivity, and

C is the analytic concentration.

The absorbance spectra of a molecule or chemical in a solution or as a solid are obtained using ultraviolet-visible (UV-vis) spectroscopy [80, 81]. The electrons in the ground state are aroused to the excited state levels when the molecules absorb enough light energy or electromagnetic radiation. The UV-vis energy region for the electromagnetic spectrum covers 1.1 to 6.2 eV, which relates to a wavelength ranging of 200-1100 nm. The Beer-Lambert Law is the principle behind absorbance spectroscopy [80].

In this study, a double-beam spectrometer with a light source (typically a deuterium or tungsten lamp), a sample container, and a detector was used to record the absorption and reflectance spectra of powder samples. A single source and monochromator are used in the double beam instrument, and then a splitter and a series of mirrors are used to direct the beam to a reference sample and the sample to be studied, allowing for more precise measurements. An ultraviolet-visible (UV–visible) spectrophotometer (UV-2600, Shimadzu) was used to obtain absorbance spectra of the as-synthesized Nd_2FeCrO_6 and Gd_2FeCrO_6 for wavelengths ranging from 200 to 800 nm.

3.9.2 Photoluminescence spectroscopy

Fluorescence and phosphorescence are used in Photoluminescence (PL) spectroscopy. In biochemistry and molecular biology, PL is extensively used to describe complicated molecules, their environment, and their position. The optoelectronic characteristics of semiconductors are also described using PL. The PL arrangement is the most straightforward type of optical system. The major components are shown in Fig. 3.9.

By defocusing the laser or lowering its output power, achieving an acceptable signal-to-noise ratio was generally feasible without causing harm. When a fixed-wavelength laser is substituted with a dye laser or another tunable unit, the setup may also be used for photoluminescence excitation spectroscopy, in which the exciting energy is changed and the monochromator is set at a fixed wavelength to monitor the resultant luminescence. Because it enables resonant excitation at key PL characteristics such as exciton peaks, this method benefits certain applications. The PL signal goes via a monochromator with a single grating that chooses a wavelength to transmit to the detector. The focal length of the monochromator determines the system's resolution or capacity to correctly detect energy, while the grating spacing determines the wavelength coverage. With an energy resolution of about l meV at mid-range, even a small 0.22 m monochromator with a 1200

groove/mm grating covers the visible to near infrared. There are many higher resolutions available.
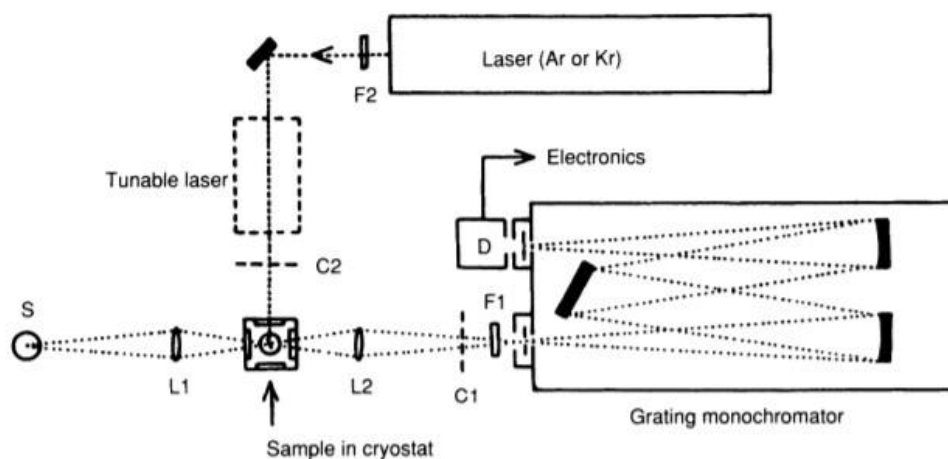
Fig. 3.9 Photoluminescence arrangement, with laser, sample and cryostat, monochromator, and detector (D). Lens L2 focuses the PL signal; filters Fl and F2 block unwanted laser light; chopper CI modulates the light for lock-in detection [81].

Steady-state PL spectroscopy of as-synthesized Nd_2FeCrO_6 and Gd_2FeCrO_6 double perovskites were carried out at room temperature using a Spectro Fluorophotometer (RF-6000, Shimadzu).

3.10 Ferroelectric loop tracer

A ferroelectric compound is defined by spontaneous polarization below the Curie temperature of ferroelectricity. The ferroelectricity may be verified experimentally by monitoring the P-E hysteresis loop. The basic P-E test system is based on the Sawyer-Tower circuit. The working principle of P-E test system is based on a simple phenomenon which is- When two capacitors are linked in series and AC voltage is delivered to each, the charge will be the same. The internal capacitance must be greater than the sample capacitance to achieve total saturation. If both capacitors are linked in series and an AC voltage is delivered, the charge on both capacitances must be the same. A standard capacitor is connected in series with the sample to be tested (device under test). When doing experiments in air, the air molecule breaks down at high fields, resulting in a spark between the electrodes. To prevent this, the capacitor must be immersed in an oil bath (silicon oil). In this investigation, the ferroelectric polarization of pellet shaped Nd_2FeCrO_6 and Gd_2FeCrO_6 double perovskites were traced using a ferroelectric loop tracer in conjunction with an external amplifier (10 kV) (Marine India).

3.11 Density functional theory

Density Functional Theory (DFT) is a popular approach for doing *ab initio* calculations on the structure of atoms, molecules, crystals, and their interactions. The DFT was established by Hohenberg and Kohn [82] and Kohn and Sham [83] to characterize the ground states of metals, semiconductors, and insulators. The DFT simulations deal with an interacting system of electrons in terms of its density rather than its many-body wave function. For N electrons in a solid, which follow the Pauli principle and repulse each other through the Coulomb potential, this indicates that the fundamental variable of the system relies mostly on the three spatial coordinates x, y, and z rather than 3N degrees of freedom.

Theorems established by Hohenberg and Khon in 1964 and a computational approach developed by Kohn and Sham in the following years underpin density functional techniques [82]. The researchers showed that total energy is a function of electron density, implying that one does not need to understand the complicated many-electron wave function but rather the electron density. The theorems are:

- **Theorem 1 (*Uniqueness*):** The ground state expectation value of any observable is a unique functional of the exact ground state electron density.
- **Theorem 2 (*Variational principle*):** Minimization of the total energy functional.

A number of terminologies required for DFT simulation are described below.

3.11.1 k-point sampling

The first Brillouin zone of a material is the area of reciprocal space near to the origin (0,0,0), and k-points are sample points inside that zone (often referred to as the Gamma point). Electronic states in bulk solids are confined to a set of k-points. In a periodic material, one k-point can account for an infinite number of electrons. Using a finite number of k-points, on the other hand, is appropriate if they are chosen to properly sample the reciprocal space [86, 87]. At k-points that are relatively close together, the electrical wave functions will be almost identical. This implies that the DFT expressions include a sum over k-points (or, more precisely, an integral over the Brillouin zone) that may be efficiently evaluated using a numerical method that sums over a limited number of specific Brillouin zone points. There are many implications for producing such points and associated weights for the summing. One may get an accurate estimate of the electronic

potential and the total energy of an insulator using these techniques, and this is accomplished by computing electronic states at a limited number of k-points. It is necessary to use a denser collection of k-points in metallic systems computations to correctly estimate the Fermi level. When the energies of two systems with different symmetries are compared, it is critical to obtain reasonable convergence regarding the k-point sample, for example if one is looking at the relative stabilities of a face center cubic (FCC) and a body center cubic (BCC) structure. Monkhorst and Pack developed one of the most often used methods for producing k-points [86].

3.11.2 Cutoff energy

For each infinite number of electrons in a solid, a wave function must be computed. Bloch's theorem makes advantage of a crystal's periodicity to limit an infinite number of one-electron wavefunctions to only the number of electrons in the crystal's unit cell [66]. Using this theorem, the wave function of an infinite crystal may be described in terms of the wave functions at reciprocal space vectors of a Bravais lattice. Bloch's theorem reduced the issue of an infinite number of electrons to one involving just the number of electrons in the unit cell (or half of that number, depending on whether the states are spin-degenerate or not) at a limited number of k-points selected to correctly sample the Brillouin Zone [68]. In theory, such an expansion requires an infinite number of plane waves. However, plane waves with lower kinetic energy usually play a larger role than those with very high kinetic energy. Thus, the plane wave basis set may have been condensed to contain only plane waves with kinetic energies less than a specified cutoff energy. When the basis set is shortened at a finite cutoff energy, an inaccuracy in the calculated total energy and its derivatives occurs. By raising the value of the cutoff energy, it is feasible to decrease the size of the mistake in a systematic manner. The cutoff energy should be raised in principle until the computed total energy converges within the specified tolerance.

To determine the structural, magnetic, optical and electronic properties of Nd_2FeCrO_6 and Gd_2FeCrO_6 double perovskites, the GGA and GGA+U approaches were used. However, for the DFT based first-principles calculation, a number of functionals/approaches are used by different researchers. Along with GGA, the other relevant approaches of DFT are given below.

3.12 Generalized gradient approximation

The Local Density Approximation (LDA) approach fails in circumstances where the density fluctuates rapidly, such as in molecules, since it approximates the real density's energy with the energy of a local constant density. The so-called Generalized Gradient Approximation (GGA) improves this by taking into account the gradient of the electron density. Symbolically this can be written as

$$E_{xc} = E_{xc}[\rho(r), \nabla\rho(r)] \qquad \cdots\cdots\cdots \quad (3.8)$$

This may result in a significant improvement over LDA findings, with accuracy approaching and in some instances exceeding that of correlated wavefunction approaches like MP2 [87]. There are two main methods of GGA: i) utilizing a large number of parameters to increase accuracy; and ii) fitting as few parameters as feasible while adhering to precise physical limitations. The GGA retains the characteristics of LDA, since the preceding terms are retained in the formalism, but in general, GGA enhances the over-binding of LDA while remaining chemically inaccurate and underestimating the electronic band gap.

3.13 Coulomb interaction or Hubbard potential

It is commonly known that first principles DFT calculations using LDA or GGA result in significant errors in estimated redox reaction energy for many transitions metal compounds. This inaccuracy is caused by the self-interaction error in LDA and GGA, which is not cancelled out in redox reactions in which an electron is moved between considerably different environments, such as between a metal and a transition metal or between a transition metal and oxygen. Consistent research attempts have been made to develop more accurate functionals through the use of corrective procedures or alternatives to density functionals. The DFT+U (Hubbard potential) approach is one of the corrective methods. The GGA+U technique has the benefit of being able to handle both delocalized and localized conduction band electrons in the same computational procedure. The GGA+U method has proven to be highly efficient and reliable tool for determining the electronic structure of systems with localized orbitals and a Coulomb interaction substantially bigger than the band width.

FIRST-PRINCIPLES PREDICTIONS ON Nd_2FeCrO_6

In this section, the structural, magnetic, electronic and optical properties of Nd_2FeCrO_6 (NFCO) double perovskite were investigated via DFT calculations using the generalized gradient approximation (GGA) approach. The effect of on-site Coulomb interaction on the ground state of NFCO double perovskite was also explored. Because of having unfilled d electrons, a strong electron correlation effect can be expected in this system and hence, this effect must be considered to conduct theoretical calculations [90, 91]. Therefore, in this investigation, 1 to 9 eV on-site Coulomb energies were incorporated with the localized d-orbital of Fe and Cr and the outcomes were analyzed extensively.

4.1 Computational details

Vienna ab-initio simulation package (VASP) [92, 93] software was used to carry out all the calculations for NFCO double perovskite by using the full-potential projector-augmented wave (PAW) approach [94, 95]. Initially, the GGA method [94] was adopted to evaluate the electronic exchange-correlation energy using the improved Perdew–Burke–Ernzerhof (PBE) functional. Since the GGA approach underestimates the band gap of insulators and semiconductors, later, the on-site Coulomb interaction was introduced using the GGA+U approach in order to properly describe the localized d electrons of Fe and Cr atoms [95]. For all calculations, Fe's $3s^23p^63d^64s^2$, Cr's $3s^23p^63d^54s^1$ and O's $2s^22p^4$ electrons were considered as valence electrons. Because partially filled f-states cannot be adequately represented by current DFT approaches and often fail to converge, the 4f electrons of the rare earth Nd atom were taken into account as the core electrons in structural relaxation [35, 98, 99]. However, Nd's 4f electrons were considered as valance electrons to investigate the effect of 4f spin on electronic structure, and spin orbit-coupling (SOC) only for NFCO. Integrations over the Brillouin-zone were performed by the tetrahedron method in a 6×5×4 Γ-centered Monkhorst–Pack k-point mesh. A plane-wave cutoff was set at 520 eV, and the self-consistent convergence criterion for energy was taken to 10^{-8} eV. The structure was completely relaxed until the forces were below 0.001 eV/Å.

To estimate the formation and decomposition energies, the total energy of the optimized unit cells of body-centered-cubic bulk Nd, Fe, Cr, molecular O_2, Nd_2O_3, Fe_2O_3, and Cr_2O_3

was used. The symmetry of the optimized structures was calculated by the spglib package [98]. The transition dipole moments were studied by Vaspkit [99]. The phonon dispersion was calculated by the Phonopy code [100] using a 2×2×1 supercell with a 2×2×2 k-mesh.

4.2 Effect of U on the ground-state
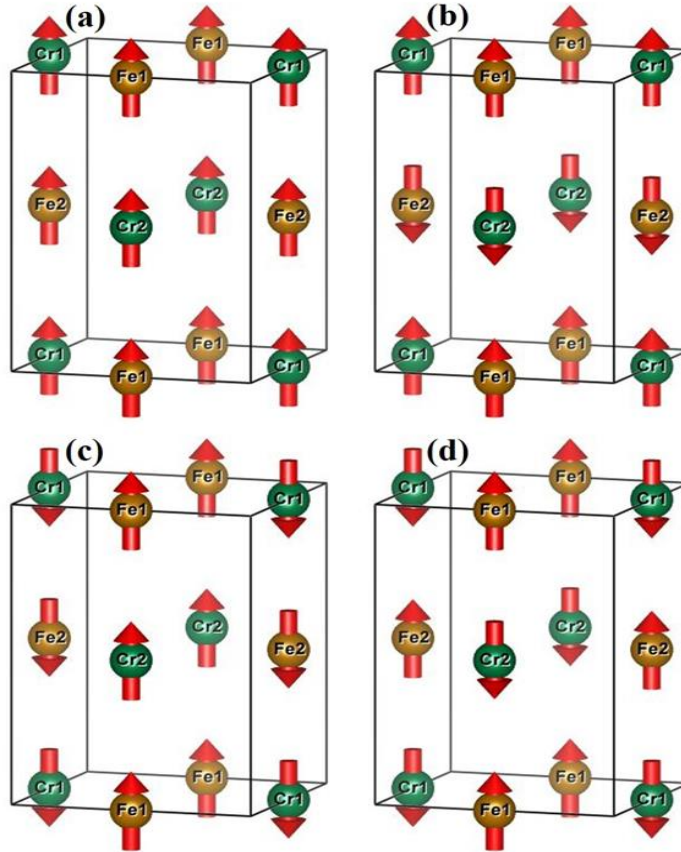
Fig. 4.1 Possible spin arrangements of Fe and Cr atoms in B-site ordered Nd_2FeCrO_6 double perovskite: (a) FM (b) A-type AFM and (c) C-type AFM and (d) G-type AFM (FiM).

To determine the lowest energy of spin order, the FM, A-AFM, C-AFM, and G-AFM arrangements of spin (shown in Fig. 4.1) were considered. The structure and atomic positions were fully relaxed for a set of U ranging from 0-9 eV for 3d electrons of Fe and Cr atoms. Fig. 4.2(a) shows the variation in total energy difference, ΔE (meV/f.u.) of the ground states of NFCO for various spin orders (as shown in Fig. 4.1) compared to the FM order and the variation corresponding to the change in U values. The total energy of all spin orders increases with U as the on-site occupation number in d orbital (and spin magnetic moment) of Fe/Cr found to be increased, which is consistent with Dudarev's formalism [101]. It should be noted that the Fe/Cr spin magnetic moments increase while the average induced magnetic moment in O atoms decrease from 0.09 μ_B to 0.07 μ_B with

increasing U indicating the attenuation of the strength of the magnetic exchange coupling via Fe–O–Cr interactions for larger U [102]. However, ΔE between FM and AFM spin orders decreases as U increases. For U < 6 eV, the G-AFM arrangement of Fe and Cr spins is energetically favorable while for larger U values (> 6 eV) the FM order becomes the lowest energy state. The mechanism could be understood from the variation of the difference in spin magnetic moments as shown in Fig. 4.2 (b). The variation and
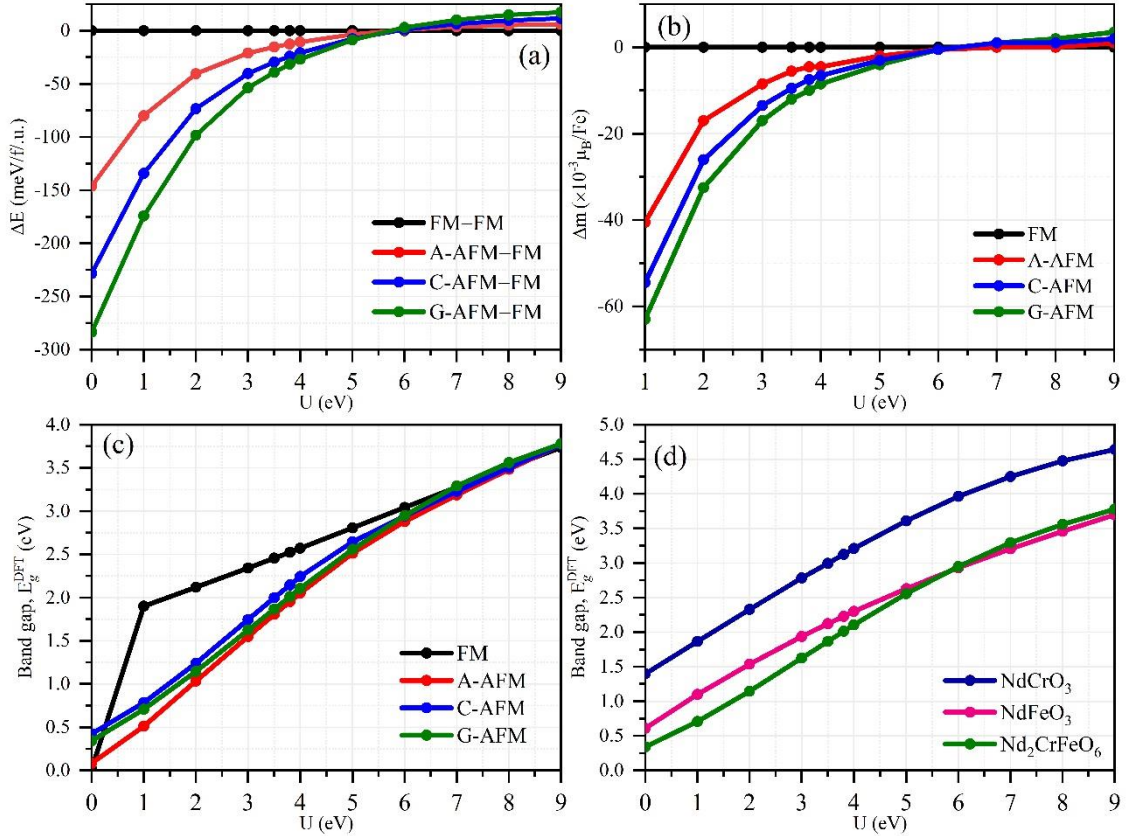
Fig. 4.2 Effect of U parameter on different ground state properties. (a) Variation of ground-state energy as a function of U for possible spin orders in Nd_2FeCrO_6 compared to the FM order. (b) Differences in spin magnetic moment (Δm) of the Fe site in AFM spin orders compared to the FM order. (c) Calculated band gap (for spin down channel) for different spin orders considered for Nd_2FeCrO_6. (d) Comparative plot of band gap for $NdCrO_3$, $NdFeO_3$ single perovskite, and Nd_2FeCrO_6 double perovskite considering their low energy spin (G-AFM) state.

turning of Δm curves are identical to the ΔE curves for AFM orders. It can be clearly seen that spin magnetic moments of AFM orders are approaching towards the FM baseline with increasing U and overtaking for U > 6 eV. A similar variation has been observed for Cr. The calculated band gaps for FM and AFM spin orientations are shown in Fig. 4.2 (c) and increase smoothly with an increment in U except for FM order at U = 0 eV. At U = 0 eV, the FM spin arrangement yields metallic behavior. This is the well-known artifact of

GGA in determining the electronic gap of semiconductors. Prior to the investigation of the physical properties of the Nd_2FeCrO_6 double perovskite, it is essential to choose a physically reasonable value of U which can adequately describe the electronic. Therefore, the parent single perovskites were studied since the experimental band gaps of these magnetic semiconductors had already been reported. For single perovskites, $NdCrO_3$ and $NdFeO_3$, the G-type AFM arrangement of spins demonstrated minimum energy for all values of U and the symmetry analysis of the optimized structures showed the orthorhombic phase with the *Pnma* space group. The calculated G-AFM ground states with orthorhombic structures for $NdCrO_3$ and $NdFeO_3$ were in agreement with experimental observations [103-105]. Since GGA (U=0) underestimated the band gap, the experimental band gaps ($E_g^{exp.}$) were compared with the calculated band gaps for different U values [106].

Table 4.1: GGA and GGA+U ($U_{Fe}= U_{Cr} = 3.50$ eV) calculated lattice parameters and band gaps for lowest energy (G-AFM) state of $NdFeO_3$, $NdCrO_3$ and Nd_2FeCrO_6. GGA+U calculated position of VBM, CBM, and charge transfer CT values for Cr/Fe cations to the oxygen anions obtained by Bader charge analysis [107].

	$NdFeO_3$		$NdCrO_3$		Nd_2FeCrO_6	
	U=0 eV	U=3.5 eV	U=0 eV	U=3.5 eV	U=0 eV	U=3.5 eV
a (Å)	5.664	5.676	5.561	5.586	5.439	5.465
b (Å)	7.797	7.824	7.724	7.770	5.615	5.627
c (Å)	5.455	5.472	5.417	5.449	7.754	7.802
β (º)	90	90	90	90	90.006	90.012
Space group	*Pnma*	*Pnma*	*Pnma*	*Pnma*	*P2₁/n*	*P2₁/n*
E_g^{DFT} (eV)	0.643	2.12	1.40	3.00	0.33	1.82
$E_g^{exp.}$ (eV)	2.06 [108]		3.10 [109]			
VBM (eV)	6.90		8.30		6.94	
CBM (eV)	4.78		5.30		5.12	
CT (eV/atom)	Fe = +1.67		Cr= +1.73		Fe= +1.70, Cr= +1.73	

Fig. 4.2(d) showed the variation in calculated band gap of $NdCrO_3$, $NdFeO_3$, and

Nd_2FeCrO_6. It was found that for U=3.50 eV (for Fe/Cr), the calculated band gap of $NdFeO_3$ and $NdCrO_3$ matched well with experimental values [108, 109]. For the same value of U i.e., for $U_{Fe} = U_{Cr} = 3.50$ eV, a band gap of 1.82 eV was obtained for double perovskite NFCO. Table 4.1 showed the calculated lattice parameters, symmetry of the optimized structures as well as the band gap values obtained by spin-polarized GGA and GGA+U calculations. As demonstrated in Fig. 4.2(d) and Table 4.1, the band gap of double perovskite NFCO (= 1.82 eV) was lower than its parent single perovskites, $NdFeO_3$ (= 2.12 eV) and $NdCrO_3$ (= 3.0 eV). To understand the reason of the low band gap in NFCO, valence band maxima (VBM), conduction band minima (CBM), and the charge transfer (CT) from Cr/Fe cations to O anion were calculated and have been shown in Table 4.1. Compared to $NdFeO_3$, the CT for Fe was found to be increased in case of NFCO, while for Cr it was similar to that of $NdCrO_3$. The higher ionicity of Fe may push the Fe-3d states in the CBM to a lower-energy position together with the almost unshifted O-2p states in VBM, resulting in the bandgap reduction. A previous investigation [110] on Bi_2FeCrO_6 (band gap 1.5 eV) double perovskite also demonstrated band gap reduction from their parent single perovskites following similar mechanism. It should be noted that the experimental band gaps of synthesized materials can be influenced by a variety of parameters, including synthesis conditions, particle size, the presence of vacancies, secondary phases, etc., [111–113] therefore, the experimental band gap owing to these effects could vary from the DFT-calculated results for perfect system [114]. In the subsequent investigation on NFCO double perovskite, G-AFM spin orientation was used as it gave the lowest energy ground state and U= 3.50 eV was considered for the 3d electrons of Fe and Cr atoms since this value satisfactorily described the electronic structure of the parent perovskite compounds.

4.3 Phase stability

Fig. 4.3 (a) and 4.3 (b) show the constructed phase diagram for Nd-Fe-Cr-O systems and the compound phase diagram for Nd_2O_3–Cr_2O_3–Fe_2O_3 systems, respectively. The NFCO phase was found to be on the convex hull's tie-line, suggesting that it is thermodynamically stable. Further, the formation energy per atom of NFCO was calculated using the following equation,

$$E_{atom}^{form} = \frac{1}{20}E_{bulk}^{Nd_2FeCrO_6} - 2 \times \frac{1}{2}E_{bulk}^{Nd} - \frac{1}{2}E_{bulk}^{Fe} - \frac{1}{2}E_{bulk}^{Cr} - 3 \times \frac{1}{8}E_{bulk}^{O_2} \quad \cdots\cdots\cdots \quad (4.1)$$
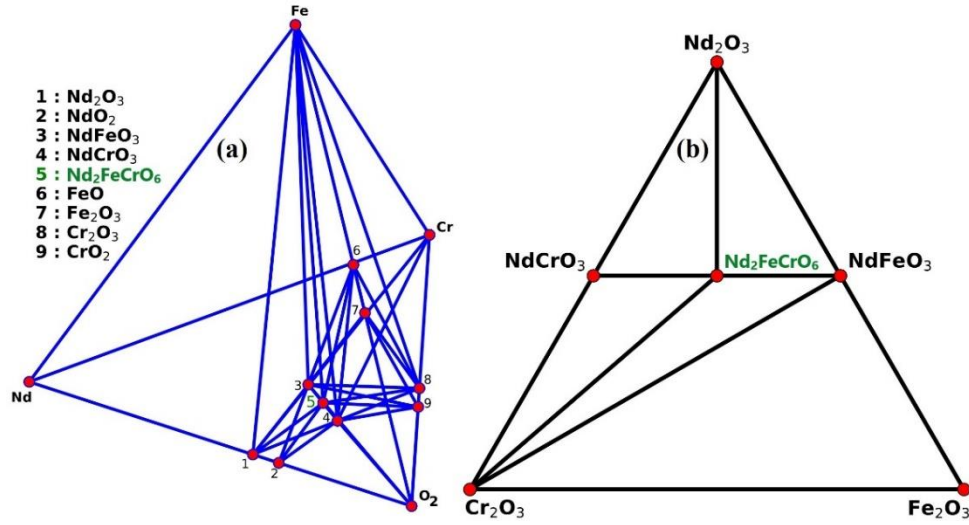
Fig. 4.3 The DFT-calculated phase diagram for the Nd–Fe–Cr–O system at T=0 K. The red circles are indicating the stable phases, these are connected by the black tie-lines that forming the convex hull. (b) The pseudo-ternary compound phase diagram of Nd_2O_3–Cr_2O_3–Fe_2O_3 systems, where the black tie-lines that forming the convex hull.

The calculated value of the formation energy, E_{atom}^{form} was found as -1.4 eV/atom. The negative value of E_{atom}^{form} indicated that this compound was formed by an exothermic process that needs less energy than the breaking of chemical bonds [115]. To evaluate the thermal stability of NFCO double perovskite, the breakdown energies of two possible phase-separation pathways of this double perovskite oxide were calculated, which was shown below.

$$\text{Path 1,} \ Nd_2FeCrO_6 \rightarrow NdFeO_3 + NdCrO_3 \qquad \cdots\cdots\cdots \ (4.2)$$

$$\text{Path 2,} \ Nd_2FeCrO_6 \rightarrow Nd_2O_3 + \frac{1}{2}Fe_2O_3 + \frac{1}{2}Cr_2O_3 \quad \cdots\cdots\cdots \ (4.3)$$
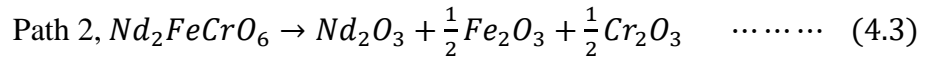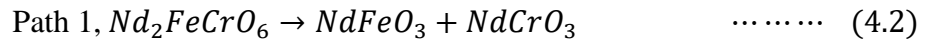
If the decomposition energy for any pathway (E_{DP}) was negative, it was not possible to observe a stable region in the phase diagram [116]. The estimated decomposition energies for NFCO double perovskite in both pathways were found to be 2.52 eV/f.u. (Path 1) and 0.86 eV/f.u. (Path 2) suggesting that this compound will not be decomposed spontaneously. This implied that the requirements for the thermodynamic equilibrium of NFCO double perovskite were satisfied.

Table 4.2: The calculated elastic constants (C_{ij} in GPa) of Nd_2FeCrO_6 double perovskite.

C_{ij}	1	2	3	4	5	6
1	281.7	131.8	117.0	0.0	2.0	0.09
2	131.8	238.8	113.9	0.0	2.0	0.0
3	117.0	113.9	275.0	0.0	-4.0	0.0
4	0.0	0.0	0.0	101.0	0.0	3.0
5	2.0	2	-4.0	0.0	85.0	0.0
6	0.0	0.0	0.0	3.0	0.0	81.0

To investigate the mechanical stability, elastic constants were calculated using the finite strain method [117]. The calculated elastic constants are summarized in Table 4.2. For monoclinic crystal, the independent elastic stiffness tensor was reduced to thirteen components, C_{11}, C_{22}, C_{33}, C_{44}, C_{55}, C_{66}, C_{12}, C_{13}, C_{15}, C_{23}, C_{25}, C_{35} and C_{46} in the Voigt notation [118]. For a mechanically stable structure, C_{ij} had to satisfy Born–Huang criteria [118, 119]. The mechanical stability criteria were given by [120]:
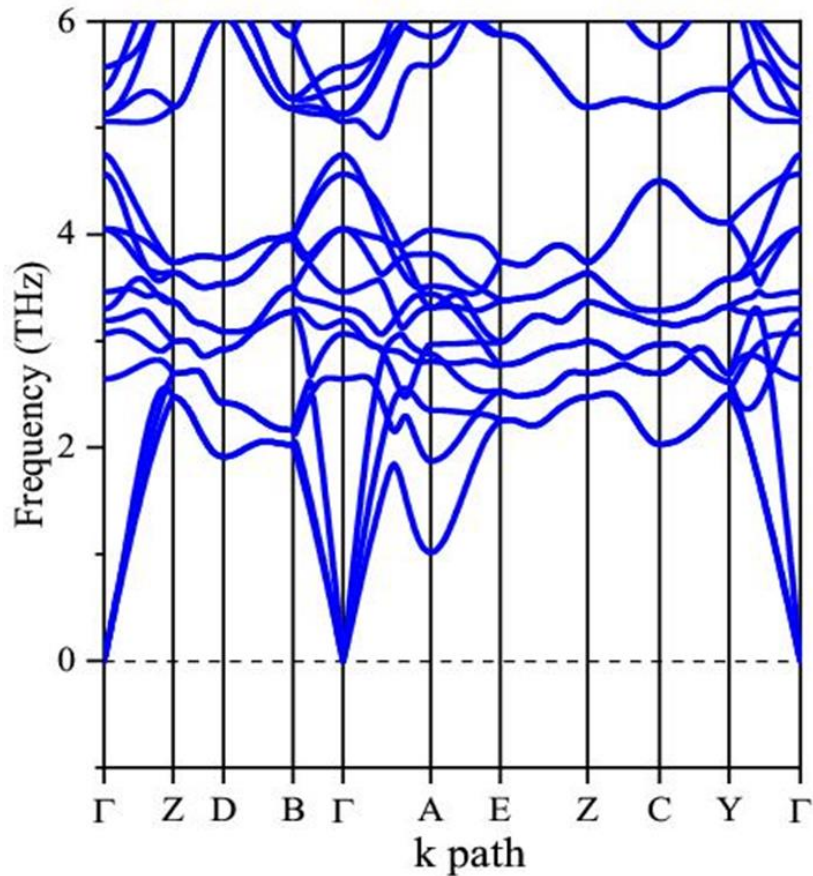
Fig. 4.4 The phonon dispersion curves of Nd_2FeCrO_6 double perovskite.

$C_{11} > 0, C_{22} > 0, C_{33} > 0, C_{44} > 0, C_{55} > 0, C_{66} > 0,$ .... (4.4)

$(C_{33}C_{55} - C_{35}^2) > 0, (C_{44}C_{66} - C_{46}^2) > 0, (C_{22} + C_{33} - 2C_{23}) > 0,$ .... (4.5)

$[C_{22}(C_{33}C_{55} - C_{35}^2) + 2C_{23}C_{25}C_{35} - C_{23}^2C_{55} - C_{25}^2C_{33})] > 0,$ .... (4.6)

$\{2[C_{15}C_{25}(C_{33}C_{12} - C_{13}C_{23}) + C_{15}C_{35}(C_{22}C_{13} - C_{12}C_{23}) + C_{25}C_{35}(C_{11}C_{23} - C_{12}C_{13})] - [C_{15}^2(C_{22}C_{33} - C_{23}^2) + C_{25}^2(C_{11}C_{33} - C_{13}^2) + C_{35}^2(C_{11}C_{22} - C_{12}^2)] + C_{55}(C_{11}C_{22}C_{33} - C_{11}C_{23}^2 - C_{22}C_{13}^2 - C_{33}C_{12}^2 + 2C_{12}C_{13}C_{23})\} > 0,$ .... (4.7)

The NFCO double perovskite met all essential stability criteria for monoclinic system. The phonon dispersion curve in Fig. 4.4 was used to analyze the dynamical stability of NFCO double perovskite. If there were no imaginary phonon frequencies in the entire Brillouin zone (BZ), the structure might be considered dynamically stable [120, 121]. In this case, any imaginary phonon frequency was not observed throughout the whole BZ, indicating that the structure was dynamically stable.

4.4 Magnetic properties

Table 4.3: Ground-state energy comparison ΔE (meV/f.u.) of FM, A-AFM, C-AFM and G-AFM states relative to FM state for $U_{Cr, Fe} = 3.50$ eV.

Order	$NdFeO_3$	$NdCrO_3$	Nd_2FeCrO_6
FM	0	0	0
A-AFM	-86	-13	-14
C-AFM	-168	-25	-27
G-AFM	-235	-36	-34
M (Fe/Cr) (μ_B)	3.99	2.66	4.05/-2.58
M_{total} (μ_B/f.u.)	0	0	2

Table 4.3 showed the ground-state energy comparison of different spin arrangements (as shown in Fig. 4.1) relative to the FM spin arrangement and magnetic moment per atom. As discussed above, NFCO double perovskite and its parent single perovskites $NdFeO_3$ and $NdCrO_3$ had G-type AFM order at the ground state. Due to the G-type AFM spin arrangement with $Fe^{3+}_\uparrow$-O-$Fe^{3+}_\downarrow$ and $Cr^{3+}_\uparrow$-O-$Cr^{3+}_\downarrow$ super-exchange interactions in $NdFeO_3$ and $NdCrO_3$, respectively, they did not possess any net magnetic moment. However, NFCO was quite interesting than $NdFeO_3$ and $NdCrO_3$ as it possessed a net magnetic moment of $\sim 2\mu_B$/f.u. due to the ordered distribution of Fe and Cr cations mediated by $Fe^{3+}_\uparrow$-O-$Cr^{3+}_\downarrow$ super-exchange interaction. Furthermore, the calculated total energies were used to estimate the magnetic ordering temperature (T_N) by mapping to the

classical Heisenberg Hamiltonian [122]:

$$H = \sum_{i,j} J_{ij} S_i S_j \qquad \cdots\cdots\cdots \quad (4.8)$$
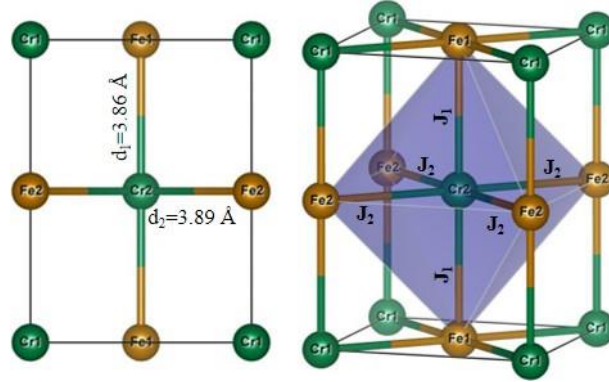
Fig. 4.5 In and out of plane bonds (d_1 and d_2) in $CrFe_6$ octahedron and magnetic exchange interactions (nearest neighbors, J_1 and next nearest neighbors J_2) in Nd_2FeCrO_6 double perovskite.

where $|S_i| = \sqrt{S_i(S_i + 1)}$ is the spin at site i and J_{ij} is the spin-exchange interaction parameter between i and j sites. Here, interactions up to the nearest neighbors J_1 and second nearest neighbors J_2 were considered. It should be noted that two types of bonds (in-plane and out of plane) with different lengths were present due to the distortion from the ideal $B'B''_6$ octahedron (as shown in Fig. 4.5). Therefore, the total energies per magnetic species may be expressed as,

$$E_0 + \sqrt{S_1(S_1 + 1)}\sqrt{S_2(S_2 + 1)}(2J_1 + 4J_2) = E_{FM} \qquad \cdots\cdots\cdots \quad (4.9)$$

$$E_0 + \sqrt{S_1(S_1 + 1)}\sqrt{S_2(S_2 + 1)}(-2J_1 + 4J_2) = E_{C-AFM} \qquad \cdots\cdots\cdots \quad (4.10)$$

$$E_0 + \sqrt{S_1(S_1 + 1)}\sqrt{S_2(S_2 - 1)}(-2J_1 - 4J_2) = E_{G-AFM} \qquad \cdots\cdots\cdots \quad (4.11)$$

where E_0 is the spin-independent part. The exchange parameters $J_1 = 0.62$ meV and $J_2 = 1.19$ meV were calculated by the above equations using $S_1 = 5/2$ and $S_2 = 3/2$ for the Fe^{3+} and Cr^{3+} spins. The positive values of exchange interactions were necessarily indicating the AFM nature of Fe-O-Cr interactions. For NFCO, magnetic phase transition temperature was estimated by the mean-field approximation, [123]

$$T_N = \frac{2}{3k_B}\sqrt{S_1(S_1 + 1)}\sqrt{S_2(S_2 + 1)}(2J_1 + 4J_2) \qquad \cdots\cdots\cdots \quad (4.12)$$

Since in B-site ordered double perovskite NFCO, the Fe-O-Cr interaction will be dominating, the calculated transition temperature 265 K was compared with experimentally observed magnetic transition at around 250 K due to Fe-O-Cr interaction in $NdFe_{0.5}Cr_{0.5}O_3$ perovskite [20, 21]. It should be noted that the classical mean-field

approach can give a rough estimation on transition temperature [124, 125]. To reveal the whole magnetic phase diagram, to understand the microscopic dynamic mechanism and to give a more qualitative picture of the magnetic properties [126], further investigation by classical atomistic spin dynamics method based on the DFT calculated exchange parameters is necessary.

4.5 Electronic structure

Fig. 4.6 showed spin-polarized band structures of NFCO for $U_{Fe} = U_{Cr} = 0$ and 3.5 eV, along the high symmetry directions in the first Brillouin zone for both spin up and spin down channels. The Fermi level (set to 0 eV) was shown by the horizontal line between the valence and conduction bands. The insulator nature of NFCO was predicted in both spin channels. For $U = 0$ (Fig. 4.6(a) and (b)), the valence band maximum (VBM) and conduction band minimum (CBM) were located at the same symmetry point (Y) in both spin up and down channels, indicating direct band gap of 2.19 eV and 0.32 eV, respectively. On the other hand, for $U_{Cr} = U_{Fe} = 3.5$ eV, in spin down channel, VBM was found to be shifted to the E points, mainly indicating the indirect nature with 1.82 eV gap. Notably, in down spin channel, Y point was located just 0.03 eV below the E point. Therefore, in double perovskite NFCO, the indirect band gap, 1.82 eV (E→Y) and direct band gap, ~1.85 eV (Y→Y) were comparable. The probability of transition either from E or Y points were understood by the calculated square of the transition dipole moment (P^2, transition probabilities between two states [99]) and was shown in the bottom panel of Fig. 4.6(d). At the E point, the transition probability was near to zero, whereas a strong probability was seen around Y point. Therefore, for double perovskite NFCO, the optical absorption could be initiated by direct Y→Y transition.

To understand the features of VBM and CBM, the total density of states (TDOS) and atom projected orbital decomposed density of states (PDOS) were analyzed. Fig. 4.7(a)-(d) displayed the TDOS of NFCO double perovskite and PDOS of Fe (3d) Cr (3d) and O (2p) orbitals, respectively. The Fe (3d) and Cr (3d) orbitals were found to be split into t_{2g} and e_g levels due to the FeO_6 and CrO_6 octahedral environment. It should be noted that following the local rotation of Fe/CrO_6 octahedra in the unit cell orientation, the $d_{x^2-y^2}$, d_{yz} and d_{xz} orbitals belonged to the t_{2g} states. On the other hand, d_{z^2} and d_{xy} orbitals belonged to e_g states [127].
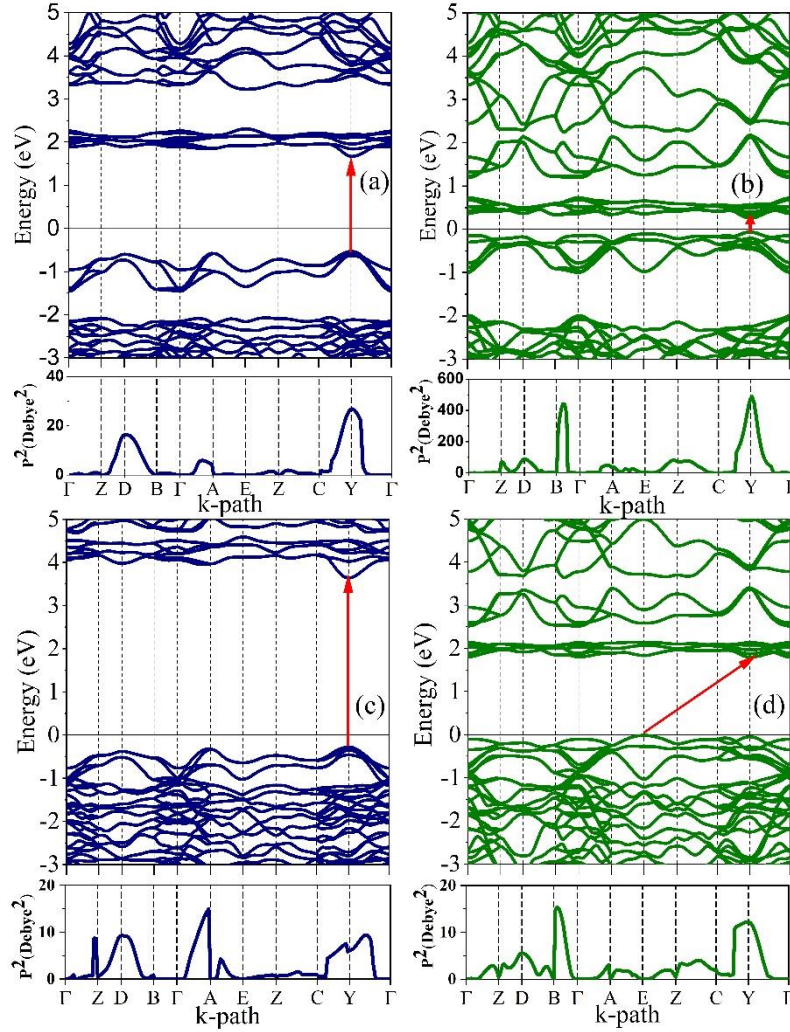
Fig. 4.6 Calculated band structure (top panel) and transition dipole moment (bottom panel) for $U_{Cr} = U_{Fe} = 0$ in (a) spin-up and (b) spin-down channels. (c) spin-up and (d) spin-down band structure and transition dipole moment for $U_{Cr} = U_{Fe} = 3.5$ eV.

In the valence band, the DOS in the range from -1 eV to 0 eV in the up-spin channel was dominated by O (2p) orbitals. Whereas, in the spin-down channel the VBM was made up of the hybridization of t_{2g} of Cr (3d) and O (2p) states. The CBM was constructed by the hybridization of Fe t_{2g} and O-2p orbitals. From Fig. 4.7(b), it was evident that both t_{2g} and e_g orbitals of Fe-3d were completely occupied by up electrons and range from -7.0 eV to -5.92 eV as a result of strong localization due to the electron correlation but in the spin-down channel t_{2g} and e_g states were completely unoccupied. This demonstrated $Fe^{3+}(t^3_{2g\uparrow}e^2_{g\uparrow})$ valance state [6] in NFCO double perovskite as illustrated in the inset of Fig. 4.7(b). In the case of Cr (3d), both t_{2g} and e_g orbitals were found to be empty in spin-up channel and in spin-down channel only the t_{2g} state was occupied, suggesting $Cr^{3+}(t^3_{2g\downarrow}e^2_{g\downarrow})$ configuration (inset of Fig. 4.7(c)). These results indicated the strong AFM

superexchange between $Cr^{3+}(t^3_{2g\downarrow}e^2_{g\downarrow})$ and $Fe^{3+}(t^3_{2g\uparrow}e^2_{g\uparrow})$ cations via O^{2-} anions.
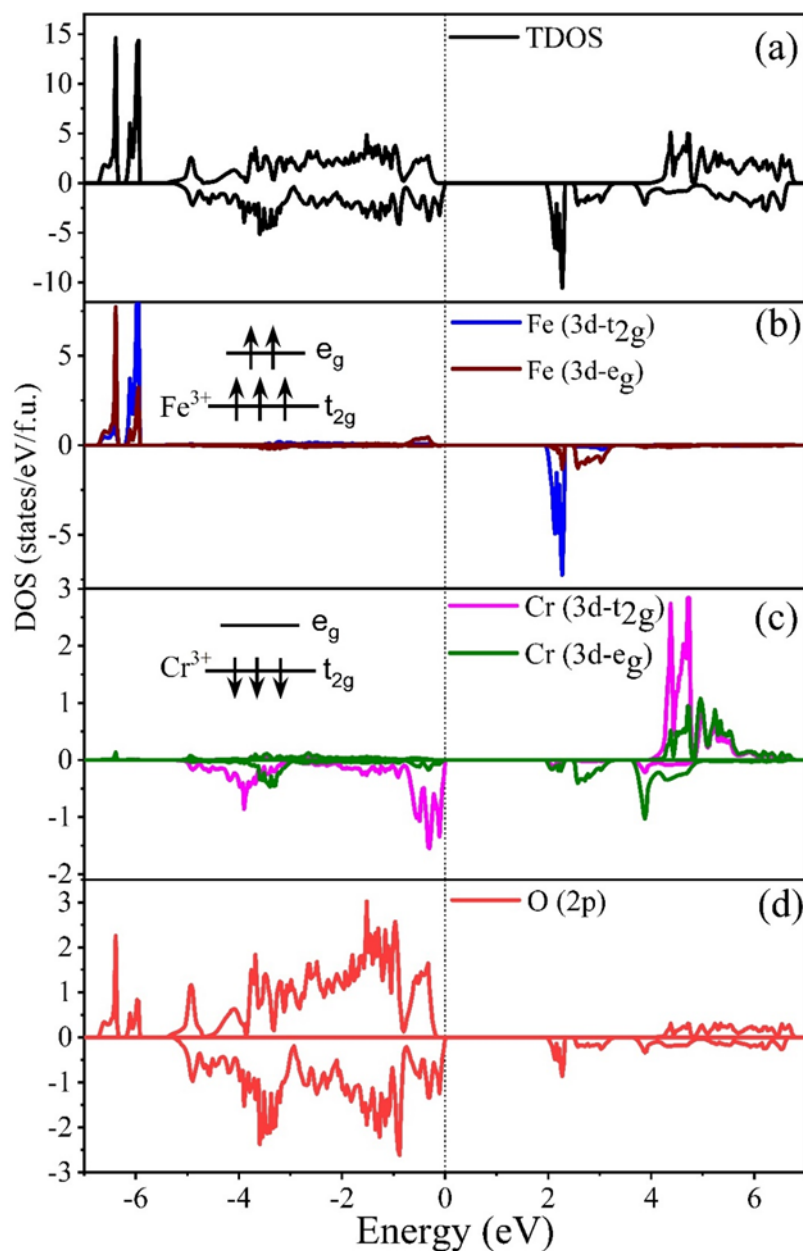
Fig. 4.7 (a) TDOS calculated by GGA + U for the ferrimagnetic ground state. (b-d) PDOS of Fe (3d), Cr (3d) and O (2p) orbitals respectively. Positive and negative DOS values stand for the up and down spin channel. Fermi level is set at zero energy.

For a deeper understanding of the bonding as well as magnetism, charge density analysis was carried out. Fig. 4.8(a) showed the total charge density distribution plot, indicating dominant Fe-O and Cr-O covalent bonding due to the presence of bond charges along the path between Fe–O and Cr–O. The magnetization density (Fig. 4.8(b)) was displaying
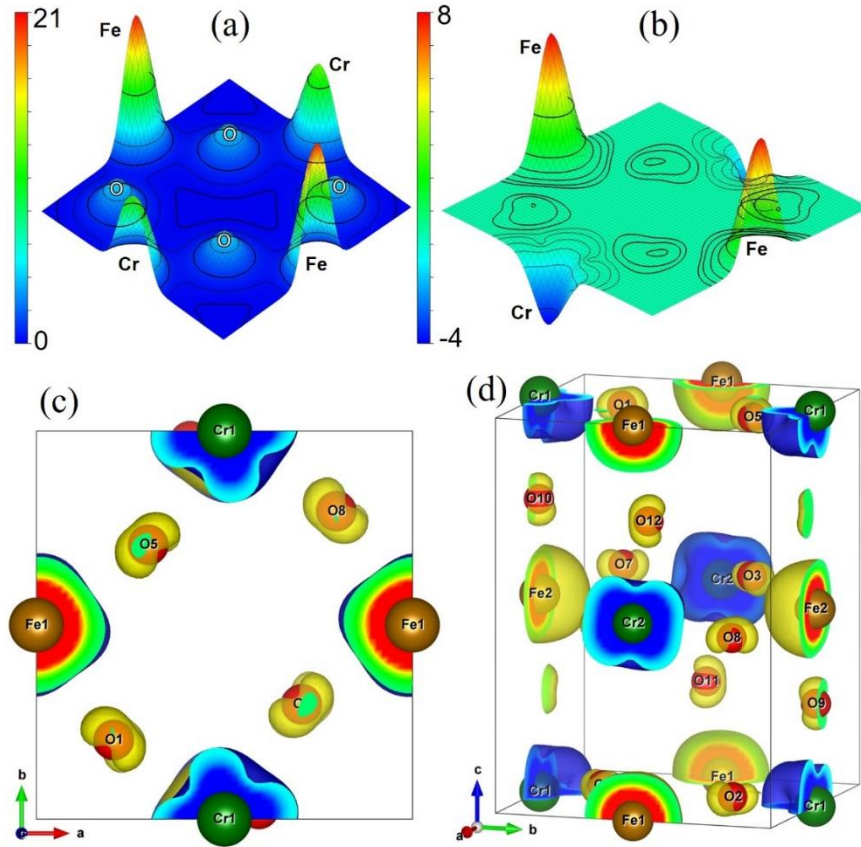
Fig. 4.8 (a) Total charge and (b) magnetization density plots. (c) Cross-sectional and (d) perspective view of three-dimensional (3D) magnetization density iso-surface plot at the same iso-value of ± 0.01 eV/Å^3. The light yellow and light blue colors represent the spin up and spin down states, respectively.

the antiparallel alignment of spins but with unequal magnitudes demonstrating FiM nature of NFCO. Fig. 4.8(c) and 4.8(d) showed cross-sectional and perspective views of 3D iso-surface of magnetization density. In analogy to the DOS, the spin density was also mainly contributed by Fe (3d) and Cr (3d) orbitals. The spherical shape around Fe atoms indicated $Fe^{3+}(t^3_{2g\uparrow}e^2_{g\uparrow})$ with $3d^5$ orbital character occupied by spin-up electrons [128]. On the other hand, only t^3_{2g} orbital were visible around Cr atoms, showing $Cr^{3+}(t^3_{2g\downarrow})$ character [129]. In addition, tiny spin densities were also appeared on the O atoms, due to the $Fe^{3+}_{\uparrow}$-O^{2-}-$Cr^{3+}_{\downarrow}$ superexchange coupling.

To investigate the effects of Nd's 4f spin and SOC, further calculations were carried out considering Nd's 4f electrons as valance electrons with U_{Nd}= 6.5 eV. Including Nd's 4f electrons in valence shell the G-AFM ordering remained as the lowest energy spin state, which was in agreement with the previous reports on ReFeO$_3$ and ReCrO$_3$ perovskites [130, 131]. Fig. 4.9(a) and (b) showed the comparative DOS plots using 4f electrons as core and valance electrons, respectively. VBM and CBM from Fig. 4.9 (b) showed no
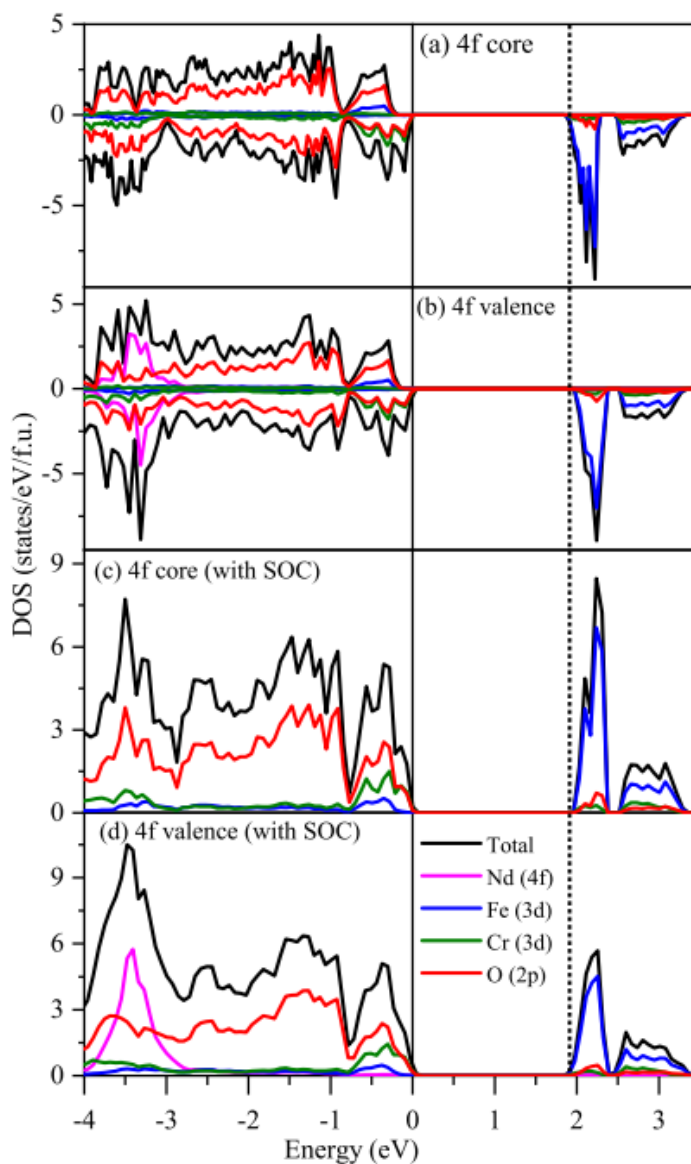
Fig. 4.9 Effect of Nd's 4f electrons and SOC on the electronic structure of Nd_2FeCrO_6. The calculated PDOS by considering; (a) 4f electron as core electron and (b) 4f electron as valance electron. The obtained PDOS including SOC by considering; (c) 4f electron as core electron and (d) 4f electron as valance electron.

contribution from the Nd (4f) orbital. Moreover, the band gap change (<0.8 eV) was found to be negligible. Similar results were found from the calculations with including SOC effect as shown in Fig. 4.9(c) and (b). Therefore, the effects of Nd's 4f spin and SOC were not so significant that change the conclusion with the results obtained by considering Nd's 4f electron as core electrons without SOC.

Table 4.4: Magnetic order (M), transition temperature (T_c) and optical band gap (E_g) of some $Re_2B'B''O_6$ materials.

Compound	B-site	M	T_c (K)	E_g (eV)	Reference
La_2MnCoO_6	ordered	FM	226	1.93	[132, 133]
La_2NiMnO_6	ordered	FM	220	1.42	[33]
Nd_2NiMnO_6	ordered	FM	195	1.57	[33]
Dy_2NiMnO_6	ordered	FM	105	1.62	[134]
La_2FeCrO_6	ordered	FiM	45	1.6	[135]
Pr_2FeCrO_6	partial	FiM	245	2.13	[62]
Nd_2FeCrO_6	ordered	FiM	265	1.85	This work

Before concluding, it could be worthwhile to compare the calculated magnetic properties and band gap of NFCO with other similar B-site ordered double perovskite oxides. Table 4.4 showed the magnetic order, transition temperature and band gaps of some Re containing B-site ordered double perovskites along with our DFT-calculated results. The obtained ground state was in agreement with Re_2FeCrO_6 and band gap was within the visible range like other candidates. Therefore, it was anticipated that this compound might be a potential candidate in various intriguing applications including spintronic memory devices, memristive high-performance data storage devices, light-emitting diodes, cryogenic magnetic cooling devices, solar cell and visible light driven photocatalysis.

CHAPTER 5

EXPERIMENTAL INVESTIGATION OF Nd₂FeCrO₆

The theoretical calculation presented in **Chapter 4** demonstrated the thermodynamic, mechanical, and dynamic stability of Nd₂FeCrO₆ (NFCO) double perovskite which intrigued to synthesize this double perovskite. The crystallographic structure along with the magnetic, electronic and optical properties of this sol-gel synthesized NFCO double perovskite is presented in this chapter.

5.1 Crystallographic structure analysis

Prior to conducting analysis, the tolerance factor and global instability index (GII) were calculated for the prediction of crystal structure of NFCO. The tolerance factor (t) of NFCO was obtained from the following relation [136, 137]:

$$t = \frac{r_{Nd}+r_O}{\sqrt{2}(\frac{r_{Fe}+r_{Cr}}{2}+r_O)} \qquad \cdots\cdots\cdots \quad (5.1)$$

Here, the ionic radii of Nd, Fe, Cr cations, and O anion are denoted by r_{Nd}, r_{Fe}, r_{Cr} and r_O, respectively. The value of $t \approx 1$ generally refers to the perfect cubic structure of double perovskites. If $t > 1$, the crystal structure is hexagonal and if t is less than 0.97, the structure can be either monoclinic or orthorhombic [136]. Here, the value of tolerance factor was found to be 0.94 for NFCO double perovskite, which means that there was a possibility for the structure to be either orthorhombic or monoclinic.

The global instability index (GII) of NFCO double perovskite was also computed using Structure Prediction Diagnostic Software (SPuDS) in order to determine its degree of stability [138]. The GII was calculated as follows [139]

$$\text{GII} = \sqrt{\frac{\sum_{i=1}^{N}(d_i)^2}{N}} \qquad \cdots\cdots\cdots \quad (5.2)$$

where d_i is the bond discrepancy index, which is the deviation of bond-valence sums (BVS) from formal valences of ions and N denotes the number of ions. Typically, GII value smaller than 0.1 v.u. (valence units) represents unstrained structures and structures having GII > 0.2 v.u. are reported to be unstable [139, 140]. Previous investigations

showed that for crystal structures with a GII value of greater than 0.02 v.u., high pressure was required during synthesis to achieve a stable phase [137, 140]. Notably, the GII value of NFCO was calculated to be 0.002 v.u. Thus, even under ambient pressure, it was able to achieve a stable double perovskite NFCO structure.
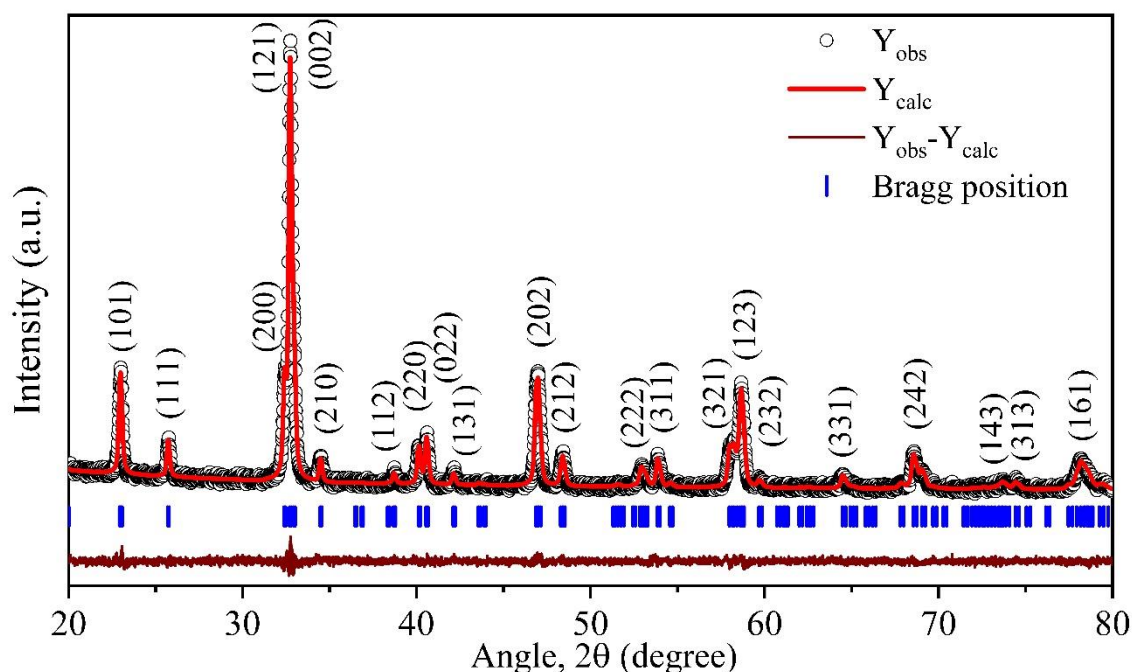
Fig. 5.1 Rietveld refined powder XRD spectrum of Nd_2FeCrO_6 nanoparticles at room temperature.

Rietveld refinement of the XRD pattern was carried out to confirm the predicted crystal symmetry and space group of NFCO perovskite [141, 142] using FullProf computer program package [71]. As the calculated value of tolerance factor was smaller than 0.97, an orthorhombic structure with a *Pnma* space group was initially considered during simulation. A monoclinic structure with *P2₁/n* space group was also considered for the refinement model. Notably, all diffraction pattern peaks were well indexed, indicating that the material was free of impurity phases. Though a better fitting was observed for *Pnma* space group (Fig. 5.1), it was still very difficult to get confirmation about the space group only by looking into the XRD patterns, especially if the B-site ordering was not perfect and β was close to 90º [56]. So, Raman spectroscopy was employed to complement X-ray diffraction experiments, providing detailed information concerning space group and octahedral distortion which will be addressed later on.

Table 5.1 Structural parameters and reliability (R) factors of Nd_2FeCrO_6 nanoparticles from Rietveld refinement of the XRD pattern.

Atom	Wyckoff site	x	y	z	Occupancy	R factors
Nd	4c	0.5437	0.25	0.5097	1	$R_p = 4.31$
Fe	4b	0.5	0	0	0.5	$R_{wp} = 5.45$
Cr	4b	0.5	0	0	0.5	$\chi^2 = 1.17$
O1	4c	-0.0154	0.25	0.4055	1	
O2	8d	0.2929	0.0392	0.7152	1	

Table 5.2 Bond lengths, bond angles and tilt angles for Fe/Cr-O and Fe-O-Cr, respectively obtained via Rietveld refined XRD pattern.

Bond length (Å)		Bond angle (°)		Tilt angle (°)
Fe/Cr-O1	2.00			
Fe/Cr-O2	1.98	Fe/Cr-O1-Fe/Cr	149.82	15.09
<Fe/Cr-O>	1.99	Fe/Cr-O2-Fe/Cr	155.12	12.44

The lattice constants of NFCO double perovskite for *Pnma* space group were $a = 5.523$ (0) Å, $b = 7.724$ (1) Å, $c = 5.435$ (2) Å, with cell volume 231.9 Å^3, as obtained from Rietveld refinement. Table 5.1 summarized the structural features acquired via Rietveld refining. The bond distances and angles included in Table 5.2 were notably similar to those reported for analogous double perovskites in an octahedral oxygen environment [40, 59]. The VESTA (Visualization for Electronic and Structural Analysis) [143] software was incorporated to model a 3D unit cell for NFCO using the structural parameters obtained from Rietveld refinement. The orthorhombic unit cell of NFCO in Fig. 5.2(a) demonstrated that the two transition metal cations were not precisely in the middle of octahedra, suggesting octahedral distortion. The distortion was also observed from an enlarged view of the two interlinked Fe/CrO_6 octahedra demonstrated in Fig. 5.2 (b) and (c). The average value of the tilt angle (Φ) was calculated to be 13.76° using the formula $\Phi = (180 - \theta)/2$, where θ is the bond angle between Fe/Cr–O–Fe/Cr, which further indicated the structural distortion in the NFCO unit cell [40]. The crystallite size of as-prepared NFCO double perovskite was calculated to be ~29 nm using the Debye-Scherrer equation [144, 145].
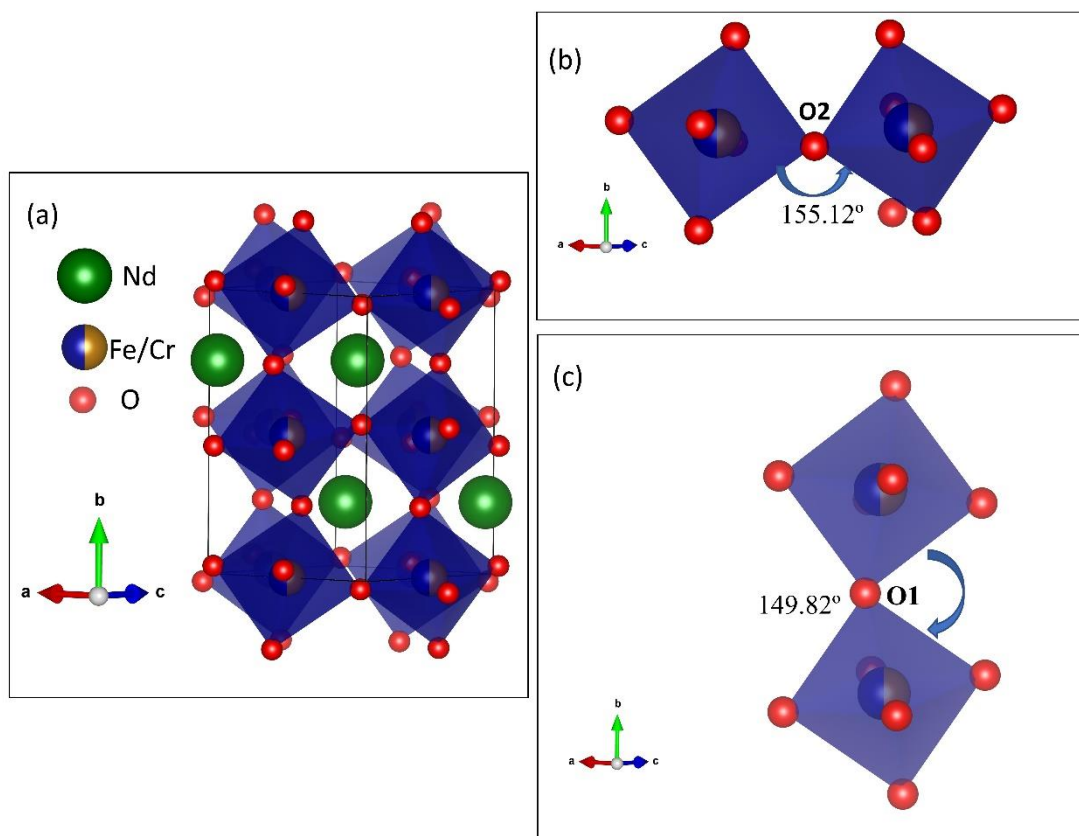
Fig. 5.2 (a) Schematic representation of the Nd_2FeCrO_6 orthorhombic unit cell with magnified view of interconnected Fe/CrO_6 octahedra (b) in the ac-plane and (c) along b-axis.

5.2 Vibrational properties

Raman spectroscopy was conducted at room temperature to analyze the crystal structure, spin-phonon coupling and cation disorder of as-prepared NFCO double perovskite (Fig. 5.3). Fig. 5.3 showed two strong modes at around 504 and 702 cm^{-1} which can be readily attributed to the B_g and A_g-like modes, respectively. Notably, asymmetry and broadness were observed in the two strong modes (B_g and A_g) which might have been influenced by several factors, including insufficient cationic ordering in $B'B''$ sites, average valance state of +3, different stretching vibrations having almost similar frequencies and so on [33]. The peak at 702 cm^{-1} can be associated with the stretching (breathing) vibrations of Fe/CrO_6 octahedra and the peak at 504 cm^{-1} corresponds to both bending and anti-stretching motions [146].
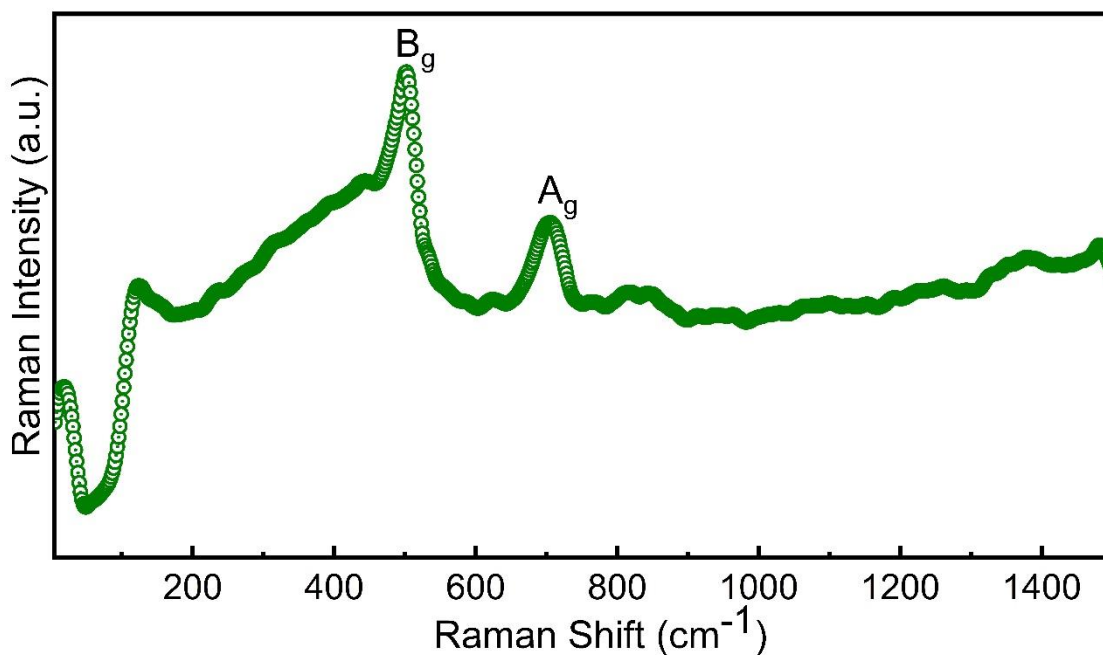
Fig. 5.3 Raman spectrum of Nd$_2$FeCrO$_6$ nanoparticles recorded at room temperature.

In addition, in the range of 800 to 1410 cm^{-1}, a multi-band was apparent (Fig. 5.3), which was ascribed to the second order multi-phonon process and decomposed into multiple separate modes. Notably, the modes near 835 and 1350 cm^{-1} were the overtones of fundamental stretching modes, B$_g$ and A$_g$, respectively. Such high frequency modes were also reported in Gd$_2$FeCrO$_6$ nanoparticles and La$_2$NiMnO$_6$ thin films [147, 148] and the occurrence of these modes further supports the possibility of NFCO nanoparticles being doubly ordered. A weak stretching mode near 120 cm^{-1} might be ascribed to the combinational effect of Nd-O stretching and Fe/CrO$_6$ tilting vibrations. Absence of any prominent mode around 377 cm^{-1} indicates the sample's phase purity, which was also confirmed from the XRD. The average bond length of Fe-O and Cr-O was also calculated by utilizing the most significant mode following the equation below [149]:

$$v(cm^{-1}) = 21349 \exp\left(-1.9176R(\text{Å})\right) \qquad \cdots\cdots\cdots \quad (5.3)$$

where, v and R are the stretching Raman frequency for Fe/Cr-O bond and the bond distance, respectively. The bond distance was found to be 1.954 Å by using this formula, which was consistent with the average bond distances of Fe/Cr-O (1.99 Å) determined by XRD.
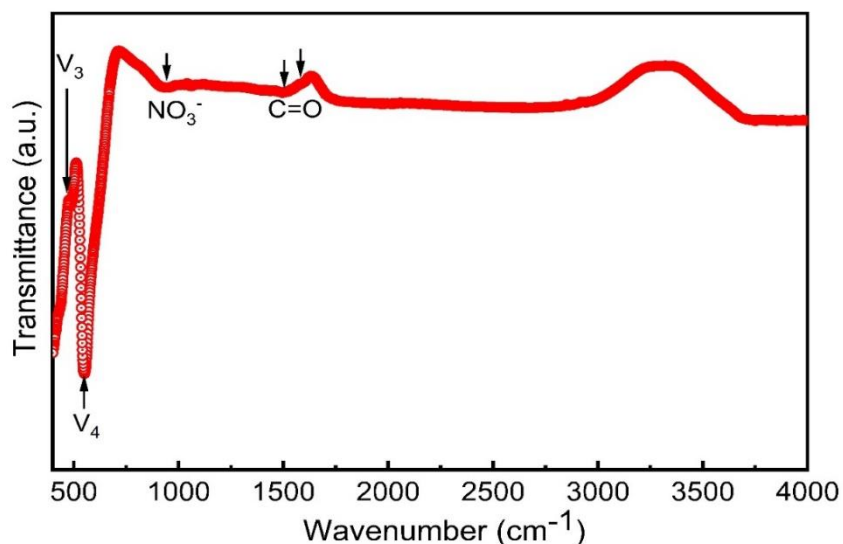
Fig. 5.4 FTIR spectrum of Nd_2FeCrO_6 nanoparticles recorded at room temperature.

For further analysis of the crystal structure, FTIR spectrum was recorded at room temperature where the spectrum demonstrated two distinct and well-defined bands corresponding to the presence of metal-oxygen band, which was a significant characteristic of perovskite materials [150] (Fig. 5.4). The strong transmission IR active bands located at 552 (V_4) and 490 (V_3) cm^{-1} were ascribed to the Fe/Cr–O stretching and bending vibrations, respectively [62, 150]. An additional band near 935 cm^{-1} referred to the presence of trapped NO^{3-} ions inside the sample [62]. The transmission bands observed in the higher frequency range can be attributed to the vibrations of C–O bands [62, 147].

5.3 Surface morphology analysis

The thermal stability of the as-prepared NFCO nanoparticles was evaluated by a TGA experiment in order to ascertain their viability in practical applications. The TGA curve in Fig. 5.5 confirmed the excellent thermal stability of NFCO, with a small weight loss of only ~8% up to 1000 ºC. The weight loss was quite negligible (~3%) in the temperature range of 600 to 1000 ºC which indicated that this temperature range will be reasonable for conducting calcination of NFCO nanoparticles and validated the choice of calcination temperature as 800 ºC during the synthesis. However, no endothermic or exothermic peaks can be seen in the DSC curve shown in Fig. 5.5, suggesting that no crystallographic phase change occurred in the temperature range of room temperature to 1000 ºC, confirming further the material's thermal stability.
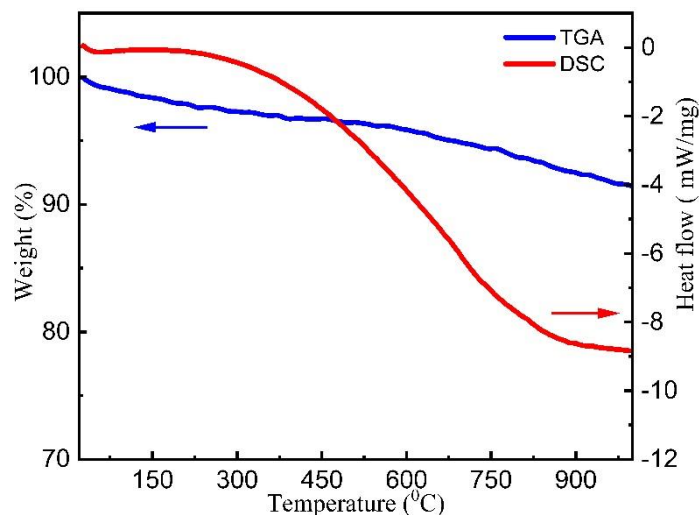
Fig. 5.5 TGA and DSC curves of Nd$_2$FeCrO$_6$ powders from room temperature to 1000 ℃ in N$_2$ with a heating rate of 10 ℃/min.

Fig. 5.6(a) presents the FESEM image of as-synthesized NFCO double perovskite demonstrating its homogeneous surface morphology. As shown in the corresponding particle size distribution histogram of Fig. 5.6(b), the particle size of as-synthesized NFCO ranges from ~40 to 130 nm, with an average size of ~70 nm. Energy Dispersive X-ray Spectroscopy (EDX) analysis was also performed with a view to determining the elemental composition of synthesized NFCO nanoparticles. Table 5.3 shows the experimentally measured as well as theoretically calculated mass and atom percentages.
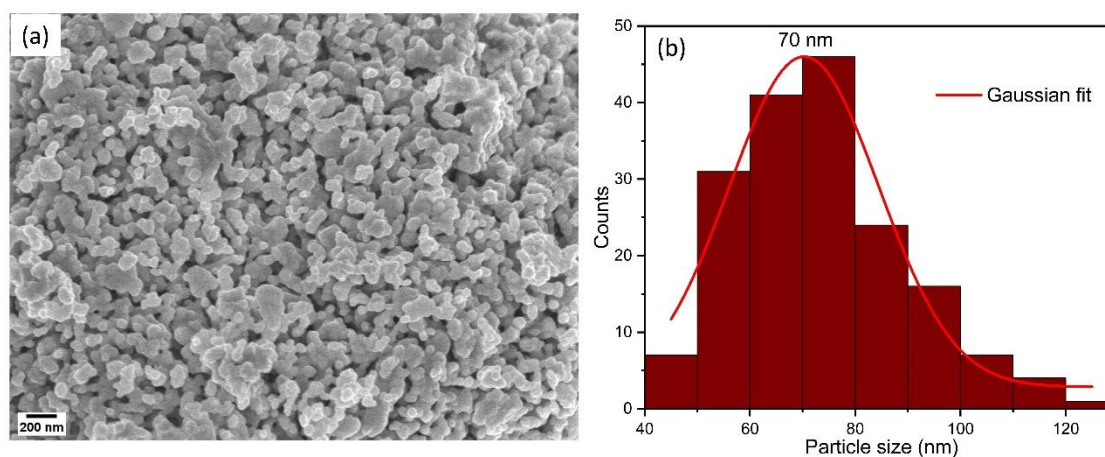
Fig. 5.6 (a) FESEM image of Nd$_2$FeCrO$_6$ nanoparticles with (b) particle size distribution histogram.

Notably, the experimentally obtained percentages of mass and atoms of desired elements such as Nd, Fe, Cr, and O in the as-synthesized NFCO nanoparticles were highly consistent with theoretical values, which further validated the successful synthesis of the intended sample.

Table 5.3 Mass and atomic percentages of Nd_2FeCrO_6 nanoparticles as obtained by EDX analysis.

Element	Mass (%) (Theoretical)	Mass (%) (Experimental)	Atom (%) (Theoretical)	Atom (%) (Experimental)
Nd	59.80	61.10	20	21.46
Fe	11.34	11.31	10	10.26
Cr	10.56	8.71	10	8.48
O	19.50	18.88	60	59.80
Total	100	100	100	100
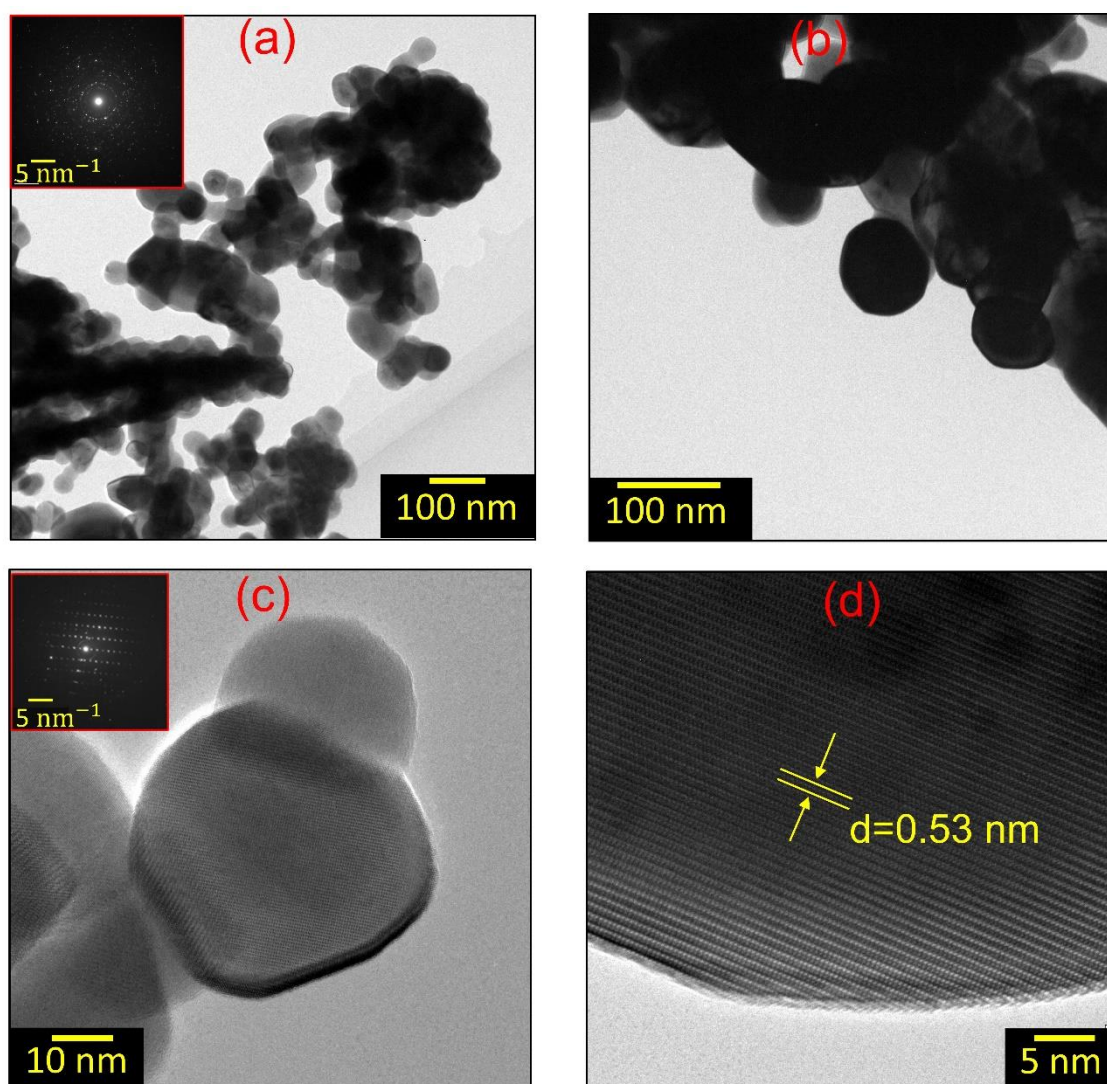
Fig. 5.7 (a) and (b) Bright field TEM images; (c) and (d) HRTEM images; insets show SAED pattern for Nd_2FeCrO_6 sample.

The morphological and nanostructural characterizations of NFCO were also performed using TEM and SAED techniques. Fig. 5.7(a) and (b) shows the general morphology of the NFCO nanoparticles. The TEM bright-field image demonstrated that the size of the

synthesized Nd_2FeCrO_6 nanoparticles was around ~55 nm which is consistent with the values obtained from FESEM imaging. Moreover, the polycrystalline nature of the as-synthesized sample was easily envisioned from the SAED pattern in the inset of Fig. 5.7(a). The HRTEM image (Fig. 5.7(c)) of NFCO showed the close-up view of a crystal with about 40 nm size and the subsequent SAED in the inset of Fig. 5.7(c) confirmed very good crystallinity. In Fig. 5.7(d) the clear lattice fringes with an inter-planar spacing of 0.53 nm can be observed.

5.4 XPS analysis

XPS is one of the most established characterization techniques for the determination of elemental composition and electronic state of solid materials. The core level XPS spectra of Nd-3d, Fe-2p, Cr-2p and O-1s in NFCO were identified and indexed to figure out the valance states of Nd, Fe and Cr ions (Fig. 5.8). The Nd-3d spectrum in Fig. 5.8(a) shows the spin-orbit splitting of $3d_{5/2}$ and $3d_{3/2}$ doublet states at 982.24 and 1004.6 eV, respectively indicating Nd^{3+} oxidation states [151]. An additional peak at 978 eV implied that some neodymium atoms existing at the surface were in metallic condition (Nd^0) [151]. The spin–orbit transitions of $Fe-2p_{3/2}$ and $Fe-2p_{1/2}$ binding energy peaks appeared at 710.57 and 724.55 eV (Fig. 5.8(b)), respectively and the doublet separation of 13.98 eV suggested that Fe has +3 oxidation state which was in good agreement with previous investigations [40], [147]. Between two major peaks, a satellite peak was observed at 719.25 eV which was also a distinguishing indication of Fe^{3+} state [40]. The occurrence of a small elevation adjacent to $Fe-2p_{3/2}$ peak confirmed the presence of Fe^{2+} oxidation state in NFCO. The XPS spectrum for Cr photoelectrons revealed two pairs of spin-orbit peaks (Fig. 5.8(c)). The lower and higher binding energy (BE) peaks for each $Cr-2p_{3/2}$ and $Cr-2p_{1/2}$ lines correspond to Cr^{2+} and Cr^{3+} ionic states, respectively [64]. The presence of mixed valances of Fe and Cr ions suggested the disordered distribution of Fe and Cr atoms in NFCO. As shown in Fig. 5.5(d), two peaks were observed in the XPS spectrum of the O-1s core level. The higher BE and lower BE peaks correspond to chemisorbed oxygen species (O^{2-}) and oxygen deficient regions (O^- and O^{2-} ions) in the NFCO nanoparticles, respectively [152].
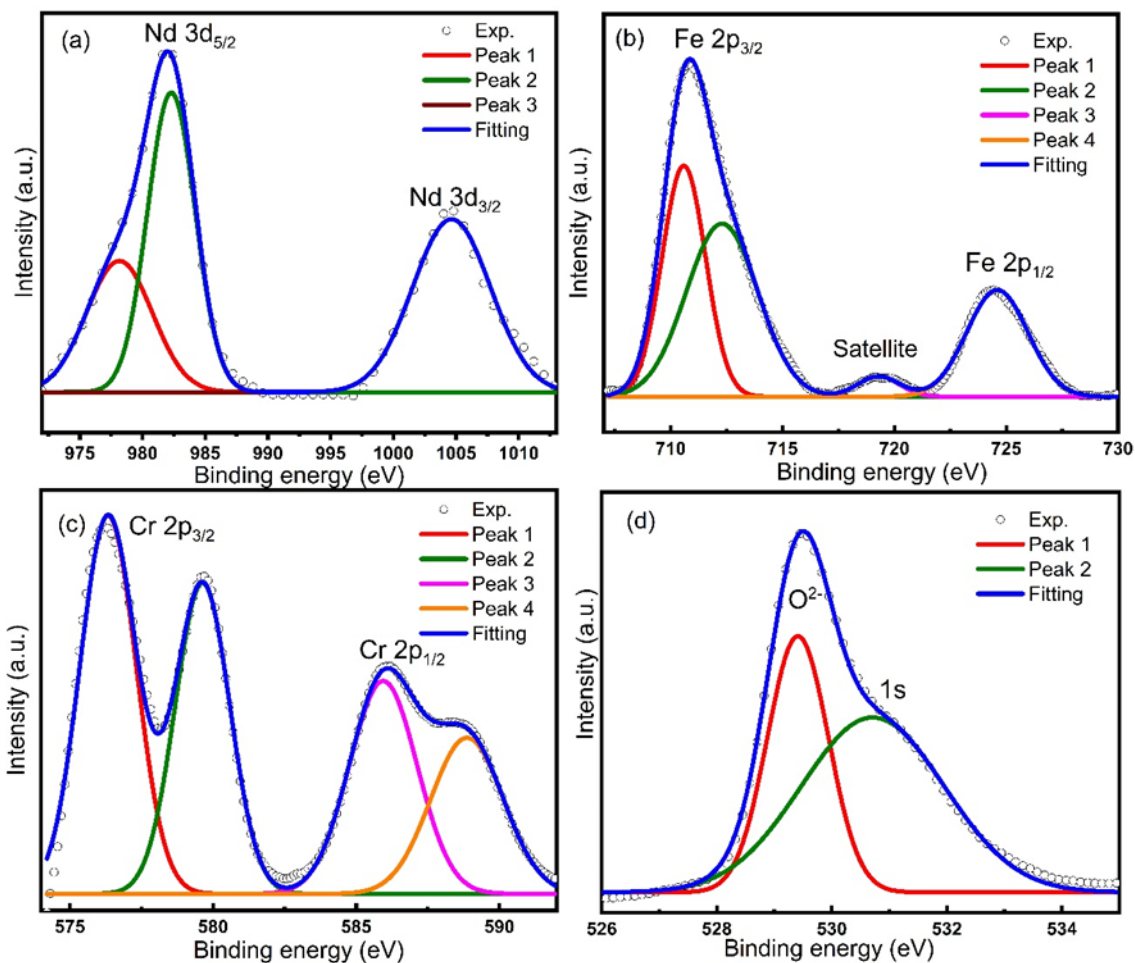
Fig. 5.8 (a–d) The core-level binding energy spectra of Nd (3d), Fe (2p), Cr (2p), and O (1s) of the Nd_2FeCrO_6 nanoparticle, respectively. The black circles indicate the experimental spectra, while the blue solid line is the sum of the fitted peaks. Peak 1, peak 2, peak 3, and peak 4 are sorted in ascending order of binding energy.

To determine the valence state of Nd, Fe, and Cr in NFCO double perovskite, bond valence sum (BVS) was calculated. BVS can be expressed as [153];

$$BVS = \sum \exp\left[\frac{R_0 - r_{ij}}{b}\right] \qquad \cdots\cdots\cdots \text{(5.4)}$$

where r_{ij}, R_0 and b represents the bond length between i and j atoms, the empirically determined distance for a given cation-anion pair, and the empirical constant, respectively. The valence states of the Nd, Fe and Cr were found to be around +3 which confirmed the XPS observations.

5.5 Magnetic properties
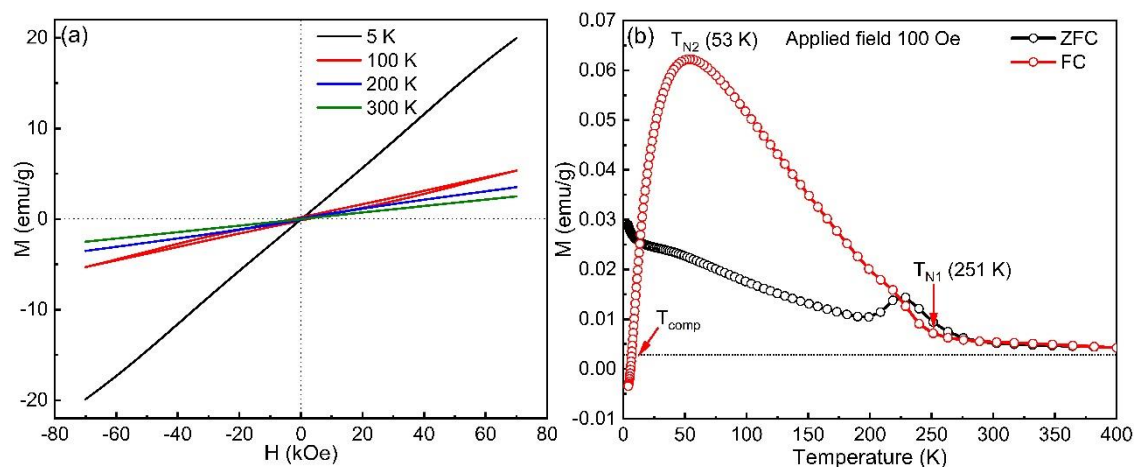
Fig. 5.9 (a) M-H hysteresis loops of Nd_2FeCrO_6 measured at 300 K, 200 K, 100 K and 5 K temperature. (b) ZFC and FC magnetization of Nd_2FeCrO_6 as a function of temperature measured in a magnetic field of 100 Oe.

The XRD analysis showed that Fe and Cr ions were not perfectly ordered at the B site of as-synthesized NFCO nanoparticles. Further, the mixed cationic states of Fe and Cr ions as revealed by the XPS measurement confirmed the presence of short-range ordering in NFCO. The aforementioned outcomes suggested that three distinct interactions should be considered in the NFCO double perovskite which are Fe^{2+}/Fe^{3+}-O-Fe^{2+}/Fe^{3+}, Cr^{2+}/Cr^{3+}-O-Cr^{2+}/Cr^{3+} and Fe^{3+}-O-Cr^{3+} interactions. According to Goodenough-Kanamori super-exchange rule, the Fe^{2+}/Fe^{3+}-O-Fe^{2+}/Fe^{3+}, Cr^{2+}/Cr^{3+}-O-Cr^{2+}/Cr^{3+} interactions will favor AFM ordering and Fe^{3+}-O-Cr^{3+} will favor FM interaction in the system [147, 154, 155].

Fig. 5.9(a) depicts the field-dependent magnetization (M-H) curve of NFCO double perovskite measured at different temperatures, where saturation was not observed even under very high external magnetic field of 70 kOe. Such unsaturated magnetic behaviour regardless of temperature variation suggests the AFM nature of NFCO. The calculated remanent magnetization (M_r) and coercive magnetic field (H_c) values are presented in Table 5.4. The presence of small M_r and H_c values indicate the existence of weak ferromagnetic (WFM) behaviour attributed to the Fe-O-Cr super-exchange interaction under a potent AFM background (influenced by the Fe-O-Fe/Cr-O-Cr super-exchange interactions) [114]. The coexistence of both FM and AFM states observed in M-H investigations inspired us to conduct additional studies to further elucidate this phenomenon.

Table 5.4 Remanent magnetization (M_r) and coercive magnetic field (H_c) values of Nd_2FeCrO_3 nanoparticles at various temperatures.

Temperature (K)	M_r (emu/g)	H_c (Oe)
5	0.034	15
100	0.1836	2563
200	0.08	1234
300	0.0029	68
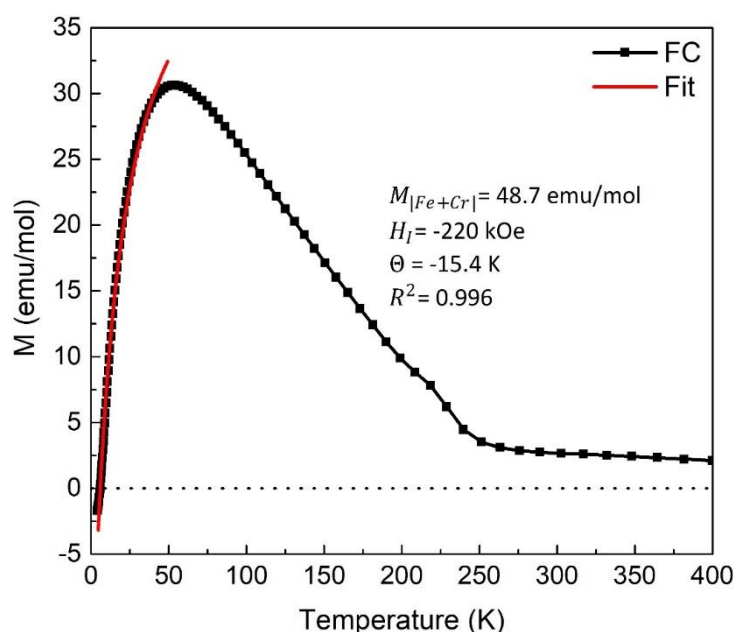
Fig. 5.10 Modified Curie−Weiss fit to the FC magnetization of the Nd_2FeCrO_6 double perovskite.

Therefore, the temperature-dependent magnetization (M-T) was measured under both zero field-cooled (ZFC) and field-cooled (FC) conditions over a wide temperature range of 4 to 400 K with an external field of 100 Oe. Fig. 5.9(b) shows ZFC and FC magnetization of NFCO, where two magnetic transitions occurred one at 251K (T_{N1}) and another one at 53K (T_{N2}) in FC curve. The 1st order magnetic transition peak at T_{N1} referred to spin-canted AFM ordering of Cr^{3+} ions [63]. Noticeably, above T_{N1}, the ZFC and FC curves merged with each other suggesting the absence of proper long-range ordering, which might have been induced by frustration effects [63]. The frustration effect might have been induced by the disordered Fe^{3+} and Cr^{3+} ions at B sites (B′ and B″) due to the random orientation of magnetic ions in the octahedral sublattice. As the

temperature was reduced below (T_{N1}), FC magnetization increased successively due to the WFM moment caused by spin canting of the dominantly disordered Fe^{3+} and Cr^{3+} ions, [21] and the FC curve showed second magnetic transition at cryogenic temperature 53 K due to the AFM ordering of Nd^{3+} ions [63]. When the temperature was further decreased, the FC curve crossed zero magnetization at the compensation temperature (T_{comp} = 6 K) below which magnetization reversal (MR) took place. The sign of magnetization in FC curve became negative due to the interaction between paramagnetic (PM) Nd^{3+} and canted AFM Fe^{3+}/Cr^{3+} magnetic moments. Such MR phenomena were also reported in several disordered materials where the B-site was occupied by unlike magnetic ions. The observed MR in NFCO double perovskite can be well explained if two sublattices, Nd and |Fe+Cr|, are considered.
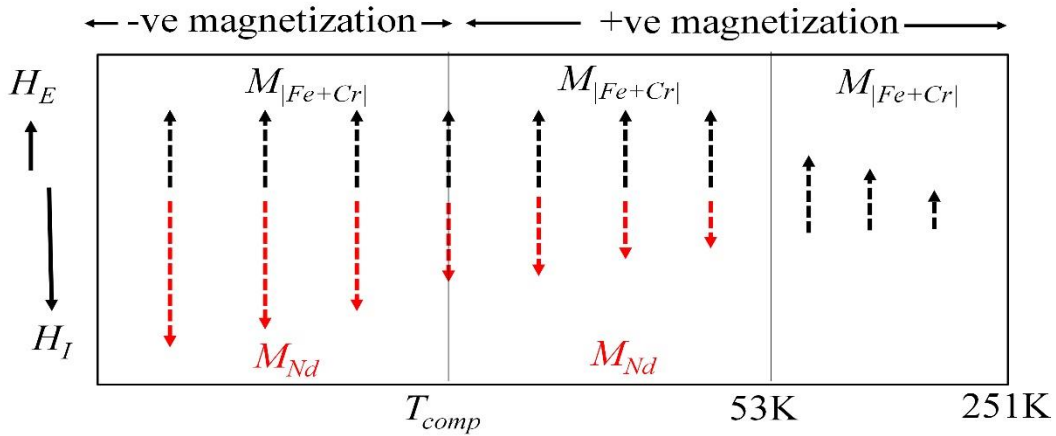
Fig. 5.11 Distribution of Nd and |Fe+Cr| moments (schematically).

The canted moments on Fe/Cr sites in FeO_6 and CrO_6 polyhedrons interacted via Dzyaloshinskii-Moriya (DM) interactions, resulting in a WFM component within the system. The competition between DM interactions of Fe-O-Fe and Cr-O-Cr with that of Fe-O-Cr resulted in sign reversal in magnetization [21]. The PM Nd^{3+} moments got polarized by the internal molecular field of |Fe+Cr| sublattice and tend to align themselves along anti-parallel to the WFM component of the |Fe+Cr|. At the temperature downturn, Nd^{3+} moments got more aligned and when the polarization of Nd sublattice neutralized the WFM contribution of |Fe+Cr| sublattice, magnetization became zero at the compensation point. At $T < T_{comp}$, the polarized Nd^{3+} moments suppressed this WFM contribution of |Fe+Cr| sublattice, and the sign of FC magnetization curve became

negative giving rise to diamagnetism. Such trend was also reported in $YbCrO_3$ [156], $La_{1-x}Pr_xCrO_3$ [157] and Fe doped $NdCrO_3$ [63].

The measured value of net magnetization in the FC mode was fitted by modified Curie-Weiss law and expressed as the combination of the magnetization of |Fe+Cr| and Nd sublattice [21].

$$M = M_{|Fe+Cr|} + \frac{C_R(H_I + H_E)}{T - \Theta} \qquad \cdots\cdots\cdots \quad (5.5)$$

Here, $M_{|Fe+Cr|}$, C_R, H_I, H_E and Θ are constant related to the FM moment of |Fe+Cr| sublattice, Curie constant of Nd^{3+} ion, internal field due to |Fe+Cr| sublattice ordering, applied magnetic field and Weiss constant, respectively.

Fig. 5.10 shows that FC magnetization data of NFCO can be reasonably fitted by the Modified Curie-Wiess law at low temperatures, with a goodness of fit (R^2) value close to 1. Above the temperature of 50 K the measured and fitted FC curves got bifurcated, indicating the appearance of an additional magnetic transition in the |Fe+Cr| sublattice. Moreover, the value of Θ was negative which signified that Nd^{3+} ions possess AFM nature [21]. In addition, $M_{|Fe+Cr|}$ and H_I had opposite signs, which means that the internal field of the |Fe+Cr| sublattice was opposite to the WFM moment of $M_{|Fe+Cr|}$. The arrangement of magnetic moments is represented schematically in Fig. 5.11. Notably, the existence of competing multi-domain interactions in NFCO as inferred from M-T investigations can be associated with the exchange bias (EB) effect which arose at the interface due to the exchange coupling between these multiple magnetic components. With a view to studying EB in NFCO, the FC isothermal M-H loops were measured while the sample was cooled down from 300 K to 10 K i.e., through Néel temperature and varying cooling magnetic fields (H_{cool}) were applied. A shift in the M-H loop along the positive field axis can be observed in Fig. 5.12(a), which demonstrates the existence of EB in NFCO.

Moreover, very small coercivity was observed due to the dominant AFM interaction of Fe-O-Fe/Cr-O-Cr in the sample. The cooling field-dependent exchange bias field plotted at 10 K has been presented in Fig. 5.12(b). The exchange bias field (H_{EB}) was quantified following this relation [21]

$$H_{EB} = |H_{C1} + H_{C2}|/2 \qquad \cdots\cdots\cdots \quad (5.6)$$

where H_{C1} and H_{C2} are the left and right coercive fields, respectively. Without a cooling field when the system was cooled down from 300 K to 10 K i.e., below the ordering temperature of Nd^{3+}, no EB was observed. However, the H_{EB} value rose abruptly with the

increase in applied cooling magnetic fields. As mentioned earlier, the interaction between the |Fe+Cr| and Nd sublattices favored AFM behaviour. When the sample was cooled down from high temperature and external field was applied, the FM component of |Fe+Cr| sublattice as well as the spins of the PM Nd^{3+} ions will align along the direction of the external field H_{cool}. However, when the external field was reversed at 10 K, the FM spins of the Fe/Cr ions started to rotate in a smaller field because of the AFM interaction with the PM Nd^{3+} spins, which might have exerted a torque along the same direction as the field, due to the positive EB effect [21].
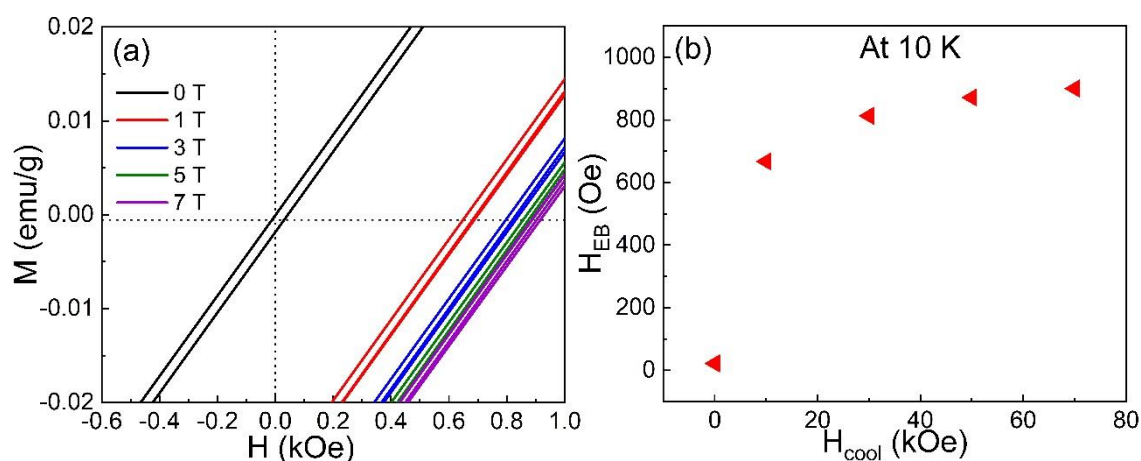
Fig. 5.12 (a) M-H hysteresis measured at different applied fields and (b) the variation of the exchange bias fields (H_{EB}) as a function of cooling field for Nd_2FeCrO_6 at 10 K.

The above observation was also interpreted by considering the competition between Zeeman energy of Nd^{3+} ions and exchange energy between |Fe+Cr| and Nd sublattices. The increase in H_{EB} with H_{cool}, indicated that the exchange energy was dominating the Zeeman energy [21]. This statement was also justified by the FC magnetization curve where magnetization reversal was observed when the exchange energy dominated the Zeeman energy of the |Fe+Cr| spins due to antiferromagnetic coupling between the two sublattices [20].

5.6 Ferroelectric properties

To study the ferroelectric behaviour of synthesized NFCO double perovskite, a ferroelectric loop tracer was used to capture ferroelectric hysteresis loops (P-E loops) at various fields. However, there were no detectable loops for the as-synthesized NFCO sample. The measurement began with a field of 0.5 kV; however, the system indicated an overloaded signal, and no hysteresis loop was observed. An electric field of up to 10 kV

field were employed, but the signal remained the same, indicating that NFCO double perovskite had no ferroelectric characteristics or features.

5.7 Optical properties and applications

The UV-visible absorbance spectrum demonstrated the optical properties of the synthesized NFCO nanoparticles. As can be observed in Fig. 5.13(a), absorption was maximum in the UV region and decreased as wavelength increased. Moreover, the absorbance spectrum had multi-band electronic configuration [62] where the absorption peaks near 306 and 391 nm resulted from charge transfer from O-2p to Fe/Cr-3d orbital [158] and the peak near 501 nm might have arisen due to the electronic transitions between p orbitals. The absorption peak near 750 nm can be associated with d to d electronic transition in Fe^{3+} ions [62].

The optical band gap of the synthesized NFCO double perovskite was calculated using the UV-visible absorption spectrum. Considering both direct and indirect transition, the band gap energy of NFCO double perovskite was calculated using the Tauc relation [159] i.e.,

$$\alpha h v = A(h v - E_g)^n \qquad \cdots\cdots\cdots \quad (5.7)$$

where, α, hv, A, E_g and n represent the absorption coefficient, incident photon energy, characteristic parameter independent of the photon energy, optical band gap, and the electronic transition type, respectively. For direct and indirect transitions, n were 0.5 and 2, respectively [160]. Figs. 5.13(b) and (c) showed the Tauc plots for determining the direct and indirect optical band gaps of NFCO nanoparticles. The band gaps were extracted by extrapolating the linear part of these curves with straight lines to the horizontal axis. As can be seen in Fig. 5.13(b) and (c), the band gap values were calculated to be 1.95 eV and 1.65 eV for direct and indirect transitions, respectively. Notably, as mentioned in the chapter 4, the direct band gap of NFCO double perovskite was determined as 1.85 eV by the theoretical calculations, which is quite comparable to the experimentally obtained value of 1.95 eV. Direct band gap of 1.95 eV along with high optical absorption at 501 nm implied that NFCO nanoparticles can efficiently absorb the major portion of the visible spectrum which can have promising potential in photoelectrochemical and photovoltaic device applications.
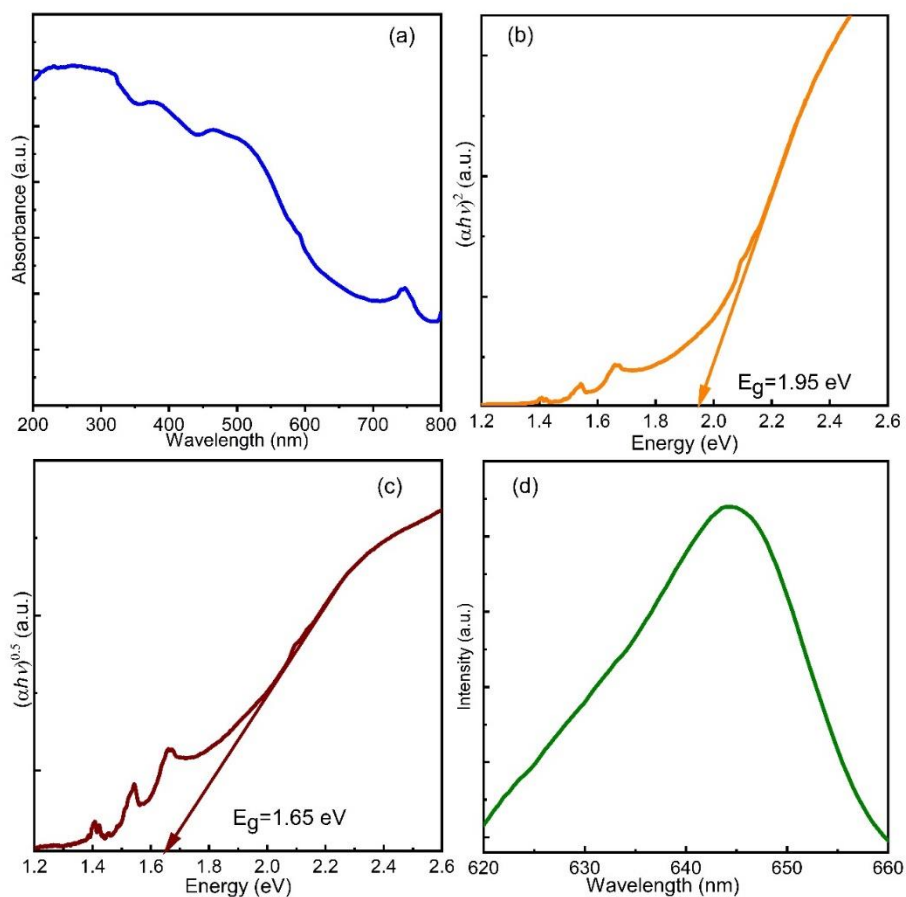
Fig. 5.13 Experimentally obtained (a) optical absorbance spectrum, Tauc plots for direct (b) and (c) indirect optical band gaps estimation and (d) steady-state photoluminescence spectrum of Nd_2FeCrO_6 nanoparticles at room temperature.

Further, the steady-state PL spectrum of as-synthesized NFCO nanoparticles was examined for an excitation wavelength of 230 nm to get insight into their charge-carrier recombination mechanism. A PL peak was detected at approximately 644 nm, indicating that the photogenerated electrons and holes recombined radiatively in NFCO double perovskite after excitation, as shown in Fig. 5.13(d). Notably, from the position of the PL peak, the band gap value of NFCO was found to be 1.93 eV which closely matched the direct band gap value as obtained from the Tauc plot (Fig. 5.13(b)). It is also noteworthy that compared to direct band gap materials, the radiative recombination is considerably less likely to occur over time in indirect band gap materials. This is because, in addition to photons, the absorption and emission of phonons are required for radiative recombination in indirect band gap materials. As a result, it is reasonable to assume that NFCO is a direct band-gap double perovskite with a band gap of 1.95 eV. This result

confirmed NFCO's semiconducting nature and, more significantly, its capacity to effectively absorb visible light from the solar spectrum.
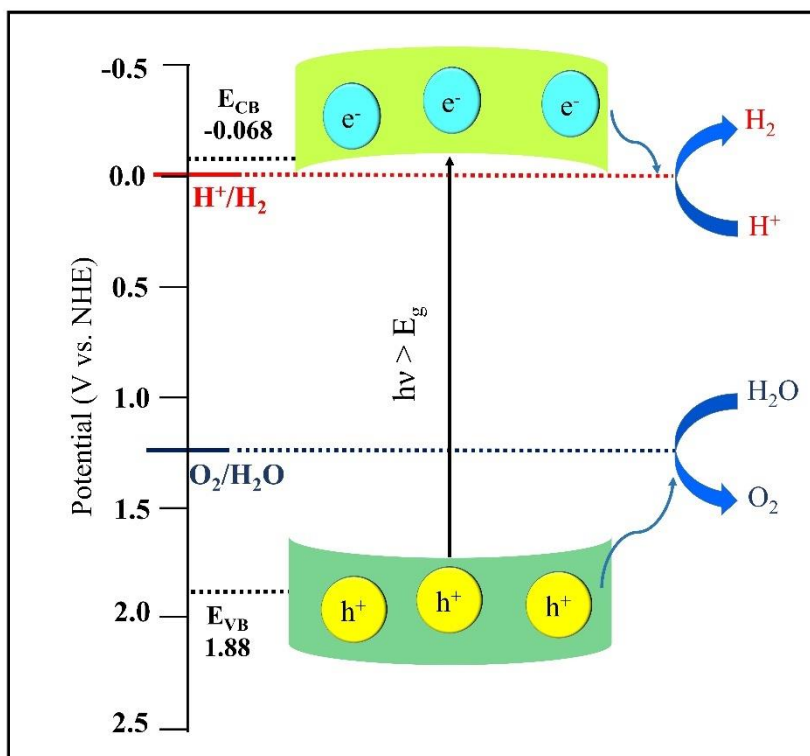
Fig. 5.14 Schematic diagram of the calculated valence and conduction band edge positions of Nd_2FeCrO_6 double perovskite oxide.

Furthermore, the band edge positions of as-synthesized NFCO double perovskite were calculated to assess their ability for various optical applications. The conduction band and valence band edge potentials of NFCO were calculated using the Mulliken electronegativity method [161, 162]. The conduction band edge (E_{CB}) and valence band edge (E_{VB}) potentials were calculated using the following equations.

$$E_{CB} = \chi - E_c - \frac{1}{2}E_g \qquad \text{········· (5.8)}$$

$$E_{VB} = E_{CB} + E_g \qquad \text{········· (5.9)}$$

where χ represents the absolute Mulliken electronegativity of NFCO perovskite, E_C is the free electron energy of hydrogen ($\sim$4.5 eV), and E_g represents the optical band gap. The Mulliken electronegativity of NFCO double perovskite was calculated to be 5.41 eV. By substituting the appropriate values of χ, E_C, and E_g, conduction band edge potential (vs NHE, normal hydrogen electrode potential) was found to be -0.068 eV, and the calculated

valence band edge potential (vs NHE) was 1.88 eV, assuming a direct band gap value of 1.95 eV as measured from the Tauc plot (Fig. 5.13(b)).

The approximate band edge positions of NFCO nanoparticles corresponding to the H^+/H_2 potential level (0 eV vs NHE, pH 0) and the O_2/H_2O potential level (1.23 eV vs NHE, pH 0) are shown in Fig. 5.14. Notably, if a semiconductor's conduction band edge potential is more negative than the H^+/H_2 potential, a photocatalytic H_2 evolution process is likely to occur. Similarly, if the valence band edge potential is greater than the potential of O_2/H_2O, O_2 gas will evolve. As shown in Fig. 5.14, the value of valence band potential was sufficiently positive compared to the oxidation potential of water, suggesting that NFCO nanoparticles are suitable for photocatalytic O_2 production [163]. In contrast, the E_{CB} of NFCO is more negative than the H^+/H_2 potential, indicating that NFCO nanoparticles could potentially be used for photocatalytic H_2 evolution [163]. However, to date, metal oxide semiconductors, which can show photocatalytic water splitting ability under visible light irradiation are quite rare. As a result, NFCO double perovskite is a good candidate for visible light-responsive photocatalysis because of its favourable surface morphology, suitable band gap of 1.95 eV, and the locations of its band edges.

CHAPTER 6

EXPERIMENTAL AND THEORETICAL INVESTIGATION OF Gd_2FeCrO_6

6.1 Experimental investigation of Gd_2FeCrO_6 perovskite

The structural, magnetic, and optical properties of Nd_2FeCrO_6 double perovskite were discussed in the previous two chapters. Theoretical predictions on Nd_2FeCrO_6 perovskite demonstrated that this structure can be synthesized at ambient pressure. Following the success of the Nd_2FeCrO_6 synthesis, a similar type of double perovskite Gd_2FeCrO_6 (GFCO) was synthesized using the same sol-gel technique. In this section, the crystallographic structure along with magnetic and optical properties of GFCO double perovskite were discussed.

6.1.1 Crystallographic structure analysis

Initially, the tolerance factor and global instability index (GII) of GFCO were calculated using the Structure Prediction Diagnostic Software (SPuDS) to get an idea about its crystal structure [138]. The tolerance factor (t) of double perovskite GFCO can be expressed as, [136, 140],

$$t = \frac{r_{Gd}+r_O}{\sqrt{2}(\frac{r_{Fe}+r_{Cr}}{2}+r_O)} \qquad \cdots\cdots\cdots \quad (6.1)$$

Here, r_{Gd}, r_{Fe}, r_{Cr} and r_O denoted the ionic radii of Gd, Fe, Cr cations and O anion, respectively. Generally, for double perovskites, the value of $t \approx 1$ corresponded to ideal cubic structure. If t was greater than 1, the crystal structure would be hexagonal and if $t < 0.97$, the structure was either orthorhombic or monoclinic [136]. Notably, the t of GFCO double perovskite was calculated to be 0.91 at room temperature (RT) from which its crystal structure can be predicted as either orthorhombic or monoclinic.

It should be noted that the degree of stability of a certain phase of perovskite could be estimated by calculating its global instability index (GII), which was the difference between the calculated bond valence sum (BVS) and the formal valence of cations and anions. GII is defined as the root mean square of bond discrepancy factor in the unit cell [164, 165]:

$$GII = \sqrt{\frac{\sum_{i=1}^{N}(d_i)^2}{N}} \qquad \cdots\cdots\cdots \quad (6.2)$$

where d_i denoted the bond discrepancy factor calculated from bond valence sum and N

denoted the number of ions. Typically, for unstrained structures, the GII values were smaller than 0.1 valence unit (v. u.) [165]. Especially, as reported by a survey of literature, stable double perovskite crystal structures were formed under ambient pressure with a GII value less than 0.02 v. u [39, 146]. Notably, the GII value of GFCO was found to be 0.013 v. u. which was conspicuously smaller than 0.02 v. u. As a consequence, even without employing high-pressure during the synthesis, unstrained single-phase crystal structure of GFCO was achieved.
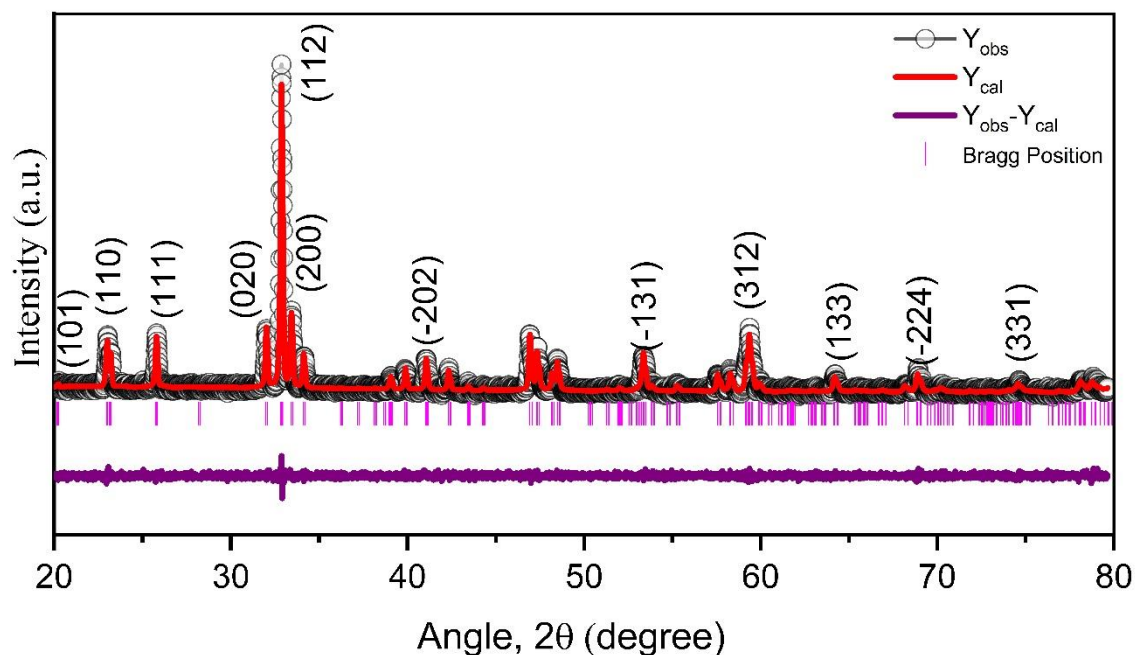
Fig. 6.1 Rietveld refined powder XRD spectrum of Gd_2FeCrO_6 nanoparticles at room temperature.

Fig. 6.1 demonstrated the Rietveld refined powder XRD spectrum of as-prepared GFCO nanoparticles at RT [141, 142]. Notably, no undesired secondary phase was detected in the XRD spectrum, which confirmed the high phase purity of the sample. Since the value of t was < 0.97, hence for Rietveld refinement, the monoclinic $P2_1/n$ space group was considered as the starting model. The lattice parameters, a, b and c of this monoclinic symmetry, were related to the cell parameter, $a_0 \approx 3.8$ Å, of ideal cubic perovskite, as $a \approx b \approx \sqrt{2}a_0$ and $c \approx 2a_0$. The background was modeled by linear interpolation between a set of background points with refinable heights. Bragg's reflections were modeled using Thompson-Cox-Hastings pseudo-Voigt Axial divergence asymmetry. Initially, cell parameters and scale factor were refined followed by the refinement of profile and full width at half maximum (FWHM) parameters. After achieving proper profile matching, the thermal and positional coordinates were refined. The crystal structure with orthorhombic *Pbnm* space group was also considered as the model for

refinement. However, between these two models, better fitting was obtained for monoclinic structure with *P2₁/n* space group. Notably, as Fe and Cr possess almost the same scattering factor, it was difficult to confirm by XRD technique whether GFCO was ordered or not. Yet one can obtain information about cation ordering by checking the superstructure reflection around 20° [148, 166]. As shown in Fig. 6.1, the superstructure reflection peak of GFCO at 20.2° was very weak (almost negligible), which suggested that the B-site cation ordering was not perfect in the synthesized sample. An indication of the absence of proper long-range ordering was also evident from the mixed valence states of Fe and Cr obtained by XPS analysis as will be discussed later on.
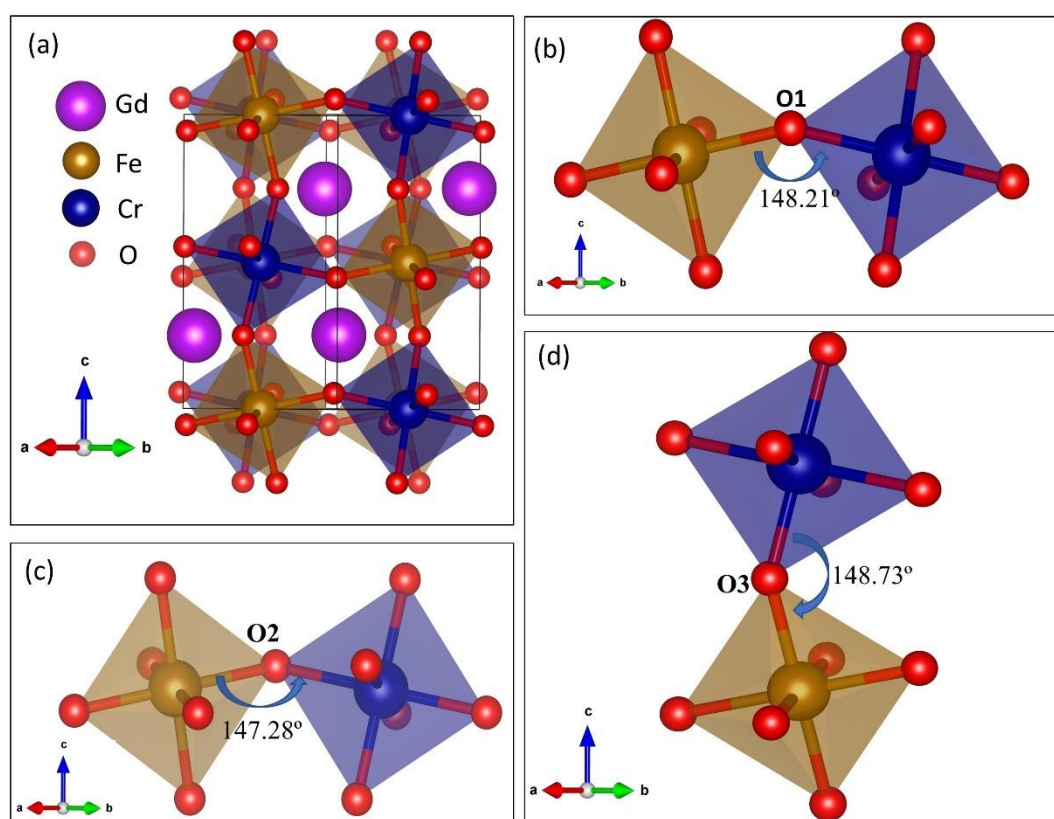
Fig. 6.2 (a) Schematic representation of the Gd_2FeCrO_6 monoclinic unit cell with magnified view of interconnected Fe/CrO_6 octahedra (b), (c) in the ab-plane and (d) along c-axis.

From the Rietveld refinement, the cell parameters of GFCO double perovskite were found to be $a = 5.259(1)$ Å, $b = 5.590(2)$ Å, $c = 7.675(3)$ Å, $\alpha = \gamma = 90°$ and $\beta = 89.958(1)°$ with cell volume 229.920 $Å^3$ which were in well agreement with those of analogous double perovskite materials [40, 56, 59]. Using these parameters, the unit cell of GFCO was modeled by the Visualization for Electronic and Structural Analysis

(VESTA) software [143]. The monoclinic unit cell of GFCO with corner shared Fe/CrO$_6$ octahedra was shown in Fig. 6.2(a). Fe and Cr cations were not exactly at the center of octahedra indicating octahedral distortion. For further insight, the enlarged view of the three interconnected Fe/CrO$_6$ octahedra was presented in the *ab* plane and along *c*-axis in Fig. 6.2(b, c and d). To estimate the distortion, the tilt angle (Φ) was also estimated, which was defined as $\Phi = (180 - \theta)/2$, where θ is the Fe/Cr-O-Fe/Cr bond angle [40]. The average value of Φ was found to be 15.96° which further confirmed the structural distortion of GFCO unit cell.

Table 6.1 Structural parameters and reliability (R) factors of Gd$_2$FeCrO$_6$ nanoparticles from Rietveld refinement of the XRD pattern.

Atom	Wyc. positions	x	y	z	Occ.	R factors
Gd	4e	0.5128	0.5599	0.2518	1	$R_p = 4.18$
Fe	2a	0	0.5	0	1	$R_{wp} = 3.93$
Cr	2c	0.5	0	0	1	$\chi^2 = 1.13$
O1	4e	0.2070	0.2071	-0.0547	1	
O2	4e	0.2988	0.6933	-0.0514	1	
O3	4e	0.4019	-0.0196	0.2495	1	

Table 6.2 Bond lengths, bond angles and tilt angles for Fe/Cr-O and Fe-O-Cr, respectively with BVS obtained via Rietveld refined XRD pattern.

Bond length (Å)		Bond angle (°)		Tilt angle (°)	BVS
Fe-O1	2.00				
Fe-O2	1.97				
Fe-O3	1.99	Fe-O1-Cr	148.21	15.89	Gd =2.85
Cr-O1	2.00	Fe-O2-Cr	147.28	16.36	Fe = 3.21
Cr-O2	2.02	Fe-O3-Cr	148.73	15.63	Cr = 2.77
Cr-O3	1.98				

Tables 6.1 and 6.2 summarized Rietveld refined other structural parameters i.e., Wyckoff positions, atomic coordinates, bond lengths, bond angles and BVS of synthesized GFCO nanoparticles obtained by Rietveld refinement as well as the reliability (R) factors. Notably, the bond distances and bond angles were shown in Table 6.2 agreed quite well with the reported values in the octahedral oxygen environment of related double perovskites [40, 59]. The valence states of the Gd, Fe and Cr were estimated by calculating their BVS [153] values which were found to be around +3 supporting the Fe^{+3} ($t_{2g}^3 e_g^2$) and Cr^{+3}($t_{2g}^3 e_g^0$) oxidation states in GFCO. Finally, the crystallite size of as-

prepared GFCO double perovskite was calculated to be 56 nm using Scherrer's equation [144, 145].

6.1.2 Raman spectrum analysis

Raman spectroscopy was performed at RT to further investigate the crystal structure, cation disorder and spin-phonon coupling of as-synthesized GFCO double perovskite (Fig. 6.3). Notably, the vibrational modes observed in the Raman spectrum arose from the Fe/CrO_6 octahedra and Gd-O bonds. Since the as-synthesized sample possessed monoclinic crystal structure with $P2_1/n$ space group, two main vibrational modes, A_g and B_g were expected in the range of 500 to 700 cm^{-1} in the Raman spectrum. The Raman spectrum of GFCO (Fig. 6.3) displayed two broad modes near 511 cm^{-1} and 690 cm^{-1} which corresponded to B_g and A_g modes, respectively and thus, confirmed the monoclinic $P2_1/n$ symmetry [33, 146, 165]. Here, A_g mode developed due to stretching (breathing) vibrations of Fe/CrO_6 octahedra [146] whereas B_g mode occurred due to both anti-stretching and bending motions. Noticeably, both the first-order strong modes i.e., A_g and B_g were fairly asymmetric. In these modes, the broadness and asymmetry might depend on several factors such as incomplete ordering of Fe and Cr sites, nearly same frequency of various Fe/Cr-O vibrations [33] etc.
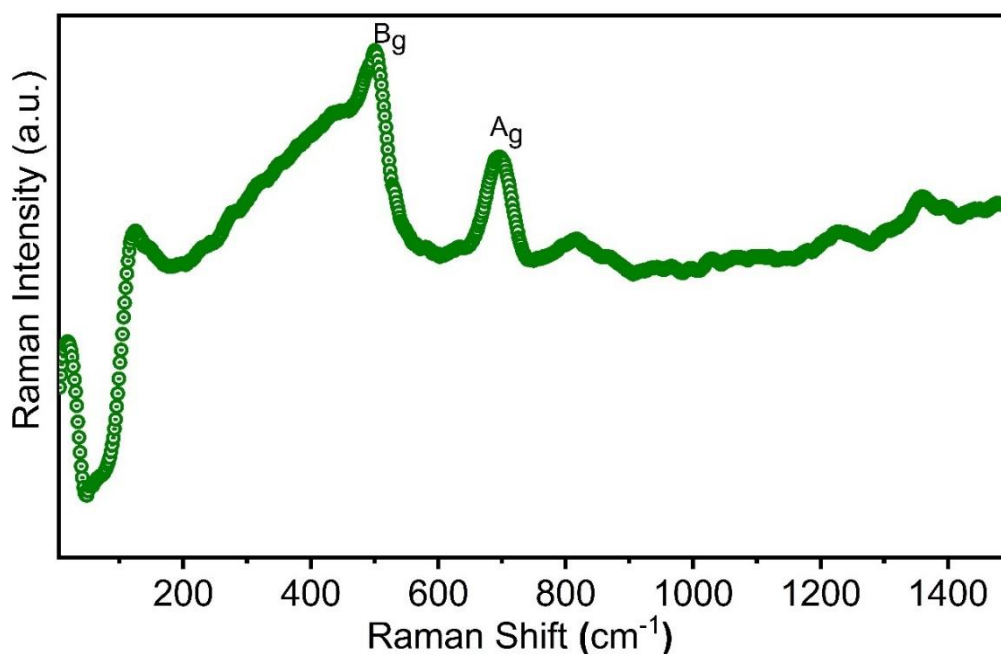
Fig. 6.3 Raman spectrum of Gd_2FeCrO_6 nanoparticles recorded at room temperature.

Furthermore, multiband was observed in Fig. 6.3 in the range of 800 to 1410 cm^{-1} which was associated with multi-phonon scattering. It was noteworthy that modes around 820 cm^{-1} and around 1355 cm^{-1} were the overtones of B_g and A_g, respectively. The mode at 1206 cm^{-1} was considered a combination of both B_g and A_g modes [148]. Such high frequency modes were also reported in double perovskite La_2NiMnO_6 thin film [148]. The presence of these high frequency modes in GFCO revealed its doubly ordered state. Due to the ordering of Fe/Cr cations, phonons were not limited to originate only from a point close to the Brillouin zone center. Rather they can emerge from any point within the Brillouin zone [148]. A stretching mode was also noticed in the low frequency regime (at around 150 cm^{-1}), which provided further evidence for the monoclinic $P2_1/n$ space group [33]. Such low-frequency vibrations were developed due to coupled Fe/CrO_6 tilting vibrations and Gd-O stretching. It was noteworthy that any intense mode around 377 cm^{-1} was the indication of oxide impurity. For as-synthesized GFCO, the most intense Raman mode was observed around 511 cm^{-1} which confirmed the phase purity of the synthesized double perovskite and supported the result of XRD analysis [167]. This intense mode was further used to calculate the Fe/Cr-O bond length by using the following equation [149]:

$$v(cm^{-1}) = 21349 \exp(-1.9176R(\text{Å})) \qquad \cdots\cdots\cdots \quad (6.3)$$

where v denoted the stretching Raman frequency and R is the Fe/Cr-O bond length. The calculated bond length of Fe/Cr-O is ~1.95 Å which was consistent with the average bond length of Fe-O and Cr-O (~1.99 Å) as obtained via Rietveld refinement.

6.1.3 FTIR spectrum analysis

FTIR analysis was performed at room temperature to investigate the chemical structure of synthesized GFCO nanoparticles as demonstrated in Fig. 6.4. Notably, the Fe/CrO_6 octahedra complex in the unit cell of GFCO was expected to have six normal modes of vibrations ($V_1 - V_6$). Among these six vibrations, V_1, V_2 and V_5 would be Raman active, V_3 and V_4 would be IR active and V_6 would be inactive in both [62, 150]. In the FTIR spectrum of GFCO (Fig. 6.4), the transmission mode at around 508 cm^{-1} was associated with V_3 which indicated the existence of bending vibrations of Fe/Cr-O bonds in the Fe/CrO_6 octahedra. The broad transmission band V_4 centered at 555 cm^{-1} corresponded to Fe/Cr-O stretching vibrations. The weak transmission band near 930 cm^{-1} was attributed to the NO_3^- ions which were trapped in the particles [150]. The weak bands observed at 1400–1600 cm^{-1} were caused by vibrations of C-O bonds generated by the chemisorption of ambient CO_2 by the GFCO surface [62]. Finally, the IR bands in the

range of 2840–3200 cm^{-1} might be imputed to the stretching vibrations of O-H bonds due to the adsorption of water at the surface.
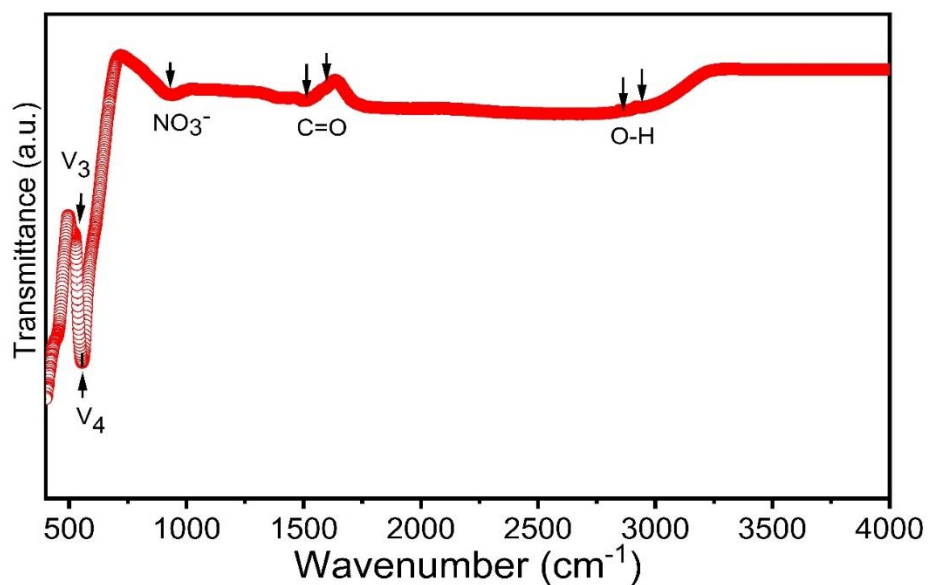
Fig. 6.4 FTIR spectrum of Gd$_2$FeCrO$_6$ nanoparticles recorded at room temperature.

6.1.4 Thermal stability and morphological analyses
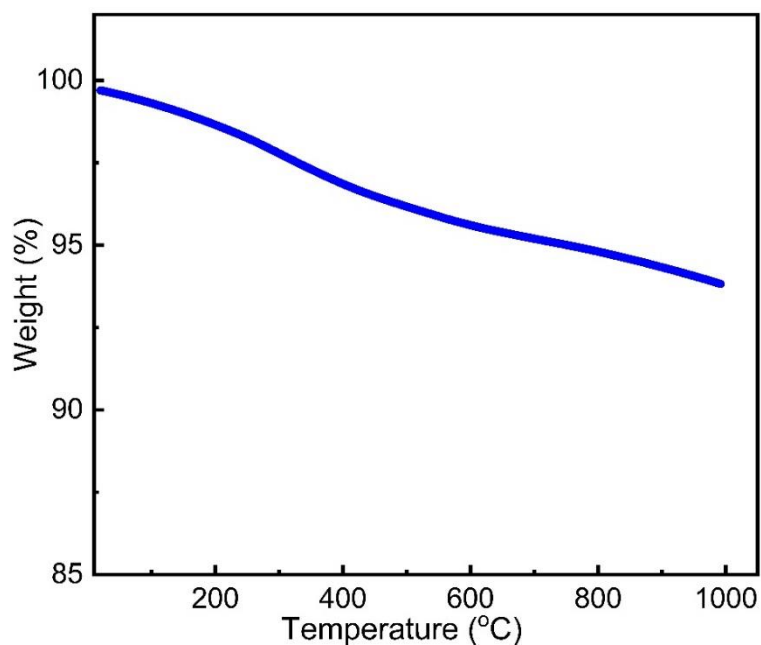
Fig. 6.5 TGA curve of Gd$_2$FeCrO$_6$ powders from 30 ℃ to 1000 ℃ in N$_2$ with heating rate of 10 ℃/min.

The thermal stability, an important property for perovskite materials for their future applications, was evaluated via TGA experiment of the as-prepared GFCO powder sample. The TGA curve shown in Fig. 6.5 demonstrated the great thermal stability of GFCO powders with a subsequent weight loss of only ~6% up to temperature 1000 °C which was comparable to that of some other double perovskites [168, 169]. The initial weight loss at a temperature below 150 °C might be due to the desorption of adsorbed water and gases. The weight loss at higher temperatures up to 1000 °C was gradual which was probably due to the reduction of both Fe and Cr ions associated with the loss of lattice oxygen. Notably, from 600 °C to 1000 °C, the weight loss is less than ~2%, indicating that the sample can be calcined within this temperature range. Therefore, considering the stability of the material over a wide range of temperature, it is worth noting that the annealing of the sample at 800°C was reasonable.
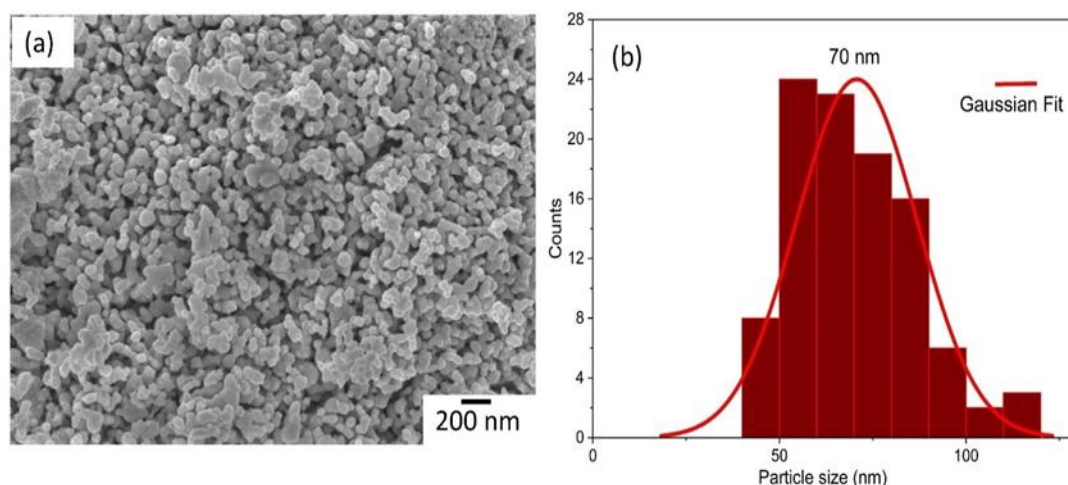
Fig. 6.6 (a) FESEM image of Gd_2FeCrO_6 nanoparticles with (b) particle size distribution histogram.

Table 6.3 Mass and atomic percentages of Gd_2FeCrO_6 nanoparticles as obtained by EDX analysis.

Element	Mass (%) (Theoretical)	Mass (%) (Experimental)	Atom (%) (Theoretical)	Atom (%) (Experimental)
Gd	60.67	59.18	20	20.85
Fe	10.77	13.74	10	13.63
Cr	10.03	11.79	10	12.56
O	18.52	15.29	60	52.96
Total	100	100	100	100

The FESEM image of GFCO double perovskite is presented in Fig. 6.6(a), which showed that as-synthesized nanoparticles are uniformly distributed and their surface is

satisfactorily homogeneous. Notably, in a previous investigation [62], a similar class of double perovskite Pr_2FeCrO_6 was synthesized using wet chemical technique co-precipitation. The authors observed an agglomeration in the synthesized nanoparticles due to the higher rate of precipitation [62]. However, in this present investigation by using sol-gel technique uniformly distributed non-agglomerated GFCO nanoparticles were successfully synthesized. Fig. 6.6(b) displayed the particle size distribution histogram as obtained from the FESEM image. From this figure, it can be estimated that the particle size of GFCO was mostly within the range of ~ 40 to 100 nm with ~ 70 nm average. The experimentally obtained percentages of mass and atom are provided in Table 6.3. In order to compare, the theoretically calculated percentages of mass and atom have also been tabulated. Clearly, the mass and atomic percentages of desired elements i.e., Gd, Fe, Cr and O in the as-prepared nanoparticles match quite well with the theoretical values which further justified the successful synthesis of GFCO double perovskite.

Fig. 6.7(a) showed a bright field TEM image of GFCO double perovskite. The particle size was in the range of 60–100 nm which was pretty consistent with the values obtained from FESEM imaging. Moreover, some of the particles had a diameter of 30–40 nm, as seen in the inset of Fig. 6.7(a). The high-resolution TEM (HRTEM) image shown in Fig. 6.8(b) represented the crystal lattice fringes of nanostructured GFCO with an inter-planar spacing of 0.28 nm corresponding to its (1 2 1) plane. The inset of Fig. 6.7(b) provided the selected area electron diffraction pattern of GFCO nanocrystal.
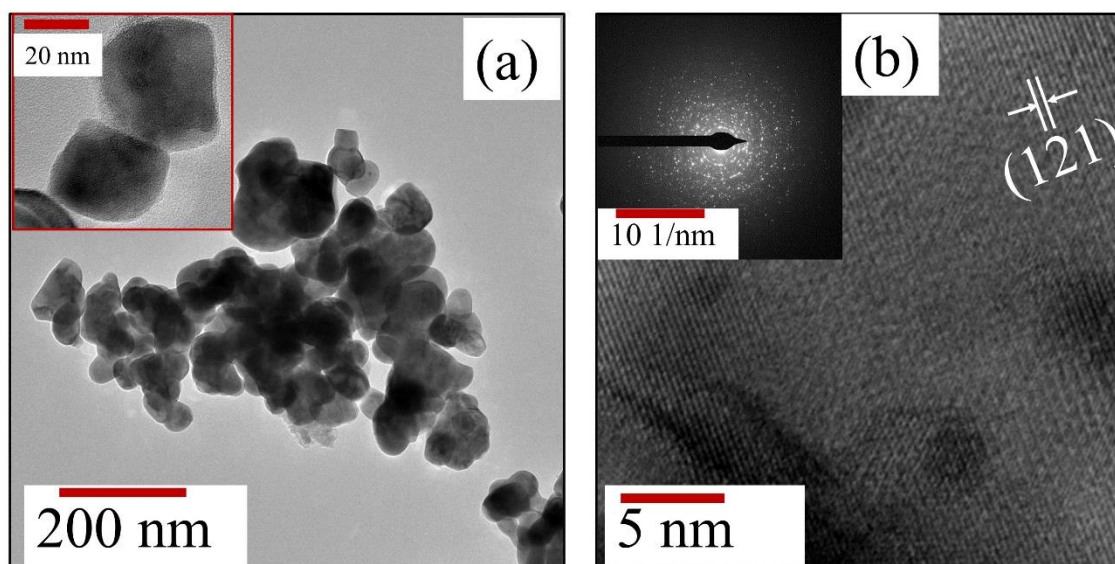
Fig. 6.7 (a) Bright field TEM image of synthesized Gd_2FeCrO_6 double perovskite. Inset of (a) shows individual nanoparticles. (b) HRTEM image of nanostructured Gd_2FeCrO_6 showing crystal planes. Inset shows SAED pattern of Gd_2FeCrO_6 nanocrystal.

6.1.5 XPS analysis

The chemical binding energies and oxidation states of different elements of as synthesized GFCO perovskite were scrutinized using XPS. The high resolution XPS spectra of Gd 4d, Fe 2p, Cr 2p and O 1s core levels for the as-synthesized sample were displayed in Fig. 6.8(a–d), respectively. The core level XPS spectrum of Gd (Fig. 6.8(a)) can be identified by two characteristic doublet peaks at $4d_{5/2}$ and $4d_{3/2}$ corresponding to the binding energy of 141.4 eV and 146.3 eV, respectively [170]. In the XPS spectrum of Fe contents (Fig. 6.8(b)), the observed two main peaks at 710 eV and 724.08 eV might have arisen due to the spin-orbit splitting of Fe 2p orbital. These two peaks were assigned to the corresponding states of Fe $2p_{3/2}$ and Fe $2p_{1/2}$, respectively and they indicated the Fe^{3+} oxidation state of Fe 2p [40]. Apart from these two peaks, a distinguishable satellite peak was observed at 718.60 eV. In the case of Fe 2p spectra, two adjacent peaks were observed at 710 eV and 711.20 eV which confirmed the presence of Fe^{2+} and Fe^{3+} oxidation states, respectively [64]. The Cr 2p spectrum shown in Fig. 6.8(c) revealed spin
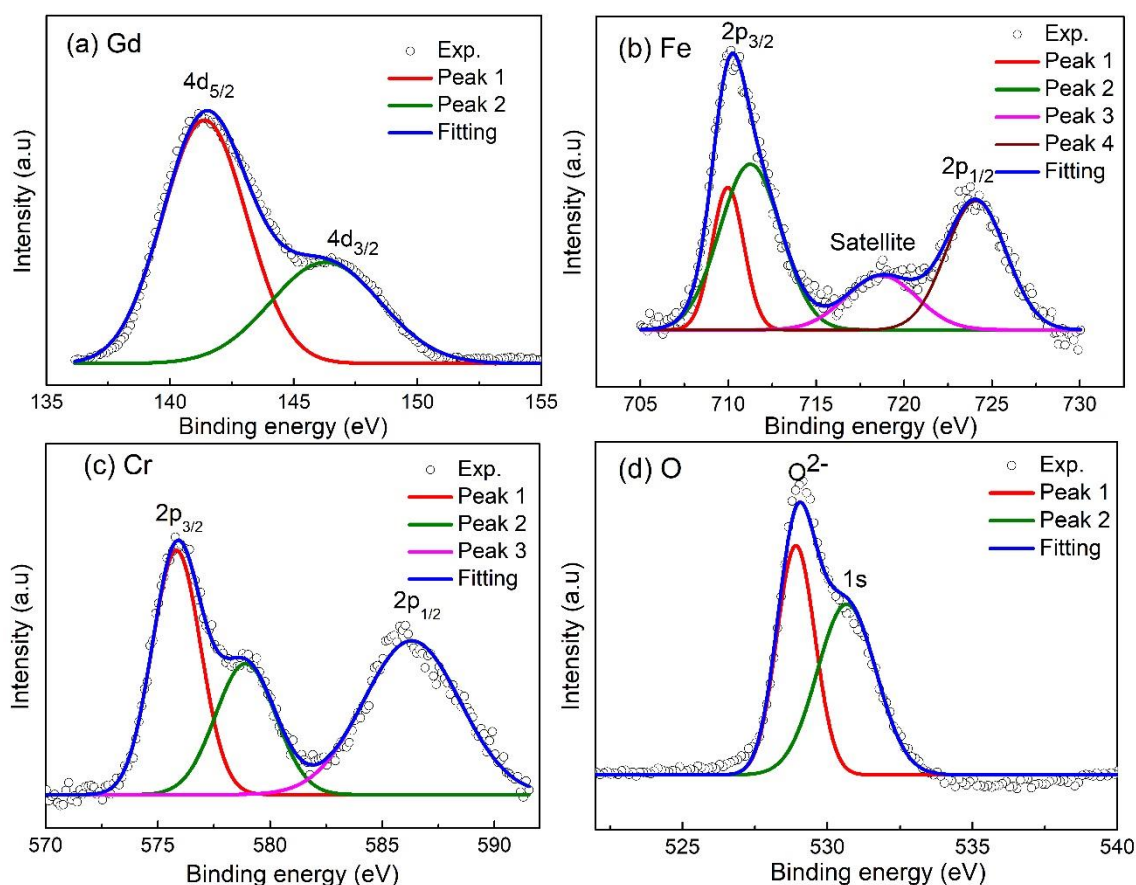
Fig. 6.8 (a-d) High-resolution XPS core spectra of Gd 4d, Fe 2p, Cr 2p and O 1s of Gd_2FeCrO_6 nanoparticles, respectively. The black circles are indicating the experimental (Exp.) spectra, while the blue solid line is the sum of the fitted peaks. Peak 1, peak 2, peak 3 and peak 4 are sorted by ascending order of binding energy.

orbit split $2p_{3/2}$ and $2p_{1/2}$ lines which appeared at 575.85 eV and 586.33 eV, respectively. The separation between these two doublets was 10.48 eV which corresponded to the +3 oxidation states of Cr [40]. The initial peak in the binding energy curve of the XPS spectrum of Cr shown in Fig. 6.8(c) was deconvoluted into two maxima around 575.85 and 578.92 eV which corresponded to the valence states of Cr^{2+} and Cr^{3+}, respectively [64]. The deconvoluted core-level spectrum (Fig. 6.8(d)) of oxygen (O^{2-}) 1s demonstrated two sets of peaks at 528.90 eV due to the singly ionized oxygen atoms and 530.69 eV for the interaction of oxygen atoms within the lattice, respectively.

6.1.6 Magnetic characterization

Fig. 6.9(a) displayed temperature dependent magnetization (M-T) curves of synthesized GFCO nanoparticles measured via ZFC and FC methods at 5–400 K under 100 Oe external magnetic field [171]. As can be seen, the FC magnetization curve increased with decreasing temperature without a sharp transition, indicating that there was no proper long-range order among Fe^{3+} and Cr^{3+} ions, as evidenced by XRD examination. Noticeably, the ZFC and FC curves demonstrated a divergence below 50 K which gradually enlarged at lower temperature below 20 K. Moreover, the ZFC curve exhibited a cusp-like feature at T ~15 K (marked by the blue arrow in Fig. 6.9(a)) suggesting a Néel transition [172]. Notably, as like as GFCO, a number of analogous double perovskites [172–175] demonstrated Néel transition at around 15 K.
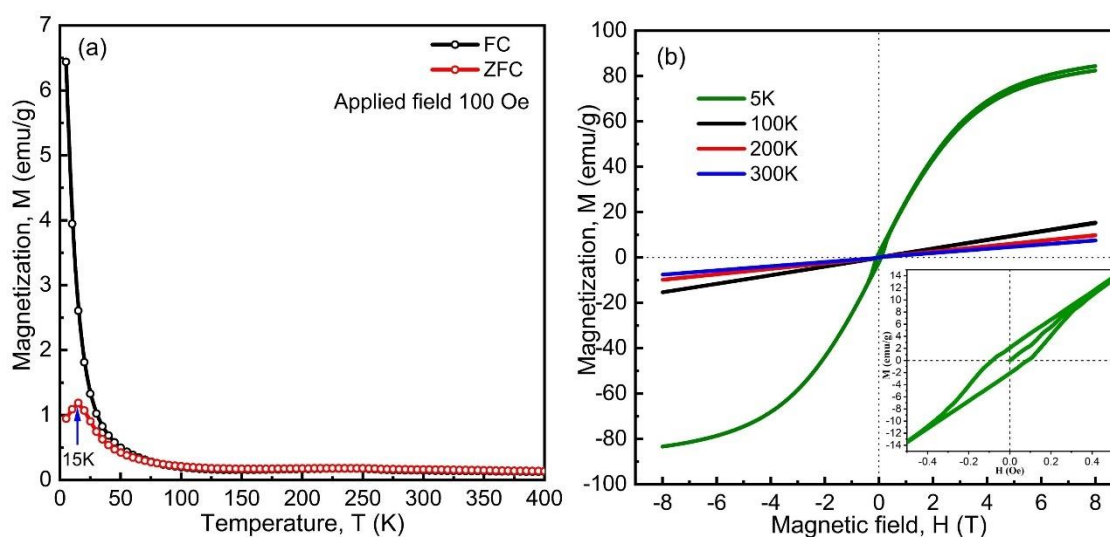
Fig. 6.9 (a) ZFC and FC magnetization vs. temperature measured under 100 Oe applied magnetic field. (b) M-H hysteresis loops recorded at 300 K, 200 K, 100 K and 5 K under an applied magnetic field of up to ± 8 T. The inset of (b) demonstrates an enlarged view of the hysteresis loop at 5 K.

Further, field dependent magnetization measurements of synthesized GFCO double perovskite were performed at 300 K, 200 K, 100 K and 5 K under an external magnetic field of up to ± 8 T. Fig. 6.9(b) presented the measured magnetization vs magnetic field (M-H) curves. As can be observed from Fig. 6.9(b), the M-H curves acquired at 300 K, 200 K and 100 K were linear and not saturated. At these temperatures, no hysteresis loop could be detected indicating the paramagnetic nature of as-prepared GFCO nanoparticles. Inset of Fig. 6.9(b) provided a magnified view of the magnetic hysteresis loop obtained at 5 K. This hysteresis loop was nearly saturated with a maximum magnetization of ~ 84 emu/g at an applied magnetic field of 8 T (Fig. 6.9(b)) which indicated the presence of FM state in GFCO nanoparticles at this lowest temperature. From this hysteresis loop, the values of remanent magnetization (M_r) and coercive field (H_c) of GFCO were estimated to be ~ 3.6 emu/g and ~ 821 Oe, respectively. Notably, at 5 K this narrow hysteresis loop was not completely saturated even upon the application of a magnetic field of 8 T (80 kOe) which indicated the presence of AFM states in GFCO nanoparticles along with FM domains [114]. These multiple magnetic domain states were a signature of complex magnetic behavior of GFCO double perovskite at low temperature which was visualized as follows. According to structural analyses, the Fe^{3+} and Cr^{3+} ions in GFCO double perovskite were not perfectly ordered at B sites (B and B'). Moreover, the XPS analysis evinced the presence of mixed valence states of Fe and Cr in GFCO double perovskite. Therefore, in the absence of long-range ordering among Fe^{3+} and Cr^{3+} sites, three next nearest neighbor configurations of B-B ions i.e., Fe^{2+}- Fe^{3+}, Cr^{2+}- Cr^{3+} and Fe^{3+}- Cr^{3+} may exist in GFCO. Among them, the Fe^{2+}- Fe^{3+} and Cr^{2+}- Cr^{3+} pairs will interact via the intervening O^{2-} ions which will give rise to anti-parallel alignment of magnetic spins and eventually generate non-zero spin moment resulting in AFM behavior [40]. Further, the magnetic interaction between Fe^{3+}-Cr^{3+} ions can be explained by the Goodenough-Kanamori rule [154]. According to this rule, the 180° superexchange interaction between the half-filled Fe^{3+}-d ($t_{2g}^3 e_g^2$) orbital and empty Cr^{3+}-d ($t_{2g}^3 e_g^0$) orbital through O^{2-} anion resulted in FM state. However, the nature of this magnetic interaction transforms into AFM when the $d(e_g^2) - O - d(e_g^0)$ angle got smaller than 180° due to lattice distortion [176]. Especially, for d^5-d^3 systems like GFCO, the superexchange interaction varied from FM to AFM for a range of 125° to 150° bond angle [176]. As demonstrated before, the Fe^{3+}-O^{2-}-Cr^{3+} bond in GFCO double perovskite bends to ~148° due to octahedral

distortion which can also be imputed to the emergence of the competing AFM interaction along with the FM state.

Furthermore, the M-H hysteresis loop at 5 K (inset of Fig. 6.9(b)) demonstrated an asymmetric shift although nominal along the field axis indicating the presence of intrinsic exchange bias effect in this double perovskite [177]. This was another indication of the concurrence of FM and AFM ordering in as-synthesized GFCO double perovskite [114], [177]. From the loop asymmetry, the exchange bias field was determined as ~ 15 Oe. However, further investigation needs to be performed in ZFC condition to confirm the presence of exchange bias effect in this double perovskite.

6.1.7 Ferroelectric properties

A ferroelectric loop tracer was used to capture ferroelectric hysteresis loops (P-E loops) at various fields to explore the ferroelectric behavior of synthesized GFCO double perovskite. Like NFCO double perovskite, the as-synthesized GFCO sample had no identifiable loops. The measurement started with a 1.0 kV field; however, the system reported an overloaded signal and no hysteresis loop. The signal stayed the same even when an electric field of up to 10 kV was applied, demonstrating that GFCO double perovskite had no ferroelectric characteristics or features.

6.1.8 Optical characterizations and applications

The optical characteristics of as-synthesized GFCO nanoparticles were extensively investigated by obtaining their UV–visible absorbance spectrum. As can be seen in Fig. 6.10(a), the experimentally obtained absorbance spectrum demonstrated four absorption bands (marked as A_1, A_2, A_3 and A_4) both in the UV and visible range indicating the multiband electronic structure of synthesized GFCO nanoparticles [62]. The high-energy absorption bands around 333 nm (A_1) and 412 nm (A_2) can be attributed to the p-d charge transfer transition $[O(2p) \rightarrow Fe/Cr(3d)]$ in Fe/CrO_6 octahedral centers of GFCO [158]. The absorption band, A_3 around 620 nm was associated with the p-p electronic transitions and the weak absorption band, A_4 around 772 nm might be imputed to the d-d transition in Fe^{3+} [62]. Thereafter, the absorbance data was employed to calculate the optical band gap of synthesized GFCO double perovskite. Notably, the optical band gap of GFCO was determined considering both direct and indirect transition using Tauc relation [159] as the following

$$\alpha h v = A(h v - E_g)^n \qquad\qquad \cdots\cdots\cdots \quad (6.4)$$

where α is the absorption coefficient, $h\nu$, A, E_g and n signify the energy of photons, proportionality constant, optical band gap and the electronic transition type, respectively. The value of n would be 0.5 for direct transition and 2 for indirect one [160]. Figs. 6.10(b) and (c) demonstrated the generated Tauc plots for estimating the direct and indirect optical band gaps of GFCO nanoparticles, respectively. The values of optical band gaps were calculated using the abscissa intercepts of the tangents to the linear region of the plots in these images. For direct and indirect transitions, the band gap values were determined to be 2.0 and 1.5 eV, respectively.
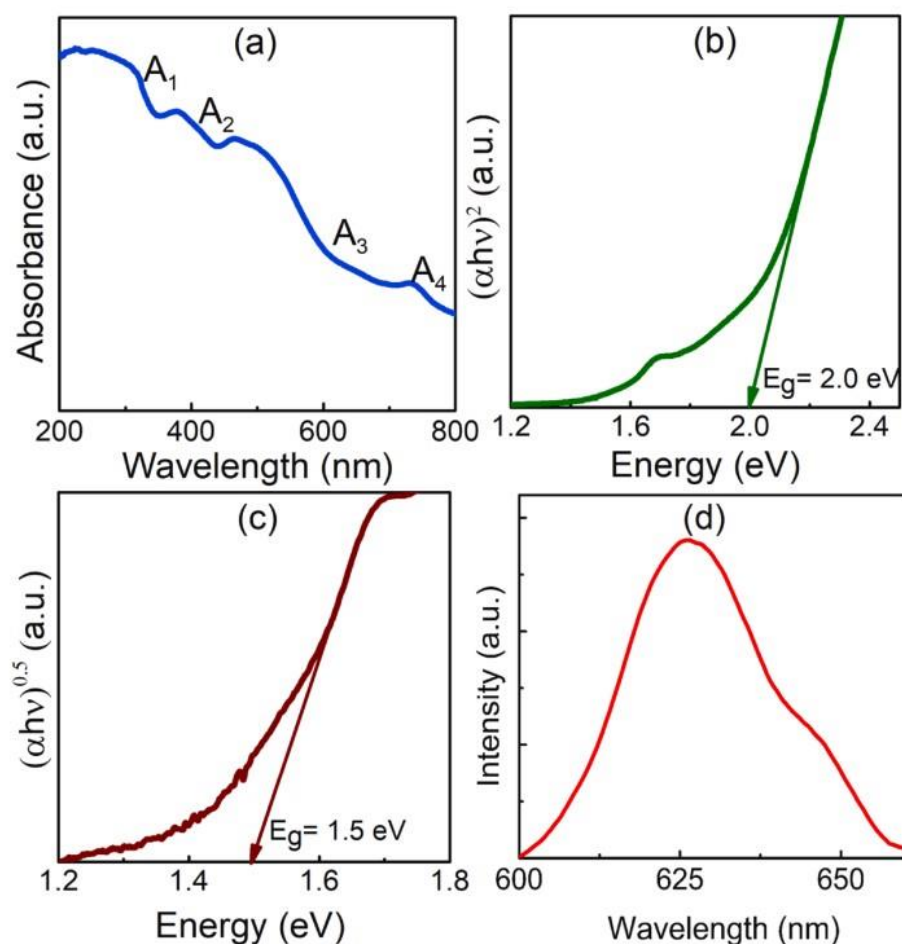
Fig. 6.10 Experimentally obtained (a) optical absorbance spectrum, Tauc plots for direct (b) and (c) indirect optical band gaps estimation and (d) steady-state photoluminescence spectrum of Gd_2FeCrO_6 nanoparticles at room temperature.

Further, the steady-state PL spectrum of as-synthesized GFCO nanoparticles at room temperature was obtained for an excitation wavelength of 230 nm to get insight into their charge-carrier recombination process. As shown in Fig. 6.10(d), a PL peak was observed at around 626 nm suggesting that upon excitation, the photogenerated electrons and holes recombine radiatively in GFCO double perovskite. Notably, from the position of the PL

peak, the band gap value of GFCO was found to be 1.98 eV which closely matched with the direct band gap value as obtained from the Tauc plot (Fig. 6.10(b)). Moreover, it was worth noting that in a given span of time, radiative recombination was much less likely to occur in indirect band gap materials as compared with the direct ones. This was due to the fact that along with photon, the radiative recombination in indirect band gap materials also required the involvement of the absorption and emission of phonon. Therefore, it was plausible to infer that our as-synthesized nanostructured GFCO was a direct band-gap double perovskite with a band gap value of ~ 2.0 eV. Notably, this outcome indicated the semiconducting nature of GFCO and, more crucially, reveals its ability to absorb the visible light of the solar spectrum efficiently.
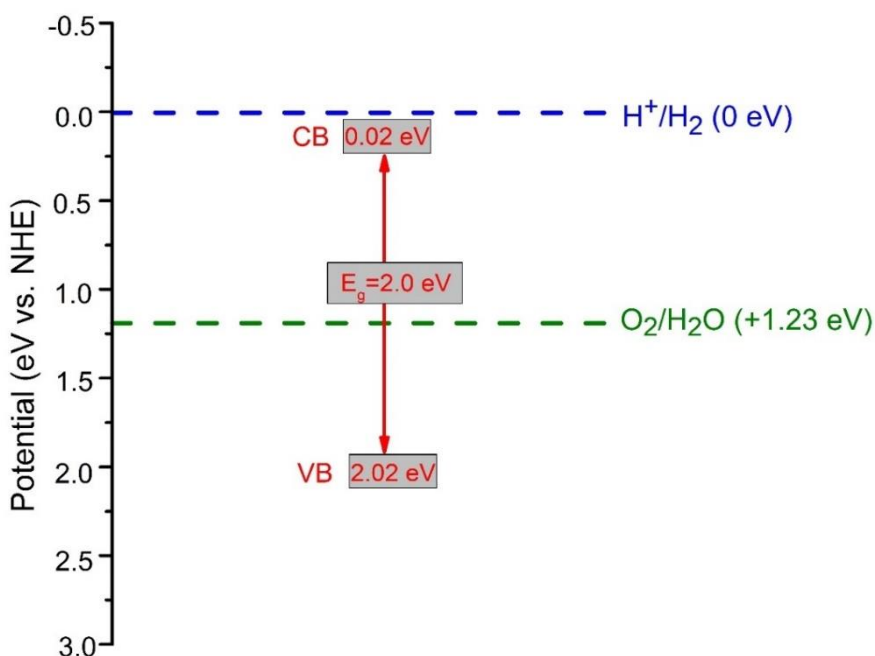
Fig. 6.11 Schematic diagram of the estimated band positions of Gd_2FeCrO_6 nanoparticles.

Moreover, the band edge positions of as-synthesized GFCO nanoparticles were determined to evaluate their potential for different optical applications. Mulliken electronegativity approach [161, 162] was adopted to calculate the conduction band minimum (CBM) and valence band maximum (VBM) potentials of GFCO. According to this approach-

$$E_{CBM} = \chi - E_C - \frac{1}{2}E_g \qquad \cdots\cdots\cdots \ (6.5)$$

$$E_{VBM} = E_{CB} + E_g \qquad \cdots\cdots\cdots \quad (6.6)$$

where χ is the Mulliken electronegativity of GFCO which was calculated to be 5.52 eV based on the electron affinities and atomic ionization energies. E_C is the energy of free electrons on the hydrogen scale ($\sim$ 4.5 eV) and E_g is the direct optical band gap (2.0 eV) as obtained from the Tauc plot (Fig. 6.10(b)). Notably, the CBM and VBM potentials (vs. normal hydrogen electrode potential, NHE) of GFCO were calculated to be 0.02 and 2.02 eV, respectively. In order to clearly elucidate the band diagram of GFCO in Fig. 6.11, the estimated band edge positions of GFCO were illustrated with respect to the H^+/H_2 potential level (0 eV vs NHE, pH 0) and the O_2/H_2O potential level (1.23 eV vs NHE, pH 0). Theoretically, if the CBM of a semiconductor was more negative than that of H^+/H_2 potential, photocatalytic H_2 evolution reaction was likely to occur. Similarly, if the VBM was more positive than O_2/H_2O potential, O_2 gas will evolve. As shown in Fig. 6.11, the VBM potential of GFCO was sufficiently positive with respect to the oxidation potential of water which unveiled the promising potential of GFCO nanoparticles to be employed in photocatalytic O_2 evolution [163]. Notably, it was challenging to find metal oxide semiconductors that can enable photocatalytic decomposition of water under visible light illumination. Hence, the favorable surface morphology, optimal direct band gap of 2.0 eV and the band edge positions of GFCO double perovskite make it a promising candidate for visible light responsive photocatalysis, especially for oxygen evolution from water.

6.2 Theoretical investigation of Gd₂FeCrO₆ double perovskite

In this section, the structural, optical and electronic band structure of GFCO double perovskite were investigated via density functional theory with GGA approach. Experimentally obtained structural parameters of GFCO from the previous section were utilized in this calculation. The effect of on-site Coulomb interaction on the structural, optical and electronic properties of GFCO double perovskite has also been investigated.

6.2.1 Computational details

In order to systematically analyze the structural, optical and electronic properties of our synthesized GFCO nanoparticles, DFT based first-principles calculations were performed using both GGA and GGA+U methods within the plane-wave pseudopotential (PWPP) framework as implemented in the Cambridge Serial Total Energy Package (CASTEP) [178]. The crystallographic structural parameters obtained from the Rietveld refined powder XRD spectrum of GFCO were employed for DFT calculation. Prior to calculation, the geometry was optimized via Brodyden-Fletcher-Goldfarb-Shanno (BFGS) scheme applying energy of 10^{-5}eV/atom, maximum force of 0.05 eV/Å and maximum stress of 0.1GPa [179]. The Gd $4f^8 5s^2 5p^6 6s^2$, Fe $3d^6 4s^2$, Cr $3s^2 3p^6 3d^5 4s^1$ and O $2s^2 2p^4$ electrons were treated as valence electrons. The plane-wave cutoff energy convergence result for structural optimization was demonstrated in Fig. 6.12 where the dashed line represents the default energy cutoff. Cutoff of energy of 450 eV was found sufficient to obtain the converged ground-state energy of GFCO. Hence, the plane-wave basis set was employed with the optimized energy cutoff of 450 eV. Moreover, Brillouin-zone integrations were carried out with a 5×5×3 Monkhorst-Pack k-point mesh [86]. Spin polarized mode during self-consistent field (SCF) calculations was endorsed and a SCF tolerance of $2×10^6$ eV per atoms was used.

Notably, to describe the exchange-correlation energy, at first, the GGA method based on the Perdew-Burke-Ernzerhof functional (PBE) within ultrasoft pseudopotentials (USP) was used. A spin-polarized calculation was carried out to confirm the exact ground state of GFCO double perovskite [180]. Further, the GGA+U calculation was performed with different values of U_{eff} for investigating the effect of Hubbard parameter U_{eff} on the structural, optical and electronic properties of the GFCO ground state. To be specific, U_{eff}

was varied from 1 to 6 eV for the Fe 3d and Cr 3d orbitals whereas for the Gd 4f orbital, U_{eff} was kept fixed at 6 eV in accordance with previous investigations [181].
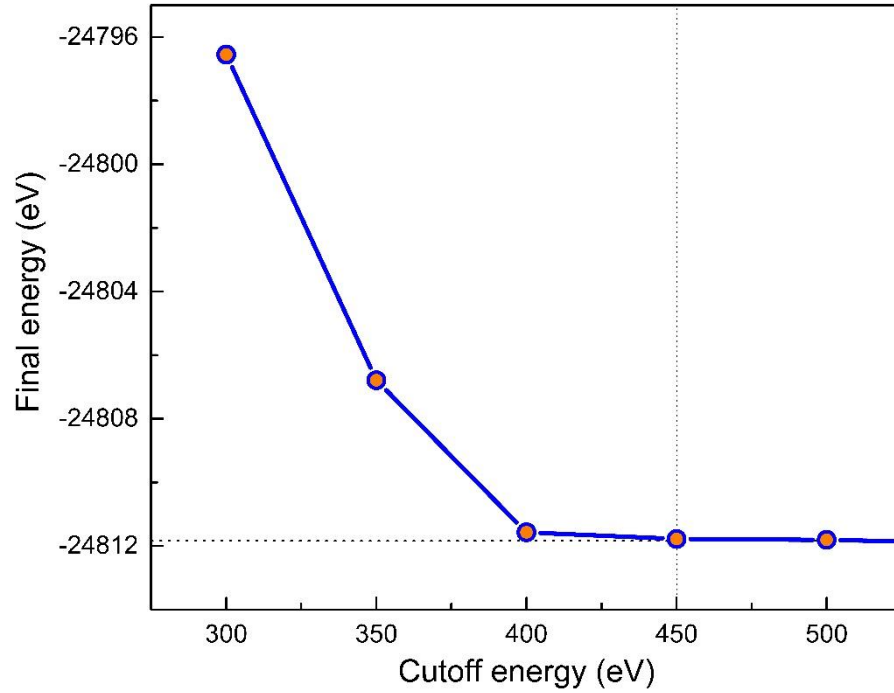
Fig. 6.12 Plane-wave cutoff energy convergence for structural optimization.

The optical absorption coefficient was obtained by the equation

$$\alpha = \sqrt{2\mu_o\omega}\sqrt{\sqrt{\epsilon_1^2(\omega) + \epsilon_2^2(\omega)} + \epsilon_1(\omega)} \quad \cdots\cdots\cdots \quad (6.7)$$

where $\epsilon_1(\omega)$ and $\epsilon_2(\omega)$ are frequency dependent real and imaginary parts of dielectric function, ω is photon frequency, μ_o is the permeability of free space [78]. The real part of the dielectric function $\epsilon_1(\omega)$ was evaluated from the imaginary part $\epsilon_2(\omega)$ by the Kramers-Kronig relationship [182].

6.2.2 Crystal structure

In the experimental results section, the crystallographic structure of as-synthesized GFCO nanoparticles was extensively investigated at room temperature by performing Rietveld refinement analysis of their powder XRD pattern. Notably, it was observed that GFCO crystallizes in monoclinic structure with *P2₁/n* space group. The lattice parameters of GFCO unit cell were found to be $a = 5.359(1)$ Å, $b = 5.590(2)$ Å, $c = 7.675(3)$ Å, monoclinic angle $\beta = 89.958(1)°$ with cell volume 229.920 Å^3. In the present investigation, first-principles calculation was performed to determine the structural parameters of GFCO by GGA ($U_{eff} = 0$ eV) and GGA + U (U_{eff} = 1- 6 eV) approaches.

The calculated lattice constants *a*, *b* and *c*, monoclinic angle (*β*) along with unit cell volume were tabulated in Table 6.4. For comparison, the experimentally obtained structural parameters were also included in the same table. Noticeably, the lattice constants and monoclinic angles obtained via first-principles calculation were found to be slightly larger than the experimental values. Nevertheless, this mismatch remained nominal i.e., within 3% of the experimental results which was consistent with a number of previous investigations [183, 184]. For instance, the lattice parameters of CO_2-metal organic framework calculated with Hubbard U corrections were reported to remain within 3% of experimental values [184]. Moreover, it was observed that the calculated lattice parameters and unit cell volume enhanced with the increment of U_{eff} from 0 to 6 eV [183]. In contrast, the monoclinic angle obtained by the GGA+U method decreased with increasing U_{eff} in the range of 1-6 eV. Such observations were in well agreement with previous investigations of related materials [183, 185].

Table 6.4 The calculated lattice parameters, monoclinic angle, unit cell volume, average of Fe-O and Cr-O bond lengths for different values of U_{eff} along with the corresponding experimental values.

	$U_{eff}=$ 0 eV	$U_{eff}=$ 1 eV	$U_{eff}=$ 2 eV	$U_{eff}=$ 3 eV	$U_{eff}=$ 4 eV	$U_{eff}=$ 5 eV	$U_{eff} =$ 6 eV	**Experimental Value**
a (Å)	5.397	5.442	5.448	5.457	5.466	5.470	5.502	5.359
b (Å)	5.601	5.676	5.682	5.689	5.698	5.701	5.750	5.590
c (Å)	7.688	7.781	7.798	7.808	7.820	7.821	7.886	7.675
β (°)	89.691	90.004	90.003	89.998	89.991	89.990	89.989	89.958
Volume(Å^3)	232.43	240.35	241.42	242.46	243.73	243.85	249.54	229.92

6.2.3 Electronic properties

Electronic properties had a crucial role in determining the optical properties of perovskites. The electronic properties of GFCO double perovskite were studied from the calculated band structures and the density of states based on the optimized crystal structures. The band structure provides basic knowledge of condensed matter and solid-state physics, which described a compound's electronic behavior, such as electron energy level and energy band gap [181, 186].

6.2.3.1 Electronic band structure

The theoretical investigation was initiated by calculating the spin-polarized electronic band structure of GFCO within the GGA method ($U_{eff} = 0$ eV) as shown in Fig. 6.13(a). The dotted horizontal line between the valence and conduction bands represents the Fermi level [21]. As can be observed, for up-spin orientation, a direct electronic band gap of 0.84 eV was obtained whereas for down-spin, the band gap was found to be indirect having a value of 0.27 eV. Notably, both of these values were much smaller than the direct optical band gap ~2.0 eV of as-synthesized GFCO as confirmed by UV-visible and PL spectroscopic analyses. It was well known that electronic band gap of any material would be close to its optical band gap [187], hence it might be inferred that the band structure formed for $U_{eff} = 0$ eV was incorrect. Therefore, the electronic band structure of GFCO was determined via GGA+U method with $U_{eff} = 1$-6 eV.
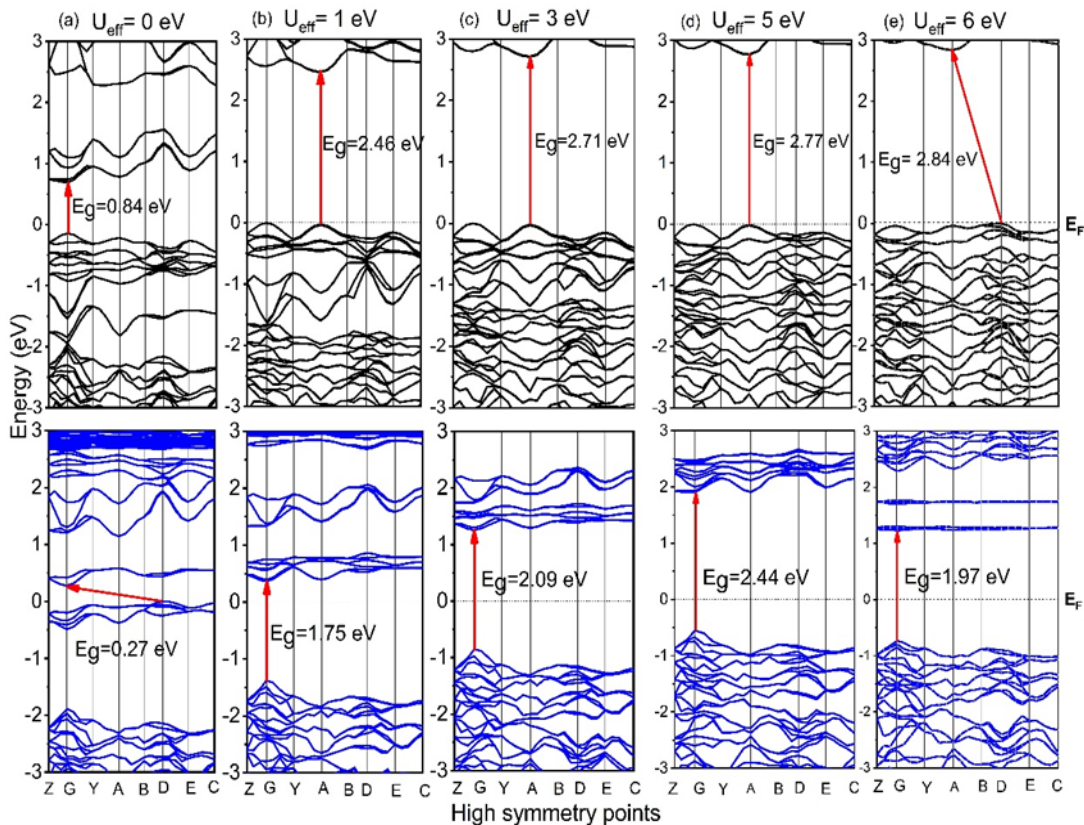
Fig. 6.13 Electronic band structure of Gd_2FeCrO_6 for (a) $U_{eff} = 0$ eV, (b) $U_{eff} = 1$ eV, (c) $U_{eff} = 3$ eV, (d) $U_{eff} = 5$ eV and (e) $U_{eff} = 6$ eV. Black and blue curves represent up-spin and down spin orientations, respectively. The energy ranges from -3 to 3 eV and the zero is set to the Fermi energy E_F.

The electronic band structures obtained for $U_{eff} = 1, 3, 5, 6$ eV were presented in Fig. 6.13(b-e), respectively. As can be seen from Fig. 6.13, the gap in the up-spin band

enlarged with increasing U_{eff} which might be attributed to the enhanced localization of the Fe-3d and Cr-3d orbitals due to increased U_{eff} [183]. It was worth noting that for U_{eff} = 1, 3, 5 eV, both the valence band maximum (VBM) and conduction band minimum (CBM) were within the A symmetry point indicating direct band structure.

However, at U_{eff} = 6 eV, an indirect up-spin band structure was obtained which was inconsistent with all the previous cases. It should be noted that so far both experimental and theoretical calculations provided strong evidence in support of direct band structure of GFCO. Therefore, the indirect band structure obtained for U_{eff} = 6 eV calls into question the applicability of employing large Hubbard parameter (i.e. U_{eff} > 5 eV) in first-principles calculations of GFCO double perovskite [183]. Moreover, it was interesting to note that the theoretically calculated up-spin band gap values were within the range of 2.46 - 2.84 eV which ensured the semiconducting nature of GFCO double perovskite as was also evident from the UV-visible and PL spectroscopic analyses (Fig. 6.10).

In the case of down-spin orientation, for all values of U_{eff} (1, 3, 5, 6 eV), both the CBM and VBM were obtained within the G symmetry point indicating again direct band structure. Interestingly, the band gap value increased monotonically from U_{eff} = 1-5 eV but an anomalous decrease can be observed at U_{eff} = 6 eV (Fig. 6.13(e)). Therefore, it might be conjectured that the optimized value of U_{eff} for first-principles calculation of GFCO would be less than 6 eV [183].

For understanding the carrier transport in the material, the curvature at band extrema were quantified by calculating the technologically important charge carrier effective masses using following expression [163].

$$m^* = \hbar^2 \left(\frac{d^2E}{dk^2}\right)^{-1} \qquad \cdots\cdots\cdots \quad (6.8)$$

Here, E is the band-edge energy as a function of wave-vector k. The electron effective mass (m_e^*) was calculated by parabolic fitting of the E-k curve within the small region of wave-vector near the CBM [163, 188]. The hole effective mass (m_h^*) was estimated by analyzing the region near the VBM using similar approach [163]. The variations of m_e^*
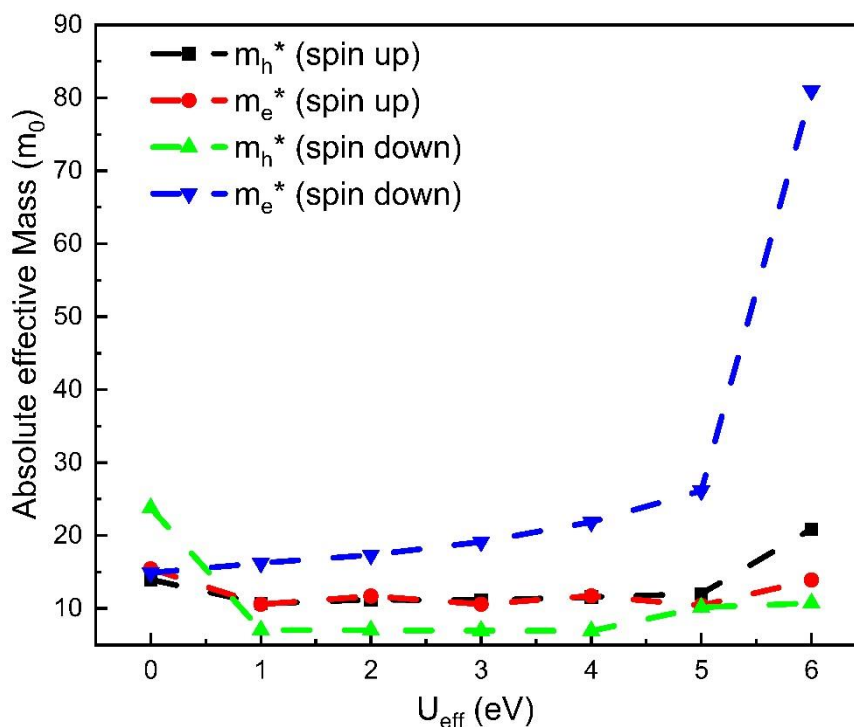
Fig. 6.14 Variation in absolute charge carrier effective mass as a function of U_{eff}. m_e^* and m_h^* are the electron and hole effective masses, respectively in units of the electron rest mass, m_o.

and m_h^* of GFCO double perovskite as a function of U_{eff} are illustrated in Fig. 6.14 both for up-spin and down-spin orientations. For up-spin band structure, m_e^* was reduced from 15.5 m_o to 10.6 m_o for $U_{eff} = 0$ eV to $U_{eff} = 1$ eV suggesting an increase in curvature at the CBM. Between U_{eff} of 1-5 eV, the values of m_e^* changed nominally (~1.3m_o). Further, for $U_{eff} = 6$ eV, an enhancement of 3.5 m_o was noticed which corresponded to the reduction in curvature at CBM. Clearly, in Fig. 6.14, a similar dependence of m_h^* on U_{eff} both for up and down-spin orientations was observed. Moreover, for down-spin band structure, a notable increase was noticed in m_e^* from 26.1 m_o to 81 m_o for $U_{eff} = 5$ eV to $U_{eff} = 6$ eV. However, the variation was comparatively smaller (~ 11.2 m_o) in the range of $U_{eff} = 0$-5 eV. It was worth mentioning that while varying the values of U_{eff} for electronic band structure calculation, the structural parameters were kept fixed at experimentally obtained values. Hence, it was confirmed that the variations in m_e^* and m_h^* with U_{eff} were solely due to the electronic effects. Such variation trend again justified that it would be worthwhile to consider U_{eff} within the range 1-5 eV for GFCO double perovskite.

6.2.3.2 Density of states

Further, in order to resolve the contribution of each individual orbital to the electronic bands of GFCO double perovskite, the total density of states (TDOS) and partial density of states (PDOS) of Gd-4f, Fe-3d, Cr-3d and O-2p orbitals of Gd_2FeCrO_6 perovskite were calculated using GGA+U method with $U_{eff} = 0, 1, 3, 5$ and 6 eV, as shown in Fig. 6.15. It was noteworthy that density of states provides numerical statistics on the availability of state at each energy level. A high density of states at a given energy level represented a high number of available energetic states for occupation [189] whereas a DOS of zero implied that no state was occupied at that energy level. Total and partial DOSs demonstrated the contribution of hybridized electrons in any atoms of the sample.

Beginning with the character of the conduction band ($E-E_F > 0$ eV) obtained for up-spin orientation, the following observations were made. At $U_{eff} = 0$ eV, Fig. 6.15(a), the conduction band lying at around 1 eV was made up of a hybridization of Fe-3d and O-2p orbitals. This band disappeared after considering the effect of Hubbard U_{eff} which corresponded to the decrement in m_e^* at $U_{eff} = 1$ eV (Fig. 6.15(b)). Notably, the conduction band (at around 2.5 eV) obtained for $U_{eff} = 1$ eV had primarily the characteristics of Cr-3d with a minor contribution from O-2p. Further, as shown in Fig. 6.15(c) and (d), with the increase of U_{eff} up to 5 eV, this conduction band shifted to higher energy resulting in the enlargement of band gap. Also, the contribution of Cr-3d to the up-spin conduction band enhanced with increasing U_{eff}. Interestingly, at $U_{eff} = 6$ eV (Fig. 6.15(e)), it was seen that the computed PDOS for Gd-4f orbital radically altered and the conduction band arose mainly due to the hybridization of Gd-4f with a minor contribution from Cr-3d orbital. Such anomaly was another indication for the limitation of $U_{eff} > 5$ eV to explain the electronic band structure of GFCO double perovskite accurately.

Now, if the valence bands ($E-E_F < 0$ eV) of up-spin electronic band structure were analyzed, as shown in Fig. 6.15(a), it might be observed that the valence band at $U_{eff} = 0$ eV was composed of Cr-3d, O- 2p as well as Fe-3d orbitals. However, when U_{eff} was used, the contribution of Fe-3d was diminished. To be specific, the up-spin valence band for $U_{eff} = 1$ eV was made up of the hybridization of Cr-3d and O-2p states (Fig. 6.15(b)). From Fig. 6.15(c), (d) and (e), it was noticed that with increasing U_{eff}, the contribution of Cr-3d state gradually decreased leaving only O-2p to dominate the valence band at $U_{eff} = 6$ eV which can be associated with the enhancement of m_h^*.
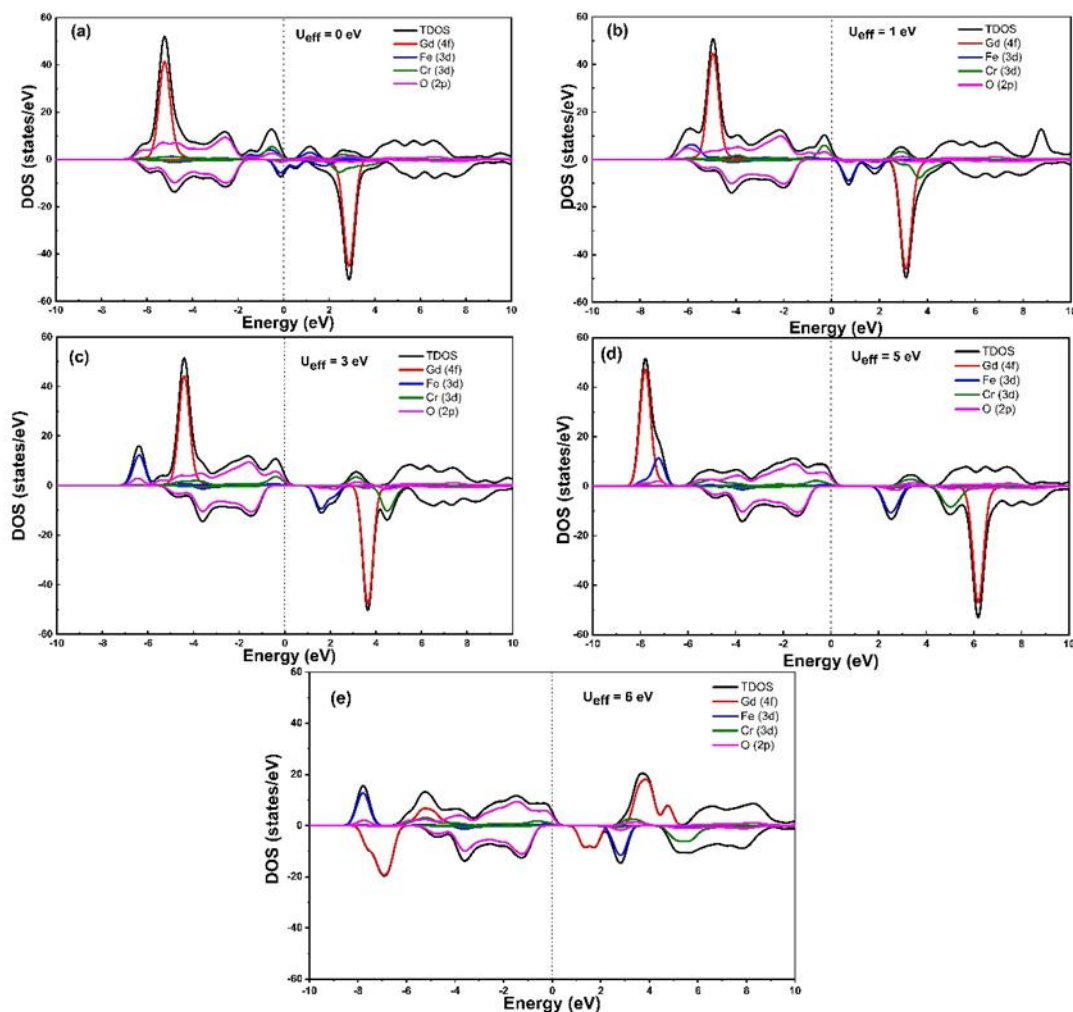
Fig. 6.15 Calculated total density of states (TDOSs) and partial density of states (PDOSs) of Gd-4f, Fe-3d, Cr-3d and O-2p orbitals for both up-spin and down-spin channels. The panels (a)-(e) show the DOSs for U_{eff} = 0, 1, 3, 5, 6 eV, respectively. The zero is set to the Fermi energy.

Further Fig. 6.15(a) demonstrated that at U_{eff} = 0 eV, the conduction band (E-E$_F$ > 0 eV) of down-spin structure was dominated mostly by Fe-3d orbital with a negligible contribution from O-2p. As can be noticed in Fig. 6.15(b), (c) and (e), the characteristics of the conduction band did not change much due to the effect of Hubbard U_{eff} up to 5 eV. Only a gradual shifting of conduction band to a higher energy was noticed with increasing U_{eff} as expected [183]. However, when a U_{eff} of 6 eV (Fig. 6.15(e)) was employed, a new flat conduction band appeared at around 1.25 eV owing to the sole contribution of Gd-4f state. Furthermore, in the case of the down-spin valence band (E-E$_F$ < 0 eV), a significant influence of U_{eff} was observed. Without considering the Coulomb repulsion effect (i.e., for U_{eff} = 0 eV in Fig. 6.15(a)), the valence band was obtained near the Fermi level which was attributed to the hybridization of Fe-3d and O-2p orbitals. After applying U_{eff} = 1 eV

(Fig. 6.15(b)), this band disappeared followed by the emergence of a new band at around - 1.5 eV which shifted gradually to higher energy with increasing U_{eff} of up to 6 eV (Fig. 6.15(b)-(e)). Notably, the formation of this band had the contribution from only O-2p orbital.

6.2.4 Mulliken population analysis

The effective atomic charge, bond population and bond length in a crystalline solid were obtained from Mulliken population analysis which provided insight into the distribution of electrons among different parts of the atomic bonds, covalency of bonding as well as bond strength [190, 191]. Mulliken effective charge, $Q(\alpha)$ of a particular atom was calculated using the following expression [191].

$$Q(\alpha) = \sum_k \omega_k \sum_\mu^{on\ \alpha} \sum_v P_{\mu v}(k) S_{\mu v}(k) \qquad \cdots\cdots\cdots \quad (6.9)$$

where $P_{\mu v}$ denotes an element of the density matrix and $S_{\mu v}$ refers to the overlap matrix. And the bond population, $P(\alpha\beta)$ between two atoms α and β can be expressed as [191]-

$$P(\alpha\beta) = \sum_k \omega_k \sum_\mu^{on\ \alpha} \sum_v^{on\ \beta} 2P_{\mu v}(k) S_{\mu v}(k) \qquad \cdots\cdots\cdots \quad (6.10)$$

Table 6.5 provided the calculated Mulliken effective charges of individual atoms, bond populations and bond lengths between different atoms in GFCO crystal structure. Noticeably, for all values of U_{eff}, the Mulliken effective charges of the individual Gd, Fe, Cr and O atoms were found to be reasonably smaller than their formal ionic charges which were +3, +3, +3, and -2, respectively. Such difference between Mulliken effective and formal ionic charges was an indication of the existence of mixed ionic and covalent bonding in GFCO [190]. It should be noted that small Mulliken effective charge of an atom was associated with its high level of covalency and vice versa [189, 191]. Therefore, it was inferred that GFCO double perovskite included chemical bonding with prominent covalency. Further, in Table 6.5, an enhancement was observed in the effective charges of Fe, Cr and O atoms after employing U_{eff} in the first-principles calculation (U_{eff} = 1-6 eV). This outcome indicated that the degree of bond covalency in GFCO reduced to an extent due to the effect of on-site Coulomb interaction.

Table 6.5 Mulliken effective charges of individual atoms, bond populations and bond lengths of Gd$_2$FeCrO$_6$ for different values of U$_{eff}$ obtained via Mulliken population analysis.

Atom		GGA+U					
	U$_{eff}$= 0 eV	U$_{eff}$=1 eV	U$_{eff}$= 2eV	U$_{eff}$=3 eV	U$_{eff}$= 4eV	U$_{eff}$= 5eV	U$_{eff}$= 6 eV
	Mulliken effective charge (e)						
Gd	1.52	1.49	1.49	1.49	1.49	1.50	1.50
Fe	0.59	0.78	0.79	0.80	0.82	0.82	0.84
Cr	0.53	0.58	0.59	0.61	0.62	0.63	0.65
O	-0.69	-0.72	-0.73	-0.73	-0.74	-0.74	-0.75
Bond		**Bond population**					
Gd-O	0.1450	0.1587	0.1600	0.1625	0.1637	0.1662	0.1700
Fe-O	0.3200	0.3100	0.3166	0.3166	0.3166	0.3166	0.3066
Cr-O	0.3533	0.3200	0.3200	0.3200	0.3200	0.3133	0.3100
O-O	-0.0350	-0.0333	-0.0333	-0.0333	-0.0333	-0.0333	-0.0333
Bond		**Bond length (Å)**					
Gd-O	2.475	2.501	2.504	2.505	2.507	2.507	2.524
Fe-O	2.023	2.051	2.061	2.065	2.065	2.069	2.083
Cr-O	2.026	2.036	2.042	2.049	2.050	2.057	2.079

Table 6.5 also presented the bond populations and bond lengths of Gd-O, Fe-O, Cr-O and O-O bonds in GFCO double perovskite as obtained for U$_{eff}$ = 0-6 eV. It was noteworthy that a large positive value of bond population was associated with high degree of covalency whereas a small bond population indicates high degree of ionicity in the chemical bond [192]. In the present investigation, the bond populations of the Gd-O, Fe-O and Cr-O were determined to be positive whereas the bond population of O-O was negative for all values of U$_{eff}$. This result suggested that no bonds had formed between the O atoms in GFCO double perovskite [181, 186]. Moreover, the calculated bond populations of Fe-O and Cr-O were found to be considerably larger than that of Gd-O. Such observation implied that the Fe-O and Cr-O bonds possess higher degree of covalency as compared to Gd-O bonds. It was also worth noticing that the bond populations of Fe-O and Cr-O calculated by GGA+U method (U$_{eff}$ = 1-6 eV) were lower than the values obtained by GGA method (U$_{eff}$ = 0 eV). This result provided further evidence for the influence of Coulomb repulsion to reduce the covalency of Fe-O and Cr-O bonding in GFCO as was observed before by analyzing the calculated Mulliken effective charges. Furthermore, Table 6.5 demonstrated that the bond lengths of Fe-O and Cr-O were reasonably smaller than that of Gd-O which can be attributed to their larger bond population and consequently, higher degree of covalency as compared to Gd-O

bonding.

6.2.5 Electron charge density

For further understanding of the chemical bonding nature, the electron charge density distribution of GFCO double perovskite was determined along the z-axis by GGA (U_{eff} = 0 eV) and GGA + U (U_{eff} = 1, 3 and 6 eV) methods as illustrated in Fig. 6.16. It was worth noting that a typical covalent bond between two atoms involves overlapping of electron clouds from both of them and the electrons remained concentrated in the overlapping region [193]. In Fig. 6.16, for all values of U_{eff}, a larger overlap of electron cloud was observed between Fe/Cr and O atoms as compared to Gd and O atoms. Such observation implied that the covalent bonds between Fe/Cr and O in GFCO were considerably stronger than the bond between Gd and O as was also revealed by Mulliken population analysis.
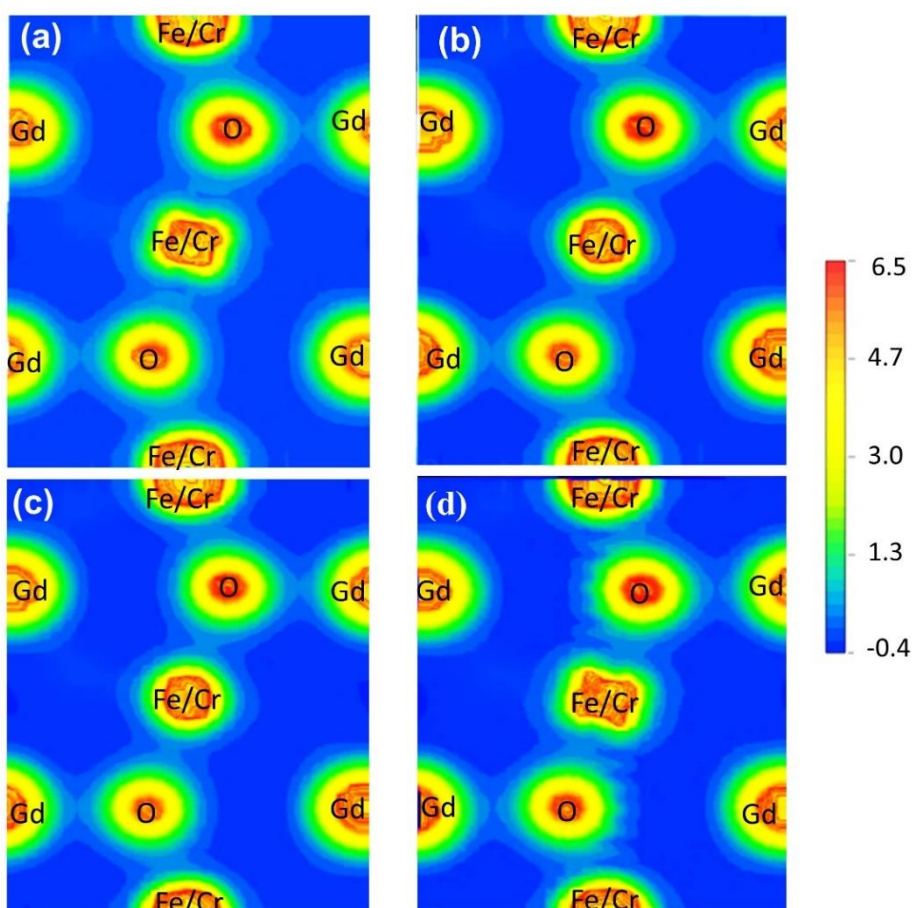
Fig. 6.16 Electronic charge density along z-axis of Gd_2FeCrO_6 for (a) U_{eff} = 0 eV, (b) U_{eff} = 1 eV, (c) U_{eff} = 3 eV, and (d) U_{eff} = 6 eV.

Moreover, no electron clouds could be seen in the region between one of the two Gd atoms and O, implying the establishment of an ionic bond between these two atoms [189],

[194]. Notably, the charge sharing between Fe/Cr and O was attributed to the hybridization among Fe/Cr-3d and O-2p orbitals and the Gd-O bond formation was associated with the hybridization between Gd-4f and O-2p orbitals, as shown by the DOS curves (Fig. 6.15).

Furthermore, after including the influence of on-site Coulomb interaction (U_{eff}) in first-principles calculations, the overlapping of electron clouds between Fe/Cr and O atoms became relatively narrower, as shown in Fig. 6.16(a) and (b). Afterward, the electron charge density in the overlapped region between Fe/Cr and O atoms enhanced with increasing U_{eff} (Fig. 6.16(c) and (d)) which was consistent with the outcome of Mulliken population analysis.

6.2.6 Light absorption property

The absorption coefficient provides valuable information about a material's light-harvesting ability. The optical absorption coefficient of GFCO was evaluated by first-principles calculation via GGA ($U_{eff} = 0$ eV) and GGA+U ($U_{eff} = 1$-6 eV) approaches using a polarization technique which included the electric field vector as an isotropic average in all directions [195]. To gain additional distinguishable absorption peaks, a small smearing value of 0.5 eV was used. Fig. 6.17(a) illustrated the calculated absorption coefficients of GFCO double perovskite as a function of wavelength to demonstrate the effect of Hubbard U_{eff} parameter on its light absorption property. In Fig. 6.17(a), for all values of U_{eff}, two absorption peaks were clearly observed in the UV region which indicated the strong UV light absorption capacity of GFCO. Noticeably, the stronger absorption coefficient peak was located at around 120 nm and it was slightly redshifted as U_{eff} increased. On contrary, the weaker absorption peak at around 320 nm was slightly blue-shifted for higher values of U_{eff}. It was worth noticing that the experimentally obtained spectrum (Fig. 6.10) had two additional bands in the visible region along with the two bands as obtained theoretically in the UV regime. This might be related to the fact that the DFT calculations were performed for 0 K whereas the experiment was conducted at room temperature. Such difference in conditions was attributed to the discrepancy between the optical and theoretical absorbance spectra of GFCO [196, 197].

Fig. 6.17(b) showed the absorption coefficient vs U_{eff} curves of GFCO for some fixed values of wavelength ranging from 150 to 600 nm. It should be noted that for the wavelength of 150 nm, the absorption coefficient attained its minimum and maximum

values for U_{eff} = 4 eV and U_{eff} = 5 eV, respectively suggesting that the coefficient was underestimated and overestimated for these U_{eff} values. Similarly, it was found that except at U_{eff} = 3 eV, the absorption coefficient was either overestimated or underestimated at all other values of U_{eff} for any of the specific wavelengths such as 200, 250, 300 nm etc. This intriguing observation was highlighted by the rectangle in Fig. 6.17(b).
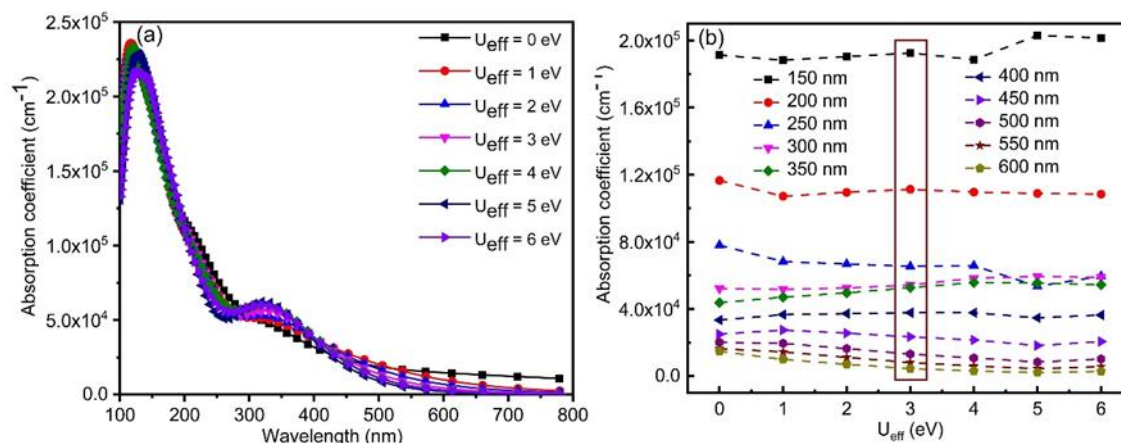
Fig. 6.17 (a) Variation of theoretically obtained absorption coefficient of Gd_2FeCrO_3 perovskite as a function of wavelength for different U_{eff}. (b) The absorption coefficient vs. U_{eff} for some fixed values of the wavelength.

6.2.7 Comparison of experimental and theoretical optical band gaps

Further, the calculated absorption coefficients were employed to theoretically calculate the optical band gap values of GFCO double perovskite using Tauc relation [159]. Fig. 6.18 showed the variation in theoretically calculated direct band gap values as a function of U_{eff}. Noticeably, a direct band gap value of 0.5 eV was obtained by GGA method (U_{eff} = 0 eV) which was significantly smaller than the experimental value ~2.0 eV. Further, with the increase of U_{eff} up to 5 eV, an almost linear increase was observed in the direct optical band gap values of GFCO double perovskite. However, an anomalous decrease was noticed for a further increase of U_{eff} to 6 eV. It was intriguing to note that the direct optical band gap (~1.99 eV) obtained for U_{eff} = 3 eV matched well with the experimentally obtained one (~2.0 eV) which was marked by a circle in Fig. 6.18. Also, the calculated band gap value (2.08 eV) for U_{eff} = 6 eV was very similar to that of the observed measurement. But as demonstrated before, the character and curvature of the conduction and valence bands inaccurately changed for U_{eff} > 5 eV. Hence, fitting U_{eff} to the band gap alone provided erroneous results for such double perovskite materials especially in the cases where the role of the band edge character was crucial.

.
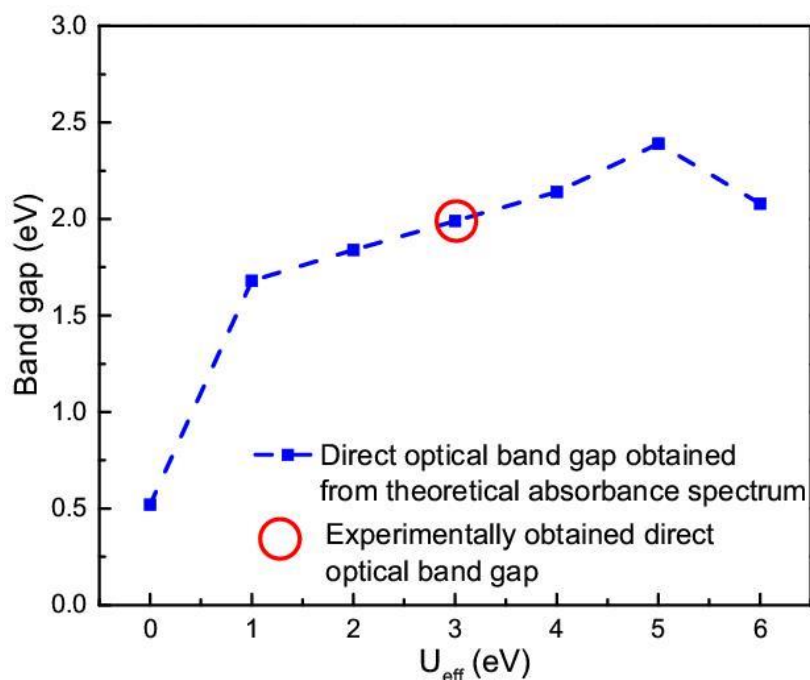
Fig. 6.18 Variation in theoretically calculated direct optical band gap as a function of U_{eff}. The red circle represents the experimentally obtained optical band gap value.

Finally, it was fascinating to note that the predictions for all the properties of GFCO (i.e., structural, electronic, and optical) considering $U_{eff} = 3$ eV closely matched with the experimental results without any over or underestimation of band gap values. This could be implied that the U_{eff} value of 3 eV most accurately localized the Fe-3d and Cr-3d orbitals of GFCO. Moreover, the almost accurate estimation of band gap values suggested that the effect of self-interaction error from the other orbitals of GFCO was almost negligible [198, 199]. Therefore, $U_{eff} = 3$ eV is recommended for the GGA+U calculation of electronic and optical properties of GFCO double perovskite.

CHAPTER 7

SUMMARY AND CONCLUSIONS

7.1 Summary

The outcomes of this investigation are summarized as:

- The parent single perovskites $NdCrO_3$ and $NdFeO_3$ were initially studied using first-principles DFT calculations to investigate the physical properties of Nd_2FeCrO_6 double perovskite. The G-type AFM arrangement of spins exhibits the lowest energy for all values of U for single perovskites $NdCrO_3$ and $NdFeO_3$, and the symmetry analysis of the optimized structures revealed the orthorhombic phase with the *Pnma* space group. Likewise, the parent single perovskites $NdFeO_3$ and $NdCrO_3$, for $U = 3.5$ eV double perovskite Nd_2FeCrO_6 also showed that G-type AFM arrangement of Fe and Cr spins are energetically favorable.

- DFT studies showed that due to the G-type AFM spin arrangement with $Fe^{3+}_\uparrow$-O-$Fe^{3+}_\downarrow$ and $Cr^{3+}_\uparrow$-O-$Cr^{3+}_\downarrow$ super-exchange interactions, the single parent perovskite oxides $NdFeO_3$ and $NdCrO_3$, respectively had no net magnetic moment. However, Nd_2FeCrO_6 possesses a net magnetic moment of $\sim 2\mu_B$/f.u. due to $Fe^{3+}_\uparrow$-O-$Cr^{3+}_\downarrow$ super-exchange interaction with an ordering temperature of ~ 265 K.

- Using DFT calculations, the band structure and DOS calculations of Nd_2FeCrO_6 double perovskite were analyzed critically. It was found that Nd_2FeCrO_6 double perovskite is a semiconductor material and with a direct band gap of ~ 1.85 eV. The density of states also showed that hybridized O-$2p$+Cr-$3d(t_{2g})$ orbitals dominate at the top of the valence band whereas Fe-$3d(t_{2g})$+O-$2p$ states dominate at the bottom of the conduction band.

- The thermodynamic, mechanical, and dynamic stability results demonstrated that it was possible to synthesis Nd_2FeCrO_6 double perovskite at ambient pressure.

- The double perovskite Nd_2FeCrO_6 were successfully synthesized by sol-gel technique as anticipated by theoretical predictions. Another double perovskite,

Gd_2FeCrO_6 were also synthesized using the same synthesis route. Rietveld refinement of powder XRD patterns of Nd_2FeCrO_6 and Gd_2FeCrO_6 were carried out to detect the samples' crystallographic phases that confirmed single-phase Nd_2FeCrO_6 and Gd_2FeCrO_6 perovskites without any impurity phases. The Rietveld refinement also ensured the orthorhombic and monoclinic crystal structures with space group *Pnma* and *P2₁/n*, respectively. Atomic positions, bond length and bond angles were also extracted from Rietveld refined XRD patterns. Unequal bond lengths of Fe/Cr-O and Fe-O-Cr's bond angles ensured the presence of Jahn-Teller distortion and octahedral tilting, respectively. The average tilt angles 13.76º and 15.96º, respectively, confirmed the structural distortion of the Nd_2FeCrO_6 and Gd_2FeCrO_6 unit cells.

- The FTIR spectra of Nd_2FeCrO_6 and Gd_2FeCrO_6 indicated the existence of bending and stretching vibrations of Fe/Cr-O bonds in the Fe/CrO_6 octahedra. At room temperature, Raman spectroscopy was used to analyze the crystal structure, cation disorder, and spin-phonon coupling of as-synthesized Nd_2FeCrO_6 and Gd_2FeCrO_6 double perovskites. The Raman spectrum of Nd_2FeCrO_6 and Gd_2FeCrO_6 displayed two broad modes around 500 cm^{-1} and 700 cm^{-1}, corresponding to B_g and A_g modes, respectively. From the Raman spectra of Nd_2FeCrO_6 and Gd_2FeCrO_6, the Fe/Cr-O bond length was found to be 1.954 Å and 1.95 Å, respectively, which agree well with the value obtained from the XRD investigation.

- The FESEM image demonstrated that the particle size of Nd_2FeCrO_6 and Gd_2FeCrO_6 double perovskites were mostly within the range of ~ 40 to 130 nm with an average ~70 nm.

- For both compounds, the existence of mixed-valence states of Fe (Fe^{2+} and Fe^{3+}) and Cr (Cr^{2+} and Cr^{3+}) were confirmed by XPS analysis.

- Temperature-dependent magnetization measurements of Nd_2FeCrO_6 revealed two magnetic transitions at 251 K (T_{N1}) and 53 K (T_{N2}). Under field cooling conditions, the M-T curves of this double perovskite showed magnetic reversal behavior at a low temperature of 6 K. The exchange bias effect was observed in this double perovskite material while the sample was cooled down from 300 K to 10 K and cooling magnetic fields (H_{cool}) were applied.

- Temperature-dependent magnetization measurements of Gd_2FeCrO_6 nanoparticles demonstrated a divergence below 50 K which gradually enlarged at lower temperature below 20 K. Moreover, the ZFC curve exhibited a cusp-like feature at T~15 K, suggesting a Néel transition. At 5 K, a nearly saturated small magnetic hysteresis loop with saturation magnetization, M_S of ~84 emu/g was observed.

- Both UV-visible absorbance and photoluminescence spectra were taken to calculate the optical band gaps of Nd_2FeCrO_6 and Gd_2FeCrO_6 nanoparticles. The direct optical band gap of Nd_2FeCrO_6 and Gd_2FeCrO_6 double perovskites were found to be 1.95 eV and 2.00 eV, respectively.

- The estimated valence band edge position of Nd_2FeCrO_6 nanoparticles was found to be greater than the potential of O_2/H_2O, implying that O_2 gas could evolve using this material as a photocatalyst, while the conduction band edge potential was found to be less negative than the H^+/H_2 potential, implying the possibility of photocatalytic H_2 evolution. The estimated valence band edge position of Gd_2FeCrO_6 double perovskite was found to be larger than the potential of O_2/H_2O.

- The physical properties of Gd_2FeCrO_6 double perovskite were also investigated theoretically using experimentally obtained structural parameters by employing GGA and GGA+U approaches. First-principles DFT calculations suggested that the effect of Hubbard parameter, U_{eff} (1 to 6 eV) on the lattice parameters of Gd_2FeCrO_6 perovskite was nominal. On the contrary, a significant effect was observed on the electronic structure and band gap of double perovskite Gd_2FeCrO_6.

- Using DFT calculations, the band structures of Gd_2FeCrO_6 were analyzed critically. It was found that Gd_2FeCrO_6 is a direct band gap semiconductor.

- The DOS estimated using the GGA+U approach (U_{eff}= 1, 3, 5, and 6 eV) revealed that the valence band maximum of Gd_2FeCrO_6 arose from the hybridization of Fe-3d, Cr-3d, and O-2p states for up spin orientation, but the conduction minimum was made up of Cr-3d and O-2p hybridization states. The valence band maximum in the down spin channel was related to the hybridization of Cr-3d and O-2p states, whereas the conduction band minimum

was assigned to Fe-3d and O-2p hybridization states.

- The experimentally obtained optical band gap~ 2.0 eV was in excellent agreement with the theoretically calculated band gap of 1.99 eV for $U_{eff} = 3eV$.

Table 7.1 Comparison among experimental different parameters of as-synthesized Nd_2FeCrO_6 and Gd_2FeCrO_6 double perovskites.

	Nd_2FeCrO_6	**Gd_2FeCrO_6**
Synthesis technique	Citrate based sol-gel	Citrate based sol-gel
Tolerance factor	0.94	0.91
Crystal structure	Orthorhombic	Monoclinic
Space group	*Pnma*	*P2$_1$/n*
Lattice parameter	$a = 5.523 (0)$ Å, $b = 7.724$ (1) Å, $c = 5.435(2)$ Å,	$a = 5.359 (1)$ Å, $b = 5.590 (2)$ Å, c = 7.674 (3) Å, $\beta = 89.958 (1)$ º
Unit cell volume	231.9 Å^3	229.9 Å^3
Average bond length of Fe/Cr-O	1.99 Å (from Rietveld) ~1.954 Å (from Raman spectrum)	1.99 Å (from Rietveld) ~ 1.95 Å (from Raman spectrum)
Average bond angle between Fe/Cr-O-Fe/Cr	152.47 º	148.07 º
Tilt angle	13.76 º	15.96 º
Average crystallite size	29 nm	56 nm
Particle size	Around ~70 nm (FESEM) Around ~55 nm (TEM)	Around ~70 nm (FESEM) 60-100 nm (TEM)
Thermal stability	Stable up to 1000 ºC	Stable up to 1000 ºC
Magnetic nature	Coexistence of weak ferromagnetic and antiferromagnetic nature	Coexistence of ferromagnetic and antiferromagnetic nature
Transition temperature	$T_{N1} = 251$ K and $T_{N1} = 53$ K	$T_N = 15$ K
Magnetization reversal	Present	Not present
Exchange bias effect	Present	Present
Material type	Semiconductor	Semiconductor
Band gap	1.95 eV (direct)	2.0 eV (direct)
Maximum absorption region	UV region	UV region

7.2 Conclusions

First-principles DFT calculations suggested that compared to the AFM nature of the parent single perovskites $NdFeO_3$ and $NdCrO_3$, the nature of B site ordered double perovskite Nd_2FeCrO_6 is a ferrimagnetic ground-state with a total magnetization of 2 μ_B

per formula unit due to the Fe^{3+}-O-Cr^{3+} super-exchange interaction. The band structure and density of states calculations confirmed the semiconducting nature of this material with a direct band gap of ~1.85 eV which is significantly smaller than the band gaps of its parent single perovskites. Notably, the crystallographic structure and physical properties of most of the single perovskite materials are experimentally well established, however, double perovskites are comparatively less investigated. Therefore, the experimental data for various double perovskites are always not available. This first-principles DFT investigation might pave the way for the theoretical prediction of the physical properties of any new double perovskite materials by employing the experimental parameters of their parent single perovskites and optimizing the effects of on-site d-d Coulomb interaction energy within GGA+U calculations.

Based on the outcome of DFT calculations, Nd_2FeCrO_6 double perovskite was synthesized via sol-gel method and its structural, magnetic and optical properties were investigated extensively. The XPS study confirmed the existence of mixed oxidation states of Fe and Cr in the Nd_2FeCrO_6 nanoparticles. A temperature and field-dependent magnetization investigation revealed the presence of both weak ferromagnetic and antiferromagnetic domains in Nd_2FeCrO_6 double perovskite which resulted in magnetization reversal in the field-cooled mode at compensation temperature (T_{comp}) of 6K. The exchange bias effect is observed which is attributed to the interaction between the Nd and Fe/Cr sublattices. The exchange bias field values showed an increasing trend with an applied magnetic field while the sample was cooled from room temperature to 10 K. It is anticipated that the newly synthesized Nd_2FeCrO_6 double perovskite with simultaneous presence of magnetization reversal and exchange bias may be a promising option to be used in innovative multifunctional devices. Moreover, the estimated band gap of Nd_2FeCrO_6 perovskite was within the visible range; which suggest that this synthesized direct band gap semiconductor might have the ability to function as a photocatalytic material.

The Rietveld refined powder XRD pattern and electron microscopy imaging demonstrated the successful synthesis of Gd_2FeCrO_6 nanoparticles with ~ 70 nm average particle size. During field cooling, the increase of magnetization with decreasing temperature without any sharp transition indicated the absence of proper long-range order among Fe^{3+} and Cr^{3+} ions as was also suggested by XRD and XPS analyses. As a consequence, the coexistence of FM and AFM states in Gd_2FeCrO_6 double perovskite

was observed at 5 K. This was further evident from the emergence of intrinsic exchange bias effect at 5 K. Both UV–visible and photoluminescence spectroscopic analyses demonstrated that band gap of Gd_2FeCrO_6 perovskite is within visible range and therefore, it can be concluded that this synthesized direct band gap semiconductor might have the ability to function as a photocatalyst material. Moreover, the band edge positions of as-synthesized Gd_2FeCrO_6 nanoparticles revealed that the valence band maximum potential is sufficiently positive with respect to the oxidation potential of water which unveils the promising potential of these nanoparticles to be employed in photocatalytic oxygen evolution from water.

The first-principles based GGA and GGA+U methods have employed to calculate the spin polarized electronic band structure, Mulliken bond population, electron charge density distribution and optical characteristics of the newly synthesized direct band gap semiconductor Gd_2FeCrO_6 double perovskite for a range of U_{eff} between 0 and 6 eV, applied to the Fe-3d and Cr-3d orbitals. The structural parameters of the monoclinic Gd_2FeCrO_6 crystal varied nominally with U_{eff}. To the contrary, the variation of U_{eff} demonstrated significant effect on the electronic band structure which indicated the importance of employing a reasonable value of U_{eff} to correct the over-delocalization of the Fe/Cr-3d states. For $U_{eff} > 5$ eV, the computed partial density of states for Gd-4f orbital radically altered which had significantly changed the band structure. In particular, it is seen that the character and curvature of the conduction and valence bands largely varied for $U_{eff} > 5$ eV leading to enormous changes in calculated charge carrier effective masses. Notably, in the case of $U_{eff} = 3$ eV, the theoretically calculated direct optical band gap ~1.99 eV matched well with the experimental value ~2.0 eV. These findings justify that it might be worthwhile to employ $U_{eff} = 3$ eV to accurately calculate the structural, electronic and optical properties of Gd_2FeCrO_6 double perovskite. The outcome of this investigation might be useful for a keen understating of the electronic and optical properties of this newly synthesized double perovskite and related material systems for photocatalytic applications via band gap engineering. This study also revealed the importance of conducting systematic analysis of the influence of on-site Coulomb interaction on band gaps as well as on the electronic structure as a whole for related other double perovskite materials for which experimental data are still not available.

7.3 Scope for future work

- The theoretical investigations were carried out on ordered double perovskites. The physical properties of disordered Nd_2FeCrO_6 and Gd_2FeCrO_6 double perovskites may also be studied theoretically.

- To observe antisite disorder (if any) in Nd_2FeCrO_6 and Gd_2FeCrO_6 double perovskites, Lorentz transmission electron microscopy imaging may also be carried out. Magnetoresistance measurements (if any) may also be carried out.

- Due to suitable band gap and band edge positions of Nd_2FeCrO_6 and Gd_2FeCrO_6, experiments on their photocatalytic dye degradation and hydrogen production via water splitting may be conducted.

List of publications

List of publications (from Ph.D. thesis)

[1] **Bhuyan, M. D. I.**, Das, S. and Basith, M. A., "Sol-gel synthesized double perovskite Gd_2FeCrO_6 nanoparticles: Structural, magnetic and optical properties", *J. Alloys Compd.*, vol. 878, p. 160389, 2021.

[2] **Bhuyan, M. D. I.**, Rana Hossain, Ferdous Ara and Basith, M. A., "First-principles study on phase stability and physical properties of B-site ordered Nd_2CrFeO_6 double perovskite", *Phys. Chem. Chem. Phys.,* vol. 24, pp.1569-1579, 2022.

[3] Das, S., **Bhuyan, M. D. I.** and Basith, M. A., "First-principles calculation of the electronic and optical properties of Gd_2FeCrO_6 double perovskite: Effect of Hubbard U parameter", *J. Mater. Res. Technol.*, vol. 13, pp. 2408-2418, 2021.

List of publications (as a co-author)

[1] Tama, A. M., Das, S., Dutta, S., **Bhuyan, M. D. I.**, Islam, M. N. and Basith, M. A., 2019. "MoS_2 nanosheet incorporated α-Fe_2O_3/ZnO nanocomposite with enhanced photocatalytic dye degradation and hydrogen production ability", *RSC Adv.*, vol. 9(69), pp. 40357-40367, 2019.

[2] Das, S., Sultana, I., **Bhuyan, M. D. I.**, and Basith, M. A., "Enhanced Magnetic Softness of Double-Layered Perovskite Manganite $La_{1.7}Gd_{0.3}SrMn_2O_7$", *IEEE Magn. Lett.*, vol. 10, pp. 1-4, 2019.

Conference presentations

[1] **Bhuyan, M. D. I.**, Rana Hossain, Ferdous Ara and Basith, M. A., "A first-principles study on phase stability, electronic and magnetic properties of a B-site ordered Nd_2CrFeO_6 double perovskite", Poster presentation, International Symposium of Nanotechnology-2022, 24 January 2022.

[2] **Bhuyan, M. D. I.**, Rana Hossain, and Basith, M. A., "Structural, magnetic, electronic and optical properties of Nd_2FeCrO_6 double perovskite: A first-principles study", Oral presentation, National Conference on Physics-2021, 06-07 August 2021.

[3] **Bhuyan, M. D. I.**, Das, S., and Basith, M. A., "A first-principles study on the electronic and optical properties of Nd_2FeCrO_6 double perovskite", Poster

presentation, 4th International Conference on Nanomaterials Science and Mechanical Engineering, University of Aveiro, Portugal, July 6-9, 2021.

[4]   **Bhuyan, M. D. I.**, Das, S., and Basith, M. A., "Structural and magnetic properties of Gd_2FeCrO_6 double perovskite", Oral presentation, Sixth Conference of Bangladesh Crystallographic Association (BCA), 2021.

[5]   **Bhuyan, M. D. I.**, Das, S., and Basith, M. A., "Structural, magnetic and optical properties of Gd_2FeCrO_6 double perovskites synthesized by sol-gel technique", Poster presentation, International Conference on Physics-2020, Atomic Energy Centre, Dhaka, Bangladesh, 2020.

References

[1] Vasala, S. and Karppinen, M., "$A_2B'B''O_6$ perovskites: A review", *Prog. Solid State Chem.*, vol. 43, pp. 1-36, 2015.

[2] Mazumdar, D. and Das, I., "Layered Double Perovskites", *Phys. Chem. Chem. Phys.*, vol. 23, pp. 5596-5606, 2021.

[3] Kangsabanik, J., Sugathan, V., Yadav, A., Yella, A., and Alam, A., "Double perovskites overtaking the single perovskites: A set of new solar harvesting materials with much higher stability and efficiency", *Phys. Rev. Mater.*, vol. 2, p. 055401, 2018.

[4] Evans, H. A., Mao, L., Seshadri, R. and Cheetham, A. K., "Structural, magnetic, and magnetocaloric properties of the multiferroic host double perovskite compound Pr_2FeCrO_6", *Annu. Rev. Mater. Res.*, vol. 51, p. 351, 2021.

[5] Gray, B., Lee, H. N., Liu, J., Chakhalian, J., and Freeland, J. W., "Local electronic and magnetic studies of an artificial La_2FeCrO_6 double perovskite", *Appl. Phys. Lett.*, vol. 97, p. 013105, 2010.

[6] Das, H., Waghmare, U. V., Saha-Dasgupta, T., and Sarma, D. D., "Electronic structure, phonons, and dielectric anomaly in ferromagnetic insulating double pervoskite La_2NiMnO_6", *Phys. Rev. Lett.*, vol. 100, p. 186402, 2008.

[7] Bull, C. L., Gleeson, D., and Knight, K. S., "Determination of B-site ordering and structural", *J. Phys. Condens. Matter*, vol. 15, pp. 4927-4936, 2003.

[8] Costilla-Aguilar, S. U., Escudero, M. J., Cienfuegos-Pelaes, R. F., and Aguilar-Martínez, J. A., "Double perovskite $La_{1.8}Sr_{0.2}CoFeO_{5+\delta}$ as a cathode material for intermediate temperature solid oxide fuel cells", *J. Alloys Compd.*, vol. 862, p. 158025, 2021.

[9] Kim, M. K., Moon, J. Y., Oh, S. H., Oh, D. G., Choi, Y. J., and Lee, N., "Strong magnetoelectric coupling in mixed ferrimagnetic-multiferroic phases of a double perovskite", *Sci. Rep.*, vol. 9, pp. 1-10, 2019.

[10] Hossain, A., Bandyopadhyay, P., and Roy, S., "An overview of double perovskites $A_2B'B''O_6$ with small ions at A site: Synthesis, structure and magnetic properties", *J. Alloys Compd.*, vol. 740, pp. 414-427, 2018.

[11] Mandal, T. K. and Gopalakrishnan, J., "New route to ordered double perovskites : synthesis of rock salt oxides, Li_4MWO_6, and their transformation to Sr_2MWO_6 (M= Mg, Mn, Fe, Ni)", *Chem. Mater.*, vol. 6, pp. 2310-2316, 2005.

[12] Shimada, T., Nakamura, J., Motohashi, T., Yamauchi, H., and Karppinen, M., "Kinetics and thermodynamics of the degree of order of the B cations in double-perovskite Sr_2FeMoO_6", *Chem. Mater.*, vol. 15, pp. 4494-4497, 2003.

[13] Yoshimatsu, K., Ishimaru, J., Watarai, K., Yamamoto, K., Hirata, Y., Wadati, H., Takeda, Y., Horiba, K., Kumigashira, H., Sakata, O., and Ohtomo, A., "Magnetic and electronic properties of B -site-ordered double-perovskite oxide La_2CrMnO_6 thin films", *Phys. Rev. B*, vol. 99, pp. 1-8, 2019.

[14] Qiao, Y., Zhou, Y., Wang, S., Yuan, L., Du, Y., Lu, D., Che, G., and Che, H., "Composition dependent magnetic and ferroelectric properties of hydrothermally synthesized $GdFe_{1-x}Cr_xO_3$ ($0.1 \leq x \leq 0.9$) perovskites", *Dalt. Trans.*, vol. 46, pp. 5930-5937, 2017.

[15] Nair, V. G., Pal, L., Subramanian, V., and Santhosh, P. N., "Structural, magnetic, and magnetodielectric studies of metamagnetic $DyFe_{0.5}Cr_{0.5}O_3$", *J. Appl. Phys.*, vol. 115, pp. 2012-2015, 2014.

[16] Bolletta, J. P., Pomiro, F., Sánchez, R. D., Pomjakushin, V., Aurelio, G., Maignan, A., Martin, C., and Carbonio, R. E., "Spin reorientation and metamagnetic transitions in $RFe_{0.5}Cr_{0.5}O_3$ perovskites (R=Tb, Dy, Ho, Er)", *Phys. Rev. B*, vol. 98, p. 134417, 2018.

[17] Hossain, R., Billah, A., Ishizaki, M., Kubota, S., Hirose, F., and Ahmmad, B., "Oxygen vacancy mediated room-temperature ferromagnetism and band gap narrowing in $DyFe_{0.5}Cr_{0.5}O_3$ nanoparticles", *Dalt. Trans.*, vol. 50, pp. 9519-9528, 2021.

[18] Yuan, L., Huang, K., Hou, C., Feng, W., Wang, S., Zhou, C., and Feng, S., "Hydrothermal synthesis and magnetic properties of $REFe_{0.5}Cr_{0.5}O_3$ (RE = La, Tb, Ho, Er, Yb, Lu and Y) perovskite", *New J. Chem.*, vol. 38, pp. 1168-1172, 2014.

[19] Yin, L. H., Yang, J., Zhang, R. R., Dai, J. M., Song, W. H., and Sun, Y. P., "Multiferroicity and magnetoelectric coupling enhanced large magnetocaloric effect in $DyFe_{0.5}Cr_{0.5}O_3$", *Appl. Phys. Lett.*, vol. 104, pp. 1-6, 2014.

[20] Sharannia, M. P., De, S., Singh, R., Das, A., Nirmala, R., and Santhosh, P. N., "Observation of magnetization and exchange bias reversals in $NdFe_{0.5}Cr_{0.5}O_3$", *J. Magn. Magn. Mater.*, vol. 430, pp. 109-113, 2017.

[21] Hou, L., Shi, L., Zhao, J., Tong, R., and Xin, Y., "Insight into the magnetization reversal and exchange bias in $RFe_{0.5}Cr_{0.5}O_3$ ceramics", *J. Phys. Chem. C*, vol. 125, pp. 7950-7958, 2021.

[22] Blessington Selvadurai, A. P., Pazhanivelu, V., Jagadeeshwaran, C., Murugaraj, R., Panneer Muthuselvam, I., and Chou, F. C., "Influence of Cr substitution on structural, magnetic and electrical conductivity spectra of $LaFeO_3$", *J. Alloys Compd.*, vol. 646, pp. 924-931, 2015.

[23] Coutinho, P. V. and Barrozo, P., "Influence of the heat treatment on magnetization reversal of orthorhombic perovskites $LaFe_{0.5}Cr_{0.5}O_3$", *Appl. Phys. A Mater. Sci. Process.*, vol. 124, pp. 1-5, 2018.

[24] Rodrigues, A. P. G., Morales, M. A., Silva, R. B., Lima, D. R. A. B., Medeiros, R. L. B. A., Araújo, J. H., and Melo, D. M. A., "Positive exchange bias effect in $LaCr_{0.5}Fe_{0.5}O_3$ perovskite", *J. Phys. Chem. Solids*, vol. 141, p. 109334, 2020.

[25] Motin Seikh, M., Pralong, V., Lebedev, O. I., Caignaert, V., and Raveau, B., "The ordered double perovskite $PrBaCo_2O_6$: Synthesis, structure, and magnetism", *J. Appl. Phys.*, vol. 114, pp. 0-5, 2013.

[26] Kleibeuker, J. E., Choi, E.-M., Jones, E. D., Yu, T.-M., Sala, B., MacLaren, B. A., Kepaptsoglou, D., Hernandez-Maldonado, D., Ramasse, Q. M., Jones, L., Barthel, J., MacLaren, I., and MacManus-Driscoll, J. L., "Route to achieving perfect B-site ordering in double perovskite thin films", *NPG Asia Mater.*, vol. 9, pp. e406-e406, 2017.

[27] Dass, R. I. and Goodenough, J. B., "Multiple magnetic phases of $La_2CoMnO_{6-\delta}$ ($0 \leq \delta \leq 0.05$)", *Phys. Rev. B*, vol. 67, pp. 144011-144019, 2003.

[28] Wang, W., Liu, F., Zhang, X., Shen, X., Yao, Y., Wang, Y., Liu, B., Liu, X., and Yu, R., "Two types of B-site ordered structures of the double perovskite Y_2CrMnO_6: Experimental identification and first-principles study", *Inorg. Chem.*

Front., vol. 5, pp. 217-224, 2018.

[29] King, G. and Woodward, P. M., "Cation ordering in perovskites", *J. Mater. Chem.*, vol. 20, pp. 5785-5796, 2010.

[30] Wang, J., Hao, X., Xu, Y., Li, Z., Zu, N., Wu, Z., and Gao, F., "Cation ordering induced semiconductor to half metal transition in La_2NiCrO_6", *RSC Adv.*, vol. 5, pp. 50913-50918, 2015.

[31] Leng, K., Tang, Q., Wei, Y., Yang, L., Xie, Y., Wu, Z., and Zhu, X., "Recent advances in Re-based double perovskites: Synthesis, structural characterization, physical properties, advanced applications, and theoretical studies", *AIP Adv.*, vol. 10, pp. 1-31, 2020.

[32] Chen, X., Xu, J., Xu, Y., Luo, F., and Du, Y., "Rare earth double perovskites: A fertile soil in the field of perovskite oxides", *Inorg. Chem. Front.*, vol. 6, pp. 2226-2238, 2019.

[33] Nasir, M., Kumar, S., Patra, N., Bhattacharya, D., Jha, S. N., Basaula, D. R., Bhatt, S., Khan, M., Liu, S. W., Biring, S., and Sen, S., "Role of antisite disorder, rare-earth size, and superexchange angle on band gap, Curie temperature, and magnetization of R_2NiMnO_6 double perovskites", *ACS Appl. Electron. Mater.*, vol. 1, pp. 141-153, 2019.

[34] Neenu Lekshmi, P., Vasundhara, M., Varma, M. R., Suresh, K. G., and Valant, M., "Structural, magnetic and dielectric properties of rare earth based double perovskites RE_2NiMnO_6 (RE=La, pr, Sm, Tb)", *Phys. B Condens. Matter*, vol. 448, pp. 285-289, 2014.

[35] Sun, M., Xuan, Y., Liu, G., Liu, Y., Zhang, F., Ren, J., and Chen, M., "Anomalous magnetic behaviors of double perovskite R_2CrFeO_6 (R = rare earth elements) predicted by first-principles calculations", *J. Magn. Magn. Mater.*, vol. 504, p. 166670, 2020.

[36] Lv, S., Saito, M., Wang, Z., Chen, C., Chakraverty, S., Kawasaki, M., and Ikuhara, Y., "Atomic-scale structure and electronic property of the $La_2FeCrO_6/SrTiO_3$ interface", *J. Appl. Phys.*, vol. 114, p. 113705, 2013.

[37] Chakraverty, S., Ohtomo, A., Okuyama, D., Saito, M., Okude, M., Kumai, R., Arima, T., Tokura, Y., Tsukimoto, S., Ikuhara, Y., and Kawasaki, M., "Ferrimagnetism and spontaneous ordering of transition metals in double perovskite La_2CrFeO_6 films", *Phys. Rev. B - Condens. Matter Mater. Phys.*, vol. 84, p. 064436, 2011.

[38] Lee, K. W. and Ahn, K. H., "Evaluation of half-metallic antiferromagnetism in A_2CrFeO_6 (A = La, Sr)", *Phys. Rev. B - Condens. Matter Mater. Phys.*, vol. 85, pp. 1-6, 2012.

[39] Booth, R. J., Fillman, R., Whitaker, H., Nag, A., Tiwari, R. M., Ramanujachary, K. V., Gopalakrishnan, J., and Lofland, S. E., "An investigation of structural, magnetic and dielectric properties of R_2NiMnO_6 (R = rare earth, Y)", *Mater. Res. Bull.*, vol. 44, pp. 1559-1564, 2009.

[40] Das, N., Singh, S., Joshi, A. G., Thirumal, M., Reddy, V. R., Gupta, L. C., and Ganguli, A. K., "Pr_2FeCrO_6: A type I multiferroic", *Inorg. Chem.*, vol. 56, pp. 12712-12718, 2017.

[41] Das, S., Bhattacharya, R. N., and Mandal, K. C., "Performance limiting factors of $Cu_2ZnSn(S_xSe_{1-x})_4$ solar cells prepared by thermal evaporation", *Sol. Energy*

Mater. Sol. Cells, vol. 144, pp. 347-351, 2016.

[42] Omata, T., Nagatani, H., Suzuki, I., Kita, M., Yanagi, H., and Ohashi, N., "Wurtzite $CuGaO_2$: A new direct and narrow band gap oxide semiconductor applicable as a solar cell absorber", *J. Am. Chem. Soc.*, vol. 136, pp. 3378-3381, 2014.

[43] Yu, M., Yang, S., Wu, C., and Marom, N., "Machine learning the Hubbard U parameter in DFT+U using Bayesian optimization", *npj Comput. Mater.*, vol. 6, pp. 1-6, 2020.

[44] Ali, M. S., Das, S., Abed, Y. F. and Basith, M. A., "Lead-free $CsSnCl_3$ perovskite nanocrystals: rapid synthesis, experimental characterization and DFT simulations", *Phys. Chem. Chem. Phys.*, vol. 23, pp. 22184-22198, 2021.

[45] Albrecht, D., Lisenkov, S., Ren, W., Rahmedov, D., Kornev, I. A., and Bellaiche, L., "Ferromagnetism in multiferroic $BiFeO_3$ films: A first-principles-based study", *Phys. Rev. B - Condens. Matter Mater. Phys.*, vol. 81, p. 140401, 2010.

[46] Bellaiche, L., Gui, Z., and Kornev, I. A., "A simple law governing coupled magnetic orders in perovskites", *J. Phys. Condens. Matter*, vol. 24, p. 312201, 2012.

[47] Yuan, S. J., Ren, W., Hong, F., Wang, Y. B., Zhang, J. C., Bellaiche, L., Cao, S. X., and Cao, G., "Spin switching and magnetization reversal in single-crystal $NdFeO_3$", *Phys. Rev. B - Condens. Matter Mater. Phys.*, vol. 87, pp. 1-6, 2013.

[48] Su, Y., Zhang, J., Feng, Z., Li, L., Li, B., Zhou, Y., Chen, Z., and Cao, S., "Magnetization reversal and Yb^{3+}/Cr^{3+} spin ordering at low temperature for perovskite $YbCrO_3$ chromites", *J. Appl. Phys.*, vol. 108, pp. 1-6, 2010.

[49] Lei, S., Liu, L., Wang, C., Wang, C., Guo, D., Zeng, S., Cheng, B., Xiao, Y., and Zhou, L., "General synthesis of rare-earth orthochromites with quasi-hollow nanostructures and their magnetic properties", *J. Mater. Chem. A*, vol. 1, pp. 11982-11991, 2013.

[50] Jeong, Y. K., Lee, J. H., Ahn, S. J., and Jang, H. M., "Temperature-induced magnetization reversal and ultra-fast magnetic switch at low field in $SmFeO_3$", *Solid State Commun.*, vol. 152, pp. 1112-1115, 2012.

[51] Yoshii, K., "Magnetic properties of perovskite $GdCrO_3$", *J. Solid State Chem.*, vol. 159, pp. 204–208, 2001.

[52] Yoshii, K., Nakamura, A., Ishii, Y., and Morii, Y., "Magnetic properties of $La_{1-x}Pr_xCrO_3$", *J. Solid State Chem.*, vol. 162, pp. 84-89, 2001.

[53] Sharma, M. K., Singh, K., and Mukherjee, K., "Exchange bias in a mixed metal oxide based magnetocaloric compound $YFe_{0.5}Cr_{0.5}O_3$", *J. Magn. Magn. Mater.*, vol. 414, pp. 116-121, 2016.

[54] Fita, I., Markovich, V., Moskvin, A. S., Wisniewski, A., Puzniak, R., Iwanowski, P., Martin, C., Maignan, A., Carbonio, R. E., Gutowska, M. U., Szewczyk, A., and Gorodetsky, G., "Reversed exchange-bias effect associated with magnetization reversal in the weak ferrimagnet $LuFe_{0.5}Cr_{0.5}O_3$", *Phys. Rev. B*, vol. 97, pp. 1-9, 2018.

[55] Bartel, C. J., Sutton, C., Goldsmith, B. R., Ouyang, R., Musgrave, C. B., Ghiringhelli, L. M., and Scheffler, M., "New tolerance factor to predict the stability of perovskite oxides and halides", *Sci. Adv.*, vol. 5, pp. 1-10, 2019.

[56] Yadav, R. and Elizabeth, S., "Magnetic frustration and dielectric relaxation in insulating Nd_2NiMnO_6 double perovskites", *J. Appl. Phys.*, vol. 117, p. 053902, 2015.

[57] Choudhury, D., Mandal, P., Mathieu, R., Hazarika, A., Rajan, S., Sundaresan, A., Waghmare, U. V., Knut, R., Karis, O., Nordblad, P., and Sarma, D. D., "Near-room-temperature colossal magnetodielectricity and multiglass properties in partially disordered La_2NiMnO_6", *Phys. Rev. Lett.*, vol. 108, pp. 1-5, 2012.

[58] Shi, C., Hao, Y., and Hu, Z., "Local valence and physical properties of double perovskite Nd_2NiMnO_6", *J. Phys. D. Appl. Phys.*, vol. 44, p. 245405, 2011.

[59] Masud, M. G., Dey, K., Ghosh, A., Majumdar, S., and Giri, S., "Occurrence of magnetoelectric effect correlated to the Dy order in Dy_2NiMnO_6 double perovskite", *J. Appl. Phys.*, vol. 118, p. 064104, 2015.

[60] Kumar, P., Ghara, S., Rajeswaran, B., Muthu, D. V. S., Sundaresan, A., and Sood, A. K., "Temperature dependent magnetic, dielectric and Raman studies of partially disordered La_2NiMnO_6", *Solid State Commun.*, vol. 184, pp. 47-51, 2014.

[61] Ueda, K., Tabata, H., and Kawai, T., "Ferromagnetism in $LaFeO_3$-$LaCrO_3$ Superlattices", *Science*, vol. 280, pp. 1064-1066, 1998.

[62] Gaikwad, V. M., Brahma, M., Borah, R., and Ravi, S., "Structural, optical and magnetic properties of Pr_2FeCrO_6 nanoparticles", *J. Solid State Chem.*, vol. 278, p. 120903, 2019.

[63] Shanker, J., Kumar, R. V., Rao, G. N., and Babu, D. S., "Magnetic reversal in Fe substituted $NdCrO_3$ perovskite nanoparticles", *Mater. Chem. Phys.*, vol. 251, p. 123098, 2020.

[64] Maiti, R. P., Dutta, S., Mitra, M. K., and Chakravorty, D., "Large magnetodielectric effect in nanocrystalline double perovskite Y_2FeCrO_6", *J. Phys. D. Appl. Phys.*, vol. 46, pp. 1-7, 2013.

[65] Chanda, S., Saha, S., Dutta, A., Krishna Murthy, J., Venimadhav, A., Shannigrahi, S., and Sinha, T. P., "Magnetic ordering and conduction mechanism of different electroactive regions in Lu_2NiMnO_6", *J. Appl. Phys.*, vol. 120, p. 134102, 2016.

[66] Ullah, M., Ayaz Khan, S., Murtaza, G., Khenata, R., Ullah, N., and Bin Omran, S., "Electronic, thermoelectric and magnetic properties of La_2NiMnO_6 and La_2CoMnO_6", *J. Magn. Magn. Mater.*, vol. 377, pp. 197-203, 2015.

[67] Miura, K. and Terakura, K., "Electronic and magnetic properties of La_2FeCrO_6: Superexchange interaction for a d^5-d^3 system", *Phys. Rev. B - Condens. Matter Mater. Phys.*, vol. 63, p. 104402, 2001.

[68] Hasan, M., Basith, M. A., Zubair, M. A., Hossain, M. S., Mahbub, R., Hakim, M. A., and Islam, M. F., "Saturation magnetization and band gap tuning in $BiFeO_3$ nanoparticles via co-substitution of Gd and Mn", *J. Alloys Compd.*, vol. 687, pp. 701-706, 2016.

[69] Pope, C. G., "X-ray diffraction and the Bragg equation", *J. Chem. Educ.*, vol. 74, pp. 129-131, 1997.

[70] Rietveld, H. M., "The Rietveld method", *Phys. Scr.*, vol. 89, p. 098002, 2014.

[71] Rodriguez-Carvajal, J., "FULLPROF: a program for Rietveld refinement and pattern matching analysis", *Satell. Meet. powder Diffr. XV Congr. IUCr*, vol. 127, p. Toulouse, France, 1990.

[72] Raman, C.V., and Krishnan, K. S., "A new type of secondary radiation", *Nature*, vol. 121, pp. 501-502, 1928.

[73] Semnani, D. (2017) *Electrospun Nanofibers*, Woodhead Publishing, Elsevier.

[74] Ruska, E., "The Development of the Electron Microscope and of Electron Microscopy (Nobel Lecture)", *Angew. Chemie Int. Ed. English*, vol. 26, pp. 595-605, 1987.

[75] de Broglie, L., "Research on the theory of quanta", *Ann. Phys.*, vol. 10, pp. 22-128, 1925.

[76] Fagaly, R. L., "Superconducting quantum interference device instruments and applications", *Rev. Sci. Instrum.*, vol. 77, p. 101101, 2006.

[77] Yang, L. and Miklavcic, S. J., "Revised Kubelka–Munk theory. III. A general theory of light propagation in scattering and absorptive media", *J. Opt. Soc. Am. A*, vol. 22, p. 1866, 2005.

[78] Basith, M. A., Yesmin, N., and Hossain, R., "Low temperature synthesis of $BiFeO_3$ nanoparticles with enhanced magnetization and promising photocatalytic performance in dye degradation and hydrogen evolution", *RSC Adv.*, vol. 8, pp. 29613-29627, 2018.

[79] Basith, M. A., Ahsan, R., Zarin, I., and Jalil, M. A., "Enhanced photocatalytic dye degradation and hydrogen production ability of $Bi_{25}FeO_{40}$-rGO nanocomposite and mechanism insight", *Sci. Rep.*, vol. 8, pp. 33-35, 2018.

[80] Swinehart, D. F., "The Beer-Lambert law", *J. Chem. Educ.*, vol. 39, pp. 333-335, 1962.

[81] Erbe, A., Nayak, S., Chen, Y.H., Niu, F., Pander, M., Tecklenburg, S. and Toparli, C., "How to probe structure, kinetics, and dynamics at complex interfaces in situ and operando by optical spectroscopy", *Encycl. Interfacial Chem.*, vol. 427, pp. 199-219, 2018.

[82] Hohenberg, P., and Kohn, W., "Density functional theory (DFT)", *Phys. Rev B*, vol. 136, p. 864, 1964.

[83] Kohn, W., and Sham, L. J., "Self-consistent equations including exchange and correlation effects", *Phys. Rev.*, vol. 140, p. 1133, 1965.

[84] Schrödinger, E., "Quantisierung als eigenwertproblem", *Ann. Phys.*, vol. 385, pp. 437-490, 1926.

[85] Mitro, S. K., Hadi, M. A., Parvin, F., Majumder, R., Naqib, S. H., and Islama, A. K. M. A., "Effect of boron incorporation into the carbon-site in Nb_2SC MAX phase: Insights from DFT", *J. Mater. Res. Technol.*, vol. 11, pp. 1969-1981, 2021.

[86] Monkhorst, H. J. and Pack, J. D., "Special points for Brillonin-zone integrations", *J. Mater. Chem. A*, vol. 13, p. 5188, 1976.

[87] Alain St.-Amant, Wendy D. Cornell, Peter A. Kollman, T. A. H., "Calculation of molecular geometries, relative conformational energies, dipole moments, and molecular electrostatic potential fitted charges of small organic molecules of biochemical interest by density functional theory", *J. Comput. Chem.*, vol. 16, pp. 1483-1506, 1995.

[88] Saad H. E., M. M. and Elhag, A., "DFT study on the crystal, electronic and magnetic structures of tantalum based double perovskite oxides Ba_2MTaO_6 (M = Cr, Mn, Fe) via GGA and GGA+U", *Results Phys.*, vol. 9, pp. 793-805, 2018.

[89] Zhao, S., Gao, L., Lan, C., Pandey, S. S., Hayase, S., and Ma, T., "Oxygen vacancy formation and migration in double perovskite Sr_2CrMoO_6: A first-principles study", *RSC Adv.*, vol. 6, pp. 43034-43040, 2016.

[90] Kresse, G. and Furthmüller, J., "Efficient iterative schemes for ab initio total-energy calculations using a plane-wave basis set", *Phys. Rev. B*, vol. 54, pp. 11169-11186, 2020.

[91] Kresse, G. and Furthmüller, J., "Efficiency of ab-initio total energy calculations for metals and semiconductors using a plane-wave basis set", *Comput. Mater. Sci.*, vol. 6, pp. 15-50, 1996.

[92] Blöchl, P. E., "Projector augmented-wave method", *Phys. Rev. B*, vol. 50, pp. 17953-17979, 1994.

[93] Kresse, G. and Joubert, D., "From ultrasoft pseudopotentials to the projector augmented-wave method", *Phys. Rev. B*, vol. 59, pp. 1758-1775, 1999.

[94] Perdew, J. P., Burke, K., and Ernzerhof, M., "Generalized gradient approximation made simple", *Phys. Rev. Lett.*, vol. 77, pp. 3865-3868, 1996.

[95] Himmetoglu, B., Floris, A., De Gironcoli, S., and Cococcioni, M., "Hubbard-corrected DFT energy functionals: The LDA+U description of correlated systems", *Int. J. Quantum Chem.*, vol. 114, pp. 14-49, 2014.

[96] Singh, A., Rajput, S., Balasubramanian, P., Anas, M., Damay, F., Kumar, C. M. N., Eguchi, G., Jain, A., Yusuf, S. M., Maitra, T., and Malik, V. K., "Successive spin reorientations and rare earth ordering in $Nd_{0.5}Dy_{0.5}FeO_3$: Experimental and ab initio investigations", *Phys. Rev. B*, vol. 102, pp. 1-13, 2020.

[97] Zhao, H. J., Ren, W., Yang, Y., Íñiguez, J., Chen, X. M., and Bellaiche, L., "Near roomerature multiferroic materials with tunable ferromagnetic and electrical properties", *Nat. Commun.*, vol. 5, pp. 1-7, 2014.

[98] Togo, A. and Tanaka, I., "Spglib: a software library for crystal symmetry search", *arXiv:1808.01590*, pp. 1-11, 2018.

[99] Wang, V., Xu, N., Liu, J. C., Tang, G., and Geng, W. T., "VASPKIT: A user-friendly interface facilitating high-throughput computing and analysis using VASP code", *Comput. Phys. Commun.*, vol. 267, p. 108033, 2021.

[100] Togo, A. and Tanaka, I., "First principles phonon calculations in materials science", *Scr. Mater.*, vol. 108, pp. 1-5, 2015.

[101] Dudarev, S. and Botton, G., "Electron-energy-loss spectra and the structural stability of nickel oxide: An LSDA+U study", *Phys. Rev. B - Condens. Matter Mater. Phys.*, vol. 57, pp. 1505-1509, 1998.

[102] Song, G., Chen, Y., Li, G., and Gao, B., "First-principles study of the electric, magnetic, and orbital structure in perovskite $ScMnO_3$", *RSC Adv.*, vol. 9, pp. 2143-2151, 2019.

[103] Bora, T. and Ravi, S., "Sign reversal of magnetization and ferromagnetism in $NdCr_{1-x}Mn_xO_3$ (x= 0 to 0.50)", *J. Supercond. Nov. Magn.*, vol. 28, pp. 869-872, 2015.

[104] Chakraborty, K. R., Mukherjee, S., Kaushik, S. D., Rayaprol, S., Prajapat, C. L., Singh, M. R., Siruguri, V., Tyagi, A. K., and Yusuf, S. M., "Low temperature neutron diffraction study of $Nd_{1-x}Sr_xCrO_3$ ($0.05 \leq x \leq 0.15$)", *J. Magn. Magn. Mater.*, vol. 361, pp. 81-87, 2014.

[105] Yamaguchi, T., "Theory of spin reorientation in rare-earth orthochromites and orthoferrites", *J. Phys. Chem. Solids*, vol. 35, pp. 479-500, 1974.

[106] Das, S., Bhuyan, M. D. I., and Basith, M. A., "First-principles calculation of the electronic and optical properties of Gd_2FeCrO_6 double perovskite: Effect of Hubbard U parameter", *J. Mater. Res. Technol.*, vol. 13, pp. 2408-2418, 2021.

[107] Henkelman, G., Arnaldsson, A., and Jónsson, H., "A fast and robust algorithm for Bader decomposition of charge density", *Comput. Mater. Sci.*, vol. 36, pp. 354-360, 2006.

[108] Mannepalli, V. R., Saj Mohan, M. M., and Ranjith, R., "Tailoring the bandgap and magnetic properties by bismuth substitution in neodymium chromite", *Bull. Mater. Sci.*, vol. 40, pp. 1503-1511, 2017.

[109] Nguyen, T. A., Pham, T. Le, Mittova, I. Y., Mittova, V. O., Nguyen, T. L. T., Van Nguyen, H., and Bui, V. X., "Co-doped $NdFeO_3$ nanoparticles: Synthesis, optical and magnetic properties study", *Nanomaterials*, vol. 11, pp. 1-9, 2021.

[110] Quattropani, A., Stoeffler, D., Fix, T., Schmerber, G., Lenertz, M., Versini, G., Rehspringer, J. L., Slaoui, A., Dinia, A., and Colis, S., "Band-Gap tuning in ferroelectric Bi_2FeCrO_6 double perovskite thin films", *J. Phys. Chem. C*, vol. 122, pp. 1070-1077, 2018.

[111] Geneste, G., Paillard, C., and Dkhil, B., "Polarons, vacancies, vacancy associations, and defect states in multiferroic $BiFeO_3$", *Phys. Rev. B*, vol. 99, pp. 1–20, 2019.

[112] Mocherla, P. S. V., Karthik, C., Ubic, R., Ramachandra Rao, M. S., and Sudakar, C., "Tunable bandgap in $BiFeO_3$ nanoparticles: The role of microstrain and oxygen defects", *Appl. Phys. Lett.*, vol. 103, pp. 1-5, 2013.

[113] Wang, J., Luo, L., Han, C., Yun, R., Tang, X., and Zhu, Y., "The microstructure, electric, optical and photovoltaic properties of $BiFeO_3$ thin films prepared by low temperature sol–gel method", *Materials (Basel).*, vol. 12, pp. 1-10, 2019.

[114] Wu, H., Pei, Z., Xia, W., Lu, Y., Leng, K., and Zhu, X., "Structural, magnetic, dielectric and optical properties of double-perovskite Bi_2FeCrO_6 ceramics synthesized under high pressure", *J. Alloys Compd.*, vol. 819, p. 153007, 2020.

[115] Emery, A. A. and Wolverton, C., "High-throughput DFT calculations of formation energy, stability and oxygen vacancy formation energy of ABO_3 perovskites", *Sci. Data*, vol. 4, pp. 1-10, 2017.

[116] Han, D., Zhang, T., Huang, M., Sun, D., Du, M. H., and Chen, S., "Predicting the thermodynamic stability of double-perovskite halides from density functional theory", *APL Mater.*, vol. 6, p. 084902, 2018.

[117] Qi, X., Cai, N., Chen, T., Wang, S., and Li, B., "Experimental and theoretical studies on the elasticity of tungsten to 13 GPa", *J. Appl. Phys.*, vol. 124, pp. 1-7, 2018.

[118] Vajeeston, P. and Fjellvåg, H., "First-principles study of structural stability, dynamical and mechanical properties of Li_2FeSiO_4 polymorphs", *RSC Adv.*, vol. 7, pp. 16843-16853, 2017.

[119] Mouhat, F. and Coudert, F. X., "Necessary and sufficient elastic stability conditions in various crystal systems", *Phys. Rev. B - Condens. Matter Mater. Phys.*, vol. 90, pp. 4-7, 2014.

[120] Chu, B., Li, D., Tian, F., Duan, D., Sha, X., Lv, Y., Zhang, H., Liu, B., and Cui, T., "Structural, mechanical, and electronic properties of Rh_2B and RhB_2: First-principles calculations", *Sci. Rep.*, vol. 5, pp. 1-7, 2015.

[121] Cheng, X. Y., Chen, X. Q., Li, D. Z., and Li, Y. Y., "Computational materials discovery: The case of the W-B system", *Acta Crystallogr. Sect. C Struct. Chem.*, vol. 70, pp. 85–103, 2014.

[122] Pajda, M., Kudrnovský, J., Turek, I., Drchal, V. and Bruno, P., "Ab initio calculations of exchange interactions, spin-wave stiffness constants, and Curie temperatures of Fe, Co, and Ni", *Phys. Rev. B*, vol. 64, pp. 1-9, 2001.

[123] Chen, W., George, J., Varley, J. B., Rignanese, G. M., and Hautier, G., "High-throughput computational discovery of $In_2Mn_2O_7$ as a high Curie temperature ferromagnetic semiconductor for spintronics", *npj Comput. Mater.*, vol. 5, pp. 1-7, 2019.

[124] Kabiraj, A., Kumar, M., and Mahapatra, S., "High-throughput discovery of high Curie point two-dimensional ferromagnetic materials", *npj Comput. Mater.*, vol. 6, pp. 1-9, 2020.

[125] Wu, C., Yu, Z., Sun, K., Nie, J., Guo, R., Liu, H., Jiang, X., and Lan, Z., "Calculation of exchange integrals and Curie temperature for La-substituted barium hexaferrites", *Sci. Rep.*, vol. 6, pp. 1-8, 2016.

[126] Sasani, A., Iñiguez, J. and Bousquet, E., "Magnetic phase diagram of rare-earth orthorhombic perovskite oxides", *Phys. Rev. B*, vol. 104, p. 064431, 2021.

[127] Ong, K. P., Blaha, P., and Wu, P., "Origin of the light green color and electronic ground state of $LaCrO_3$", *Phys. Rev. B - Condens. Matter Mater. Phys.*, vol. 77, pp. 2-5, 2008.

[128] Kharkwal, K. C., Roy, R., Kumar, H., Bera, A. K., Yusuf, S. M., Shukla, A. K., Kumar, K., Kanungo, S., and Pramanik, A. K., "Structure, magnetism, and electronic properties in 3d-5d based double perovskite $(Sr_{1-x}Ca_x)_2FeIrO_6$ ($0{\leq}x{\leq}1$)", *Phys. Rev. B*, vol. 102, pp. 1-18, 2020.

[129] Nazir, S., "Insulator-to-half metal transition and enhancement of structural distortions in Lu_2NiIrO_6 double perovskite oxide via hole-doping", *Sci. Rep.*, vol. 11, pp. 1-10, 2021.

[130] Zhu, X. H., Xiao, X. B., Chen, X. R., and Liu, B. G., "Electronic structure, magnetism and optical properties of orthorhombic $GdFeO_3$ from first principles", *RSC Adv.*, vol. 7, pp. 4054-4061, 2017.

[131] Zhao, H. J., Bellaiche, L., Chen, X. M., and Íñiguez, J., "Improper electric polarization in simple perovskite oxides with two magnetic sublattices", *Nat. Commun.*, vol. 8, pp. 1-11, 2017.

[132] Gauvin-Ndiaye, C., Baker, T. E., Karan, P., Massé, Balli, M., Brahiti, N., Eskandari, M. A., Fournier, P., Tremblay, A. M. S., and Nourafkan, R., "Electronic and magnetic properties of the candidate magnetocaloric-material double perovskites La_2MnCoO_6, La_2MnNiO_6, and La_2MnFeO_6", *Phys. Rev. B*, vol. 98, pp. 1-9, 2018.

[133] Chang, H., Gao, Y., Liu, F., Liu, Y., Zhu, H., and Yun, Y., "Effect of synthesis on structure, oxygen voids, valence bands, forbidden band gap and magnetic domain configuration of La_2CoMnO_6", *J. Alloys Compd.*, vol. 690, pp. 8-14, 2017.

[134] Chanda, S., Saha, S., Dutta, A., and Sinha, T. P., "Structural and transport

properties of double perovskite Dy_2NiMnO_6", *Mater. Res. Bull.*, vol. 62, pp. 153-160, 2015.

[135] Ohtomo, A., Chakraverty, S., Mashiko, H., Oshima, T. and Kawasaki, M., "Spontaneous atomic ordering and magnetism in epitaxially stabilized double-perovskites", *Mater. Res. Soc. Symp. Proc.*, vol. 1454, pp. 3-13, 2012.

[136] Anderson, M. T., Greenwood, K. B., Taylor, G. A., and Poeppelmeier, K. R., "B-cation arrangements in double perovskites", *Prog. Solid State Chem.*, vol. 22, pp. 197-233, 1993.

[137] Li, Z., Cho, Y., Li, X., Li, X., Aimi, A., Inaguma, Y., Alonso, J. A., Fernandez-Diaz, M. T., Yan, J., Downer, M. C., Henkelman, G., Goodenough, J. B., and Zhou, J., "New mechanism for ferroelectricity in the perovskite $Ca_{2-x}Mn_xTi_2O_6$ synthesized by spark plasma sintering", *J. Am. Chem. Soc.*, vol. 140, pp. 2214-2220, 2018.

[138] Lufaso, M. W. and Woodward, P. M., "Prediction of the crystal structures of perovskites using the software program SPuDS", *Acta Crystallogr. Sect. B*, vol. B57, pp. 725-738, 2001.

[139] Yamada, I., Takamatsu, A., and Ikeno, H., "Complementary evaluation of structure stability of perovskite oxides using bond-valence and density-functional-theory calculations", *Sci. Technol. Adv. Mater.*, vol. 19, pp. 101-107, 2018.

[140] Byeon, S. H., Lufaso, M. W., Parise, J. B., Woodward, P. M., and Hansen, T., "High-pressure synthesis and characterization of perovskites with simultaneous ordering of both the A- and B-site cations, $CaCu_3Ga_2M_2O_{12}$ (M = Sb, Ta)", *Chem. Mater.*, vol. 15, pp. 3798-3804, 2003.

[141] Mccusker, L. B., Von Dreele, R. B., Cox, D. E., Louër, D., and Scardi, P., "Rietveld refinement guidelines", *J. Appl. Crystallogr.*, vol. 32, pp. 36-50, 1999.

[142] Rietveld, H. M., "A profile refinement method for nuclear and magnetic structures", *J. Appl. Crystallogr.*, vol. 2, pp. 65-71, 1969.

[143] Momma, K. and Izumi, F., "VESTA 3 for three-dimensional visualization of crystal, volumetric and morphology data", *J. Appl. Crystallogr.*, vol. 44, pp. 1272-1276, 2011.

[144] Parida, K., Dehury, S. K., and Choudhary, R. N. P., "Electrical, optical and magneto-electric characteristics of $BiBaFeCeO_6$ electronic system", *Mater. Sci. Eng. B*, vol. 225, pp. 173-181, 2017.

[145] Purohit, V., Padhee, R., and Choudhary, R. N. P., "Dielectric and impedance spectroscopy of $Bi(Ca_{0.5}Ti_{0.5})O_3$ ceramic", *Ceram. Int.*, vol. 44, pp. 3993-3999, 2018.

[146] Iliev, M. N., Abrashev, M. V., Litvinchuk, A. P., Hadjiev, V. G., Guo, H., and Gupta, A., "Raman spectroscopy of ordered double perovskite La_2CoMnO_6 thin films", *Phys. Rev. B - Condens. Matter Mater. Phys.*, vol. 75, pp. 1-6, 2007.

[147] Bhuyan, M. D. I., Das, S., and Basith, M. A., "Sol-gel synthesized double perovskite Gd_2FeCrO_6 nanoparticles: Structural, magnetic and optical properties", *J. Alloys Compd.*, vol. 878, p. 160389, 2021.

[148] Guo, H., Burgess, J., Street, S., Gupta, A., Calvarese, T. G., and Subramanian, M. A., "Growth of epitaxial thin films of the ordered double perovskite La_2NiMnO_6 on different substrates", *Appl. Phys. Lett.*, vol. 89, p. 022509, 2006.

[149] Obregón, S. and Colón, G., "Improved O_2 evolution from a water splitting reaction over Er^{3+} and Y^{3+} co-doped tetragonal $BiVO_4$", *Catal. Sci. Technol.*, vol. 4, pp. 2042-2050, 2014.

[150] Nakamoto, K. (2006) *Handbook of Vibrational Spectroscopy*. John Wiley & Sons, Ltd., Hoboken, New Jersey, United States.

[151] Bilovol, V., Ferrari, S., Derewnicka, D., and Saccone, F. D., "XANES and XPS study of electronic structure of Ti-enriched Nd-Fe-B ribbons", *Mater. Chem. Phys.*, vol. 146, pp. 269-276, 2014.

[152] Joshi, N., da Silva, L. F., Shimizu, F. M., Mastelaro, V. R., M'Peko, J. C., Lin, L., and Oliveira, O. N., "UV-assisted chemiresistors made with gold-modified ZnO nanorods to detect ozone gas at room temperature", *Microchim. Acta*, vol. 186, pp. 1-9, 2019.

[153] Brown, I. D., and Altermatt, D., "Bond-Valence parameters obtained from a systematic analysis of the inorganic crystal structure database.", *Acta Crystallogr. B Struct. Sci.*, vol. 244, pp. 244-247, 1985.

[154] Kanamori, J., "Superexchange interaction and symmetry properties of electron orbitals", *J. Phys. Chem. Solids*, vol. 10, pp. 87-98, 1959.

[155] Goodenough, J. B., "Theory of the role of covalence in the perovskite-type manganites [La,M(II)]MnO_3", *Phys. Rev.*, vol. 100, pp. 564-573, 1955.

[156] Wang, L., Wang, S. W., Zhang, X., Zhang, L. L., Yao, R., and Rao, G. H., "Reversals of magnetization and exchange-bias in perovskite chromite $YbCrO_3$", *J. Alloys Compd.*, vol. 662, pp. 268-271, 2016.

[157] Yoshii, K., "Positive exchange bias from magnetization reversal in $La_{1-x}Pr_xCrO_3$ (x ~0.7-0.85)", *Appl. Phys. Lett.*, vol. 99, pp. 2012-2015, 2011.

[158] Arima, T., Tokura, Y., and Torrance, J. B., "Variation of optical gaps in perovskite-type 3d transition-metal oxides", *Phys. Rev. B*, vol. 48, pp. 17006-17009, 1993.

[159] Tauc, J., Grigorovici, R. and Vancu, A., "Optical properties and electronic structure of amorphous germanium", *Phys. Status Solidi*, vol. 15, pp. 627-637, 1966.

[160] Nowak, M., Kauch, B., and Szperlich, P., "Determination of energy band gap of nanocrystalline SbSI using diffuse reflectance spectroscopy", *Rev. Sci. Instrum.*, vol. 80, pp. 4-7, 2009.

[161] Mulliken, R. S., "Electronic structures of molecules XI. Electroaffinity, molecular orbitals and dipole moments", *J. Chem. Phys.*, vol. 3, pp. 573-585, 1935.

[162] Mulliken, R. S., "A new electroaffinity scale; Together with data on valence states and on valence ionization potentials and electron affinities", *J. Chem. Phys.*, vol. 2, pp. 782-793, 1934.

[163] Reunchan, P., Boonchun, A., and Umezawa, N., "Electronic properties of highly-active Ag_3AsO_4 photocatalyst and its band gap modulation: An insight from hybrid-density functional calculations", *Phys. Chem. Chem. Phys.*, vol. 18, pp. 23407-23411, 2016.

[164] Bull, C. L. and McMillan, P. F., "Raman scattering study and electrical properties characterization of elpasolite perovskites $Ln_2(BB')O_6$ (Ln=La, Sm...Gd and B,B'=Ni, Co, Mn)", *J. Solid State Chem.*, vol. 177, pp. 2323-2328, 2004.

[165] Guo, H. Z., Burgess, J., Ada, E., Street, S., Gupta, A., Iliev, M. N., Kellock, A. J.,

Magen, C., Varela, M., and Pennycook, S. J., "Influence of defects on structural and magnetic properties of multifunctional La_2NiMnO_6 thin films", *Phys. Rev. B - Condens. Matter Mater. Phys.*, vol. 77, pp. 13-21, 2008.

[166] Retuerto, M., Muñoz, Á., Martínez-Lope, M. J., Alonso, J. A., Mompeán, F. J., Fernández-Díaz, M. T., and Sánchez-Benítez, J., "Magnetic interactions in the double perovskites R_2NiMnO_6 (R = Tb, Ho, Er, Tm) investigated by neutron diffraction", *Inorg. Chem.*, vol. 54, pp. 10890-10900, 2015.

[167] Panitz, J. C., Mayor, J. C., Grob, B., and Durisch, W., "A Raman spectroscopic study of rare earth mixed oxides", *J. Alloys Compd.*, vol. 303-304, pp. 340-344, 2000.

[168] Cowin, P. I., Lan, R., Petit, C. T. G., and Tao, S., "Conductivity and redox stability of double perovskite oxide $SrCaFe_{1+x}Mo_{1-x}O_{6-\delta}$ (x = 0.2, 0.4, 0.6)", *Mater. Chem. Phys.*, vol. 168, pp. 50-57, 2015.

[169] Ding, H., Tao, Z., Liu, S., and Yang, Y., "A redox-stable direct-methane solid oxide fuel cell (SOFC) with $Sr_2FeNb_{0.2}Mo_{0.8}O_{6-\delta}$ double perovskite as anode material", *J. Power Sources*, vol. 327, pp. 573-579, 2016.

[170] Han, W., Wang, Z., Li, Q., Liu, H., Fan, Q., Dong, Y., Kuang, Q., and Zhao, Y., "Autoclave growth, magnetic, and optical properties of GdB_6 nanowires", *J. Solid State Chem.*, vol. 256, pp. 53-59, 2017.

[171] Das, S., Ahmmad, B., and Basith, M. A., "Thermal stability of the crystallographic structure of nanocrystalline $Nd_{0.7}Sr_{0.3}MnO_3$ manganite with enhanced magnetic properties", *AIP Adv.*, vol. 10, p. 095135, 2020.

[172] Ortega-San Martin, L., Chapman, J. P., Lezama, L., Sánchez-Marcos, J., Rodríguez-Fernández, J., Arriortua, M. I., and Rojo, T., "Factors determining the effect of Co(II) in the ordered double perovskite structure: Sr_2CoTeO_6", *J. Mater. Chem.*, vol. 15, pp. 183-193, 2005.

[173] Cox, D. E., Shirane, G., and Frazer, B. C., "Neutron-diffraction study of antiferromagnetic Ba_2CoWO_6 and Ba_2NiWO_6", *J. Appl. Phys.*, vol. 38, pp. 1459-1460, 1967.

[174] Primo-Martín, V. and Jansen, M., "Synthesis, structure, and physical properties of cobalt perovskites: $Sr_3CoSb_2O_9$ and $Sr_2CoSbO_{6-\delta}$", *J. Solid State Chem.*, vol. 157, pp. 76-85, 2001.

[175] Li, M. R., Stephens, P. W., Retuerto, M., Sarkar, T., Grams, C. P., Hemberger, J., Croft, M. C., Walker, D., and Greenblatt, M., "Designing polar and magnetic oxides: Zn_2FeTaO_6 - In search of multiferroics", *J. Am. Chem. Soc.*, vol. 136, pp. 8508-8511, 2014.

[176] Feng, H. L., Arai, M., Matsushita, Y., Tsujimoto, Y., Guo, Y., Sathish, C. I., Wang, X., Yuan, Y. H., Tanaka, M., and Yamaura, K., "High-temperature ferrimagnetism driven by lattice distortion in double perovskite Ca_2FeOsO_6", *J. Am. Chem. Soc.*, vol. 136, pp. 3326-3329, 2014.

[177] Basith, M. A., Khan, F. A., Ahmmad, B., Kubota, S., Hirose, F., Ngo, D. T., Tran, Q. H., and Mølhave, K., "Tunable exchange bias effect in magnetic $Bi_{0.9}Gd_{0.1}Fe_{0.9}Ti_{0.1}O_3$ nanoparticles at temperatures up to 250 K", *J. Appl. Phys.*, vol. 118, pp. 4-9, 2015.

[178] Segall, M. D., Lindan, P. J. D., Probert, M. J., Pickard, C. J., Hasnip, P. J., Clark, S. J., and Payne, M. C., "First-principles simulation: Ideas, illustrations and the

CASTEP code", *J. Phys. Condens. Matter*, vol. 14, pp. 2717-2744, 2002.

[179] Fischer, T. H. and Almlöf, J., "General methods for geometry and wave function optimization", *J. Phys. Chem.*, vol. 96, pp. 9768-9774, 1992.

[180] Zhang, J. T., Lu, X. M., Zhou, J., Su, J., Min, K. L., Huang, F. Z., and Zhu, J. S., "First-principles study of structural, electronic, and magnetic properties of double perovskite Ho_2MnFeO_6", *Phys. Rev. B - Condens. Matter Mater. Phys.*, vol. 82, pp. 1-8, 2010.

[181] Chakraborty, M., Pal, P., and Sekhar, B. R., "Half metallicity in $Pr_{0.75}Sr_{0.25}MnO_3$: A first principle study", *Solid State Commun.*, vol. 145, pp. 197-200, 2008.

[182] Zhang, X. D., Guo, M. L., Li, W. X., and Liu, C. L., "First-principles study of electronic and optical properties in wurtzite $Zn_{1-x}Cd_xO$", *J. Appl. Phys.*, vol. 103, p. 063721, 2008.

[183] Shenton, J. K., Bowler, D. R. and Cheah, W. L., "Effects of the Hubbard U on density functional-based predictions of $BiFeO_3$ properties", *J. Phys. Condens. Matter*, vol. 29, p. 445501, 2018.

[184] Mann, G. W., Lee, K., Cococcioni, M., Smit, B., and Neaton, J. B., "First-principles Hubbard U approach for small molecule binding in metal-organic frameworks", *J. Chem. Phys.*, vol. 144, p. 174104, 2016.

[185] Neaton, J. B., Ederer C., Waghmare, U. V., Spaldin, N. A., Rabe, K. M., "First-principles study of spontaneous polarization in multiferroic $BiFeO_3$", *Phys. Rev. B*, vol. 71, p. 014113, 2005.

[186] Yaakob, M. K., Taib, M. F. M., Lu, L., Hassan, O. H., and Yahya, M. Z. A., "Self-interaction corrected LDA + U investigations of $BiFeO_3$ properties: Plane-wave pseudopotential method", *Mater. Res. Express*, vol. 2, p. 116101, 2015.

[187] Bredas, J. L., "Mind the gap!", *Mater. Horizons*, vol. 1, pp. 17-19, 2014.

[188] Das, S., Bhowal, M. K., and Dhar, S., "Calculation of the band structure, carrier effective mass, and the optical absorption properties of GaSbBi alloys", *J. Appl. Phys.*, vol. 125, p. 075705, 2019.

[189] Rozilah, R., Yaakob, M. K., Mohamed, Z. and Yahya, A. K., "Effects of on-site Coulomb interaction (U) on the structural and electronic properties of half- metallic ferromagnetic orthorhombic $Pr_{0.75}Na_{0.25}MnO_3$ manganite: A LDA+U calculation and experimental study", *Mater. Res. Express*, vol. 4, p. 066103, 2015.

[190] Segall, M. D., Shah, R., Pickard, C. J. and Payne, M. C., "Population analysis of plane-wave electronic structure calculations of bulk materials", *Phys. Rev. B*, vol. 54, pp. 317-320, 1996.

[191] Mulliken, R. S., "Electronic population analysis on LCAO-MO molecular wave functions. I", *J. Chem. Phys.*, vol. 23, pp. 1833-1840, 1955.

[192] Ching, W. Y. and Xu, Y. N., "Nonscalability and nontransferability in the electronic properties of the Y-Al-O system", *Phys. Rev. B - Condens. Matter Mater. Phys.*, vol. 59, pp. 12815-12821, 1999.

[193] Phillips, J. C., "Covalent bond in crystals. I. Elements of a structural theory", *Phys. Rev.*, vol. 166, pp. 832-838, 1968.

[194] Craig, D. P., Maccoll, A., Nyholm, R. S., Orgel, L. E. and Sutton, L. E., "Chemical bonds involving d-orbitals. Part I", *J. Chem. Soc.*, pp. 332-353, 1954.

[195] Brik, M. G., Parasyuk, O. V., Myronchuk, G. L. and Kityk, I. V., "Specific features

of band structure and optical anisotropy of $Cu_2CdGeSe_4$ quaternary compounds", *Mater. Chem. Phys.*, vol. 47, pp. 155-161, 2014.

[196] Honglin, L., Yingbo, L., Jinzhu, L., and Ke, Y., "Experimental and first-principles studies of structural and optical properties of rare earth (RE = La, Er, Nd) doped ZnO", *J. Alloys Compd.*, vol. 617, pp. 102-107, 2014.

[197] Harun, K., Salleh, N. A., Deghfel, B., Yaakob, M. K. and Mohamad, A. A., "DFT+U calculations for electronic, structural, and optical properties of ZnO wurtzite structure: A review", *Results Phys.*, vol. 16, p. 102829, 2020.

[198] Perdew, J. P., "Density functional theory and the band gap problem", *Int. J. Quantum Chem.*, vol. 28, pp. 497-523, 1985.

[199] Brown, J. J. and Page, A. J., "The Hubbard-U correction and optical properties of d0 metal oxide photocatalysts", *J. Chem. Phys.*, vol. 153, p. 224116, 2020.